ARTIFACT IDENTIFICATION FOR BLOOD PRESSURE AND PHOTOPLETHYSMOGRAPHY SIGNALS IN AN UNSUPERVISED ENVIRONMENT

LIM POOI KHOON

FACULTY OF ENGINEERING
UNIVERSITY OF MALAYA
KUALA LUMPUR

2020

ARTIFACT IDENTIFICATION FOR BLOOD PRESSURE AND PHOTOPLETHSMOGRAPHY SIGNALS IN AN UNSUPERVISED ENVIRONMENT

LIM POOI KHOON

THESIS SUBMITTED IN FULFILMENT OF THE REQUIREMENTS FOR THE DEGREE OF DOCTOR OF PHILOSOPHY OF BIOMEDICAL ENGINEERING

FACULTY OF ENGINEERING
UNIVERSITY OF MALAYA
KUALA LUMPUR

2020

UNIVERSITY OF MALAYA

ORIGINAL LITERARY WORK DECLARATION

Name of Candidate: Lim Pooi Khoon

Matric No: HHC130016

Name of Degree: Doctor of Philosophy

Title of Project Paper/Research Report/Dissertation/Thesis ("this Work"):

Artifact Identification for Blood Pressure and Photoplethysmography Signals in an Unsupervised Environment

Field of Study: Biomedical Engineering

I do solemnly and sincerely declare that:

(1) I am the sole author/writer of this Work;
(2) This Work is original;
(3) Any use of any work in which copyright exists was done by way of fair dealing and for permitted purposes and any excerpt or extract from, or reference to or reproduction of any copyright work has been disclosed expressly and sufficiently and the title of the Work and its authorship have been acknowledged in this Work;
(4) I do not have any actual knowledge nor do I ought reasonably to know that the making of this work constitutes an infringement of any copyright work;
(5) I hereby assign all and every rights in the copyright to this Work to the University of Malaya ("UM"), who henceforth shall be owner of the copyright in this Work and that any reproduction or use in any form or by any means whatsoever is prohibited without the written consent of UM having been first had and obtained;
(6) I am fully aware that if in the course of making this Work I have infringed any copyright whether intentionally or otherwise, I may be subject to legal action or any other action as may be determined by UM.

Candidate's Signature Date: 1/5/2020

Subscribed and solemnly declared before,

Witness's Signature Date:

Name:

Designation:

ARTIFACT IDENTIFICATION FOR BLOOD PRESSURE AND PHOTOPLETHYSMOGRAPHY SIGNALS IN AN UNSUPERVISED ENVIRONMENT

ABSTRACT

Physiological signals play a significant role in clinical diagnosis, it always acts as a major input of a decision support system. However, the physiological signal is easily corrupted by different factors especially motion artifacts. Several research works have been tried to recover the underlying physiological signal by suppressing the artifact. However, not much attention has been paid to situation where the artifact is too extreme and the artifact suppression is not possible. In this situation, physiological signal quality must be evaluated before any further assessment. In this study, an automated artifact detection algorithm was developed for Blood Pressure and PPG signals. For Blood Pressure signal, an automatic algorithm based on relative changes in the cuff pressure and neighbouring oscillometric pulses was proposed to remove outlier points caused by movement artifacts. Next, multiple linear regression (MLR) and support vector regression (SVR) models were used to examine the relationship between the Systolic Blood Pressure (SBP) and the Diastolic Blood Pressure (DBP) ratio with ten features extracted from the oscillometric waveform envelope (OWE). Upon using the artifact detection method followed by BP estimation, the SBP and DBP were improved in BHS grades from D to A. With regards to the AAMI standard, the mean ± SD of difference between the estimated and the gold standard SBP improved from 4.5±28.6 mmHg to -0.3±5.8mmHg and -0.6±5.4 mmHg using the MLR and SVR, respectively. Meanwhile, the mean ± SD of difference for DBP improved from 0.0±14.2 mmHg to -0.2±6.4 mmHg and 0.4±6.3 mmHg using the MLR and SVR, respectively. For PPG signal, two master templates have been generated from PhysioNet MIMIC II database. The master template is then updated with each of the incoming clean pulse. Correlation coefficient

were used to classify the PPG pulse into either good or bad quality categories. The robustness of this artifact detection algorithm was then evaluated on both short and continuous data collected from young and older subjects which included arrhythmia patients. For short data, the average accuracy improved from 95.2% to 98.0%. For long continuous data on healthy subject, an average accuracy of 91.5%, sensitivity of 94.1% and specificity of 89.7% were achieved. Meanwhile, for long continuous data on elder subject which included arrhythmia patients, an average accuracy of 91.3%, sensitivity of 80.5% and specificity 93.0% were achieved.

Keywords: Blood Pressure, Photoplethysmography, Artifact, Unsupervised environment

PENILAIAN ARTIFAK TEKANAN DARAH DAN GELOMBANG FOTOPLETISMOGRAFI JARI (PPG) DALAM KAWASAN TANPA PENGAWASAN

ABSTRAK

Isyarat fisiologi memainkan peranan penting dalam diagnosis klinikal, di mana ia sentiasa menjadi input utama dalam sistem sokongan keputusan. Walau bagaimanapun, isyarat fisiologi mudah dipengaruhi oleh banyak faktor terutamanya oleh gerakan tubuh badan kita. Beberapa kajian penyelidikan cuba memulihkan isyarat fisiologi dengan mengurangkan artifak tersebut. Bagaimanapun, tidak banyak perhatian diberikan kepada situasi di mana artifak terlalu banyak/melampau dan menyebabkan pengurangan artifak menjadi tidak mungkin. Dalam keadaan ini, kualiti isyarat fisiologi mesti dinilai sebelum digunakan. Dalam kajian ini, algoritma pengesanan artifak automatik telah dibangunkan untuk isyarat Tekanan Darah dan PPG. Untuk isyarat Tekanan Darah, algoritma automatik berdasarkan perubahan pada tekanan 'cuff' dengan nadi bersebelahan telah dicadangkan untuk menghapuskan artifak yang disebabkan oleh pergerakan. Selepas itu, regresi linear berganda (MLR) dan regresi vektor sokongan (SVR) telah digunakan untuk menilai perhubungan antara Tekanan Darah Sistolik (SBP) dengan nisbah Tekanan Darah Diastolik (DBP) melalui sepuluh ciri yang diekstrak dari sampul gelombang oscillometric (OWE). Kaedah anggaran tekanan darah telah digunakan selepas penggunaan kaedah pengesanan artifak, SBP dan DBP telah ditingkatkan dari gred D ke A (dalam piawai BHS) dengan menggunakan kaedah MLR dan SVR. Menurut piawai AAMI, perbezaan purata ± sisihan piawai SBP diperbaiki dari 4.5 ± 28.6 mmHg kepada -0.3 ± 5.8 mmHg dan -0.6 ± 5.4 mmHg bagi MLR dan SVR. Sementara itu, purata ± sisihan piawai DBP ditingkatkan dari 0.0 ± 14.2 mmHg kepada -0.2 ± 6.4 mmHg dan 0.4 ± 6.3 mmHg untuk MLR dan SVR. Untuk isyarat PPG, dua pencontoh utama telah dihasilkan daripada

pangkalan data PhysioNet MIMIC II. Pencontoh utama kemudian akan dikemas kini berdasarkan kemunculan setiap nadi yang baik. Pekali korelasi kemudiannya akan digunakan untuk mengklasifikasikan nadi PPG ke dalam kategori kualiti baik atau buruk. Kekuatan algoritma pengesanan artifak ini kemudiannya akan dinilai pada kedua-dua data pendek dan berterusan yang dikumpulkan dari subjek-subjek muda dan tua termasuk pesakit aritmia. Untuk data yang pendek, ketepatan telah ditingkatkan dari 95.2% (Lee et al., 2003) kepada 98.0%. Untuk data berterusan yang melibatkan subjek sihat, ketepatan 91.5%, kepekaan 94.1% dan spesifikas 89.7% telah dicapai. Sementara itu, untuk data berterusan yang melibatkan pesakit tua termasuk pesakit aritmia, ketepatan 91.3%, sensitiviti 80.5% dan spesifikasi 93.0% telah dicapai.

Kata kunci: Tekanan darah, Fotopletismografi Jari (PPG), artifak, kawasan tanpa pengawasan

ACKNOWLEDGEMENTS

First of all, I would like to thank my supervisor, Associate Professor Ir. Dr. Lim Einly, for her consistent supervision and guidance during my doctoral research. I am also grateful for her endless encouragement, support, and tolerance. I am thankful to have my co-supervisor, Dr. Ng Siew Cheok. His expertise and contribution, particularly in the artifact algorithm development, made this project goes smoothly. I would like to thank him for his patience and guidance during my PhD study. My special gratitude goes to co- supervisors Scientia Professor Nigel Lovell and Associate Professor Stephen Redmond from Graduate School of University of New South Wales (UNSW). They were extremely helpful in getting the Sotera Visi Mobile device for data collection. I would like to thank them for their assistances and supervision during my attachment in UNSW. I would like to thank Professor Tan Maw Pin from University Malaya Medical Centre for her effort the patient recruitment process. Many thanks to Dr. Yu Yong Poh and Dr. Goh Choon Hian for their guidance during my PhD research. Last but not least, my deepest gratitude goes to my parents, siblings, daughter, best friends and colleagues in the Asian Cardiac Engineering Laboratory for their unconditional love and support during my PhD study.

TABLE OF CONTENTS

LIST OF FIGURES

LIST OF TABLES

LIST OF SYMBOLS AND ABBREVIATIONS

List of Abbreviations

AAMI	:	Advancement of Medical Instrumentation's
ABPM	:	Ambulatory BP monitors
AC	:	Alternating current
AF	:	Atrial fibrillation
AV node	:	Atrioventricular node
BHS	:	British Hypertension Society
BP	:	Blood pressure
bpm	:	Numbers of beat per minutes
CB	:	Capnobase
CP	:	Cuff pressure
CSL	:	Complex System Laboratory
CNN	:	Convolution Neural Network
DBP	:	Diastolic blood pressure
DBPA	:	Diastolic blood pressure amplitude
DBPR	:	Diastolic blood pressure ratio
DC	:	Direct current
ECG	:	Electrocardiograph
EMD	:	Empirical mode decomposition
FFT	:	Fourier transforms
GS	:	Gold standard

GUI	:	Graphical User Interface
Hb	:	Haemoglobin
HbO_2	:	Oxygenated haemoglobin
HR	:	Heart rate
HREA	:	Human Research Ethics Advisory
HRV	:	Heart rate variability
IBP	:	Invasive blood pressure
ICA	:	Independent component analysis
ICU	:	Intensive Care Unit
LA	:	Left arm
LED	:	Light-emitting diode
LL	:	Left leg
MA	:	Maximum amplitude
MAA	:	Maximum amplitude algorithm
MAP	:	Mean arterial pressure
MLR	:	Multiple linear regression
NIBP	:	Non-invasive blood pressure
NN	:	Neural network
NPV	:	Negative predictive value
OMW	:	Oscillometric waveform
OMWE	:	Oscillometric waveform envelope
PAT	:	Pulse arrival time

PCA	:	Principal component analysis
PCs	:	Principal components
PD	:	Photodetector
PP	:	Pulse pressure
PPG	:	Photoplethysmogram
PPV	:	Positive predictive value
PTT	:	Pulse transit time
PVCs	:	Premature ventricular contractions
PW	:	Pulse width
PWV	:	Pulse wave velocity
RA	:	Right arm
RDT	:	Random distortion testing
refPW	:	Reference pulse width
RR	:	Respiration rate
RS	:	Reference scoring
RSA	:	Respiratory Sinus Arrhythmia
SA node	:	Sinoatrial node
SBP	:	Systolic Blood Pressure
SBPA	:	Systolic Blood Pressure Amplitude
SBPR	:	Systolic Blood Pressure ratio
SD	:	Standard deviation
SDE	:	Standard deviation error

SE	:	Shannon Entropy
SFFS	:	Sequential Forward floating selection
SQI	:	Signal quality index
SVM	:	Support vector machine
SVR	:	Support vector regression
SpO_2	:	Oxygen saturation
Th	:	Threshold
VFCDM	:	Variable frequency complex demodulation
UMMC	:	University Malaya Medical Centre
UNSW	:	University of New South Wales

List of Symbols

α	:	Learning rate

LIST OF APPENDICES

CHAPTER 1: INTRODUCTION

1.1 Research motivation

One out of three adults suffer from multiple chronic conditions globally (Hajat & Stein, 2018). The top four chronic diseases that affect almost two-thirds of deaths every year are heart disease, cancer, stroke and diabetes. This has become a new challenge in the medical field as there will be an inadequate number of nurses to cater for the growing aging population. Besides that, the exploding number of patients also increases hospitalisation costs (Hajat & Stein, 2018). Traditional health care models that only react to patients when chronic diseases develop might no longer be adequate to handle the issue. Therefore, preventive health care measures that include frequent health screening is implemented as this will somehow improve patients' health care quality and reduce health care costs (Noel, Vogel, Erdos, Cornwall, & Levin, 2004). Telehealth care is one of the new approaches that provide long term health status monitoring and it is taken to solve this aging population problem and reduce hospitalization rate (Anzanpour et al., 2017; Nia, Mozaffari-Kermani, Sur-Kolay, Raghunathan, & Jha, 2015; Yin, Akmandor, Mosenia, & Jha, 2018).

Telehealth is defined as the usage of electronic information and telecommunication technologies to support and deliver clinical health care services over distance (Bowles & Baugh, 2007; Institute of Medicine Committee on Evaluating Clinical Applications of, 1996). Telehealth care usually involves the collection of physiological signals in an unsupervised environment such as the patient's home or care center. Then, these data will be transmitted to the central database which is accessible for health care professionals. A decision support system will then play its role to manage and analyse the data. Health care professionals will be allowed to monitor the well-being of the patient with the help of the decision made from the system and provide necessary health care management.

Telehealth has been implemented in a few countries for the past 20 years. In the US, the telehealth system has been well established with more than half of the hospitals equipped with a telemedicine programme. The number of patients using telehealth services has increased from 22 million in 2013 to 30 million in 2017 and it is predicted to increase to 81 million in 2050. Several studies have shown positive outcomes with the usage of telehealth in the US such as improving communication between doctor and patient, providing more accuracy in decision making and reducing patient length of stay in the intensive care unit (ICU) (Demaerschalk, Raman, Ernstrom, & Meyer, 2012; Hilty, Nesbitt, Marks, & Callahan, 2002; Palen, Price, Shetterly, & Wallace, 2012; Young et al., 2011).

Physiological signals are the major inputs of the decision support system. With the use of the internet and the decision support system, a massive number of data can be managed and interpreted in a fast and easy manner. However, the ability of the decision support systems to make the right call is highly dependent on the quality of the recorded data. This is because further derivation from the physiological signals can provide more information about one's health condition. Thus, the signal quality assessment of the physiological signal is crucial for further evaluations (Redmond, Xie, Chang, Basilakis, & Lovell, 2012). The consequence of a lack of reliable signal quality causes a high false alarm rate. In a supervised environment such as the ICU, the false alarm rate was reported as high as 90% (Aboukhalil, Nielsen, Saeed, Mark, & Clifford, 2008). Other studies also reported that only 8% (Tsien & Fackler, 1997) or lower (Redmond et al., 2012) of the alarms were classified as true alarms with clinical significance. With the high occurrence of false alarms, the workload of clinicians has indirectly increased (Imhoff & Kuhls, 2006) and thus leads to slow response time to the alarms (Donchin & Seagull, 2002). In some cases, clinicians might even miss the true alarm (Clifford et al., 2016; Donchin & Seagull, 2002; Meng'anyi, Omondi, & Muiva, 2017). On the other hand, a high false

alarm rate may increase patient anxiety (John Allen & Murray, 1996; Chambrin, 2001; Cropp, Woods, Raney, & Bredle, 1994; Hug, Clifford, & Reisner, 2011) and increase the re-hospitalisation rate (Hagerman et al., 2005; Novaes, Aronovich, Ferraz, & Knobel, 1997).

Some manufacturers have recognised the importance of artifact detection and have implemented that in their devices such as Nellcor (Boulder, CO, USA) and Masimo (Irvine, CA, USA). However, those artifact detection algorithms are proprietary. Yet, there are some public databases (e.g. PhysioNet) that allow researchers to design their own algorithms and make comparisons. However, most of the algorithms were only applied in data collected from the ICU where the patient's movement is limited. The performance of their algorithms on unsupervised environments which usually contain motion artifacts is not known. Limited artifact detection studies have focused on data containing motion artifacts. Sukor *et* al. (2011) and Chong *et al*. (2014) have conducted their studies on evaluating the performance of their algorithm on motion corrupted data. However, both studies only involved short segments of photoplethysmogram (PPG) signals (i.e., 1 minute duration). Continuous PPG signals at longer duration (i.e. more than 30 minutes) are known to contain much more variations. Thus, this PhD study aimed to develop automatic artifact detection algorithms for blood pressure (BP) and Photoplethysmography (PPG) signals, and evaluated their robustness on both short and continuous data collected from young and older subjects which included arrhythmia patients.

1.2 Research Scope

The scope of the thesis includes the development of artifact detection algorithms for BP and PPG. In the BP study, 4 recordings (2 recordings from each arm) were collected from 25 healthy subjects aged 28 ± 5 years. One of the two measurements were purposely

contaminated with movements during cuff deflation. Artifact were then removed based on features extracted from the oscillometric curve. Three algorithms – Maximum Amplitude Algorithm (MAA), Multiple Linear Regression (MLR) and Support Vector Regression (SVR) were then used to estimate BP. In the PPG study, two PPG master templates were generated. Next, the developed artifact detection algorithm was tested on both short (6 s) and long continuous data with different cohorts with movements: 19 young healthy subjects (aged between 18 and 45 years), 15 healthy older subjects (aged above 65 years old) and 4 older patients with arrhythmia.

1.3 Objectives

i. To develop an automatic algorithm to detect and remove artifacts during continuous oscillometric BP measurement.
ii. To estimate the BP reading accurately through oscillometric waveform in the presence of artifacts.
iii. To develop an online algorithm to detect artifacts in PPG signals.
iv. To investigate the effectiveness of the developed PPG noise detection algorithm in ambulatory long-continuous data (i.e. longer than 30mins) which contain several types of motion artifacts and short segment data (6s) in unsupervised environment.
v. To test the PPG artifact detection algorithm in different patient cohorts (young and older subjects including arrhythmia patient).

1.4 Thesis Contribution

The contributions of this thesis include:

i. Introduction of a novel technique for automatically identifying noise sections in BP recording.

ii. Introduction of multiple linear regression (MLR) and support vector regression (SVR) to estimate the Systolic Blood Pressure (SBP) and Diastolic Blood Pressure (DBP) accurately in the presence of noise.

iii. Development of an adaptive template algorithm to detect artifact in PPG signal. This algorithm is simple as only two variables (the threshold value and the learning rate) need to be optimized. This algorithm does not require any prior knowledge of the PPG signal, such as amplitude, pulse width and slope, thus making our algorithm suitable for a diverse range of datasets acquired from different devices.

iv. Besides that, two PPG master templates were generated from the Physionet database(Goldberger et al., 2000) (a publicly available database).This eliminates the need to generate subject-specific templates to account for inherent differences in the PPG waveform morphology across subjects, which resulted in long processing time.

v. Online detection algorithm. The response time of the PPG algorithm (i.e. 2 s) was much shorter as compared to other studies, thus making our algorithm robust and suitable for online detection purpose (within 2 s).

vi. The developed PPG algorithm had demonstrated accuracy of more than 90% in normal young, older and older subjects with arrhythmia.

1.5 Thesis organisation

This thesis consists of six chapters. Chapter 1 contains the backgrounds of research work, scope, research motivation and objectives of the study. This thesis introduced an artifact identification algorithm for BP and photoplethysmography signals in an unsupervised environment.

Chapter 2 detailed the background of the physiological signal quality in an unsupervised environment, including home telecare, decision support system, types of physiological signals and the importance of physiological signal quality assessment. This chapter focused on the development of signal quality assessment for BP and PPG, different types of recording techniques, existing artifact detection techniques, signal quality assessment and challenges in BP and PPG signals recording or post-processing.

Chapter 3 focuses on the development of an automated artifact detection algorithm in BP signals. A gold standard as well as the development of the graphical user interface (GUI) to evaluate the algorithm's performance. Next, the performance of ten extracted features from the oscillometric waveform envelope (OMWE) was evaluated. Besides that, the sequential forward floating selection (SFFS) method was used to minimise and identify the best combination of features that result in the best performance. Two different methods, using MLR and SVR were developed to estimate SBP and DBP.

Chapter 4 focuses on the development of an artifact detection algorithm in PPG signals. Two PPG master templates were generated from the PhysioNet database (Goldberger et al., 2000) (a publicly available dataset). Then, the algorithm was applied on two datasets, which are: (i) Sotera Visi Mobile dataset, which contained poses and movements in daily activities; and (ii) PhysioNet MIMIC II dataset, which was recorded from the ICU environment. The performance of the algorithm in classifying PPG signals based on Gold Standard (GS) annotation, discussion and conclusion are presented.

Although the developed PPG algorithm were proven to be accurate in heathy subject, its effectiveness on other subject cohorts remain unknown. Therefore, chapter 5 discusses the testing of the proposed PPG artifact detection algorithm on older and arrhythmia patients. The performance of the algorithm on older subjects is compared with young healthy subjects. Discussion and conclusion are also presented.

Lastly, Chapter 6 presents the conclusion of the present work, limitations of the existing algorithm and recommendations for future work.

CHAPTER 2: LITERATURE REVIEW

In the following sections, three main physiological signals commonly recorded in a home telehealth care system, i.e. ECG, BP and PPG signal, are described.

2.1 Electrocardiograph (ECG) signal

ECG is a measurement of electrical activity of the heart through the skin surface. Cardiac muscle cells in the walls of the heart send the signal to the heart and cause contraction. The sinoatrial node (SA node, anatomical pacemaker) starts the sequence by causing the atrial muscles to contract. From there, the signal travels to the atrioventricular node (AV node), through the Bundle of His, down the bundle branches, and through the Purkinje fibers, causing the ventricles to contract. This signal creates an electrical current that is called ECG.

2.1.1 Techniques of measurements

ECG can be recorded quickly by placing some electrodes on the chest area. The resulting measurements are referred to as leads. Different lead systems have been developed and improved over the past century; these included the most common 3-lead and 12-lead ECG.

2.1.1.1 3-lead ECG (Einthoven's Triangle)

In 1903, Einthoven recorded the first ECG by using 3-lead ECG through the combination of three electrodes (Right arm (RA), Left arm (LA), and Left leg (LL)) as shown in Figure 2.1 and it only offers three views (lead of the heart) which is named as Lead I (right and left arm), Lead II (right arm and left leg) and Lead III (left arm and left leg).

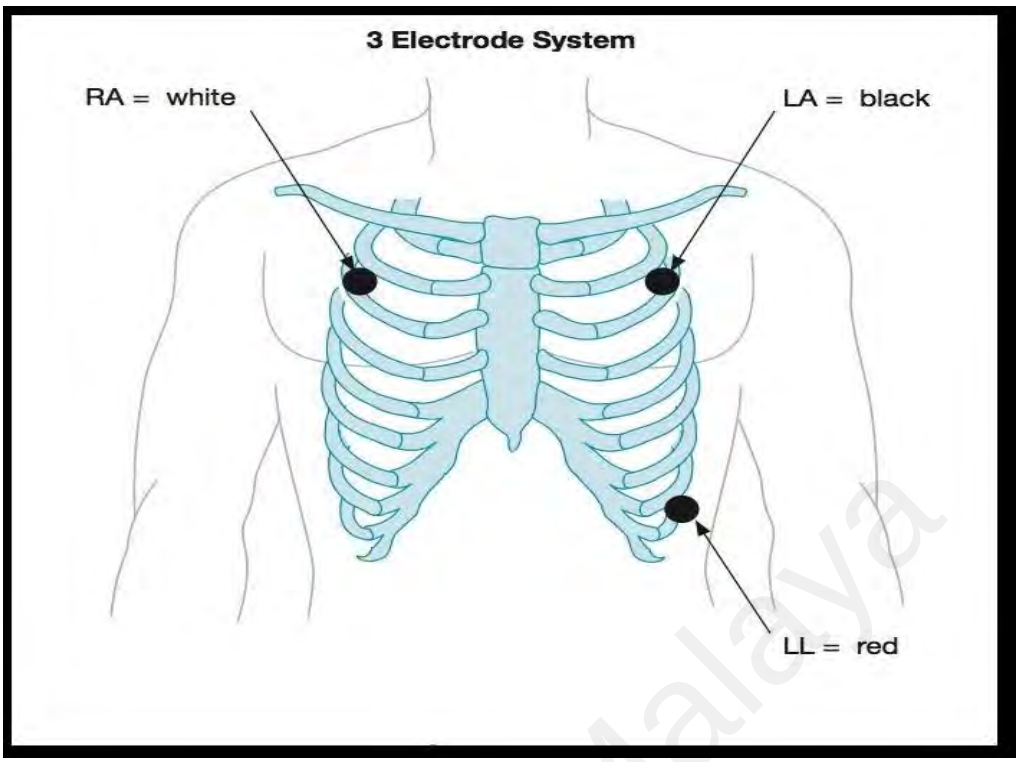

Figure 2.1: Electrode position of 3-lead ECG (Pounds, 2018).

Figure 2.2 is an example of a normal ECG consisting of a P wave, a QRS complex, a T wave, and a U wave that each has a fairly unique pattern as described in the following:

- The P wave represents atrial depolarisation.
- The QRS complex represents ventricular depolarisation.
- The T wave represents ventricular repolarisation.
- The U wave represents papillary muscle repolarisation.

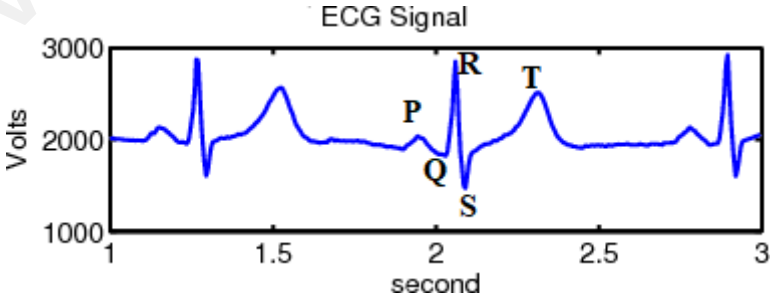

Figure 2.2: A normal ECG tracing, seen on Lead II, constituting a P wave, a QRS complex and a T wave.

2.1.1.2 12-lead ECG

The further development of 3-lead systems has resulted in the classic 12 leads of today. In a conventional 12-lead ECG, ten electrodes as shown in Figure 2.3 and Table 2.1 were placed on the patient's limbs and chest. By using 12-lead ECG, 12 different views (three limb leads, six chest leads and three 'augmented' leads) of the electrical activities of the heart are measured.

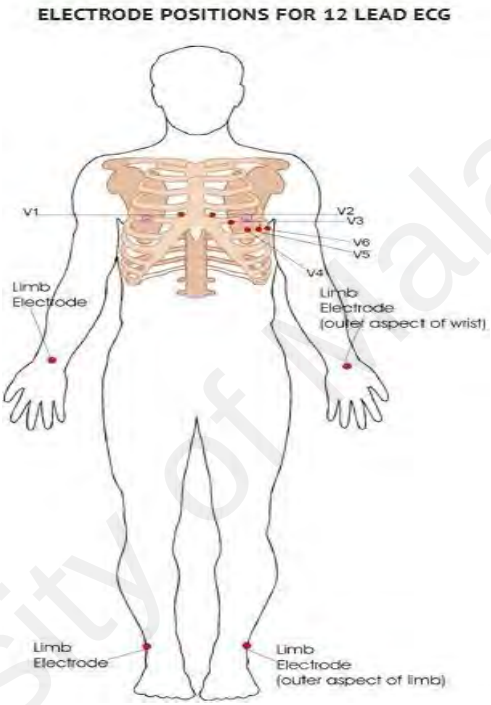

Figure 2.3: The ten electrode positions for 12-lead ECG recording, consisting of the four limb electrodes and six electrodes spread across the rib cage near the heart (V1, V2, V3, V4, V5 and V6) (Ihara, 2006).

Table 2.1: Electrode placement position (Burke, 2018)

Electrode	Placement
V1	Between ribs 4 and 5 to the right of the sternum
V2	Between ribs 4 and 5 to the left of sternum
V3	Between leads V2 and V4
V4	Between ribs 5 and 6 in the mid-clavicular line
V5	In the left anterior axillary line, horizontally even with V4
V6	In the midaxillary line, horizontally even with V4 and V5

Table 2.2 continued: Electrode placement position (Burke, 2018)

Electrode	Placement
RL	On the right leg
RA	On the right arm
LL	On the left leg
LA	On the left arm

2.1.2 Applications of ECG signal

Heart rate (HR) is one of the most basic features that can be extracted from ECG. HR can be determined by finding the R-R distance (the time difference between two consecutive R peaks in one complete ECG signal) as shown in Figure 2.4.

$$Heart\ Rate\ (HR) = \frac{60}{R-R\ distance} . \frac{beats}{min} \tag{2.1}$$

The normal range of HR is 60 to 120 beats per minute (BPM). The calculated HR is useful to determine heart abnormalities such as bradycardia and tachycardia.

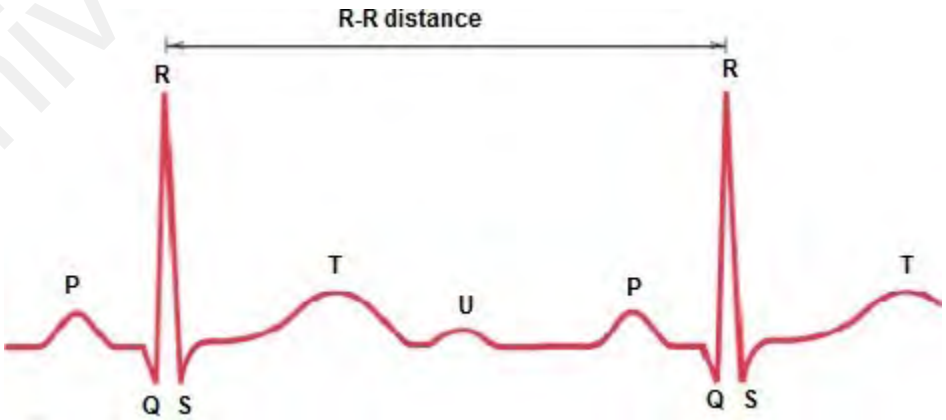

Figure 2.4: ECG signal.

HR only focused on the average beats per minute while heart rate variability (HRV) measures the specific change in time (or variability) between successive heart beats. HRV

can be simply acquired by applying Equation 2.2:

$$\text{HRV} = \frac{\text{mean (R} - \text{R distance)}}{\text{number of beats per minute (bpm)}} \tag{2.2}$$

Generally, a low HRV (or less variability in the heart beats) indicates that the body is under stress from exercise, psychological events, or other internal or external stressors. Higher HRV (or greater variability between heart beats) usually means that the body has a strong ability to tolerate stress or is strongly recovering from prior accumulated stress. During resting conditions, high HRV will be preferred rather than low HRV. When in an active state, lower HRV is generally favourable compared to high HRV (Shaffer & Ginsberg, 2017).

Besides that, a large amount of information which indicate heart performance can be acquired from the ECG signal and it have always been used to detect arrhythmias (irregularities in heart rhythm) (B. Zhu, Ding, & Hao, 2013), coronary artery disease (blockage or narrowed arteries in the heart) (Moyer, 2012)， heart attack history (Jin, 2018), structural problems of heart chambers (Joshi, Tomar, & Tomar, 2014), and recovering conditions of heart disease treatment, such as effects of cardiac drugs (Ghamsari, Dadpour, & Najari, 2016; Grad & Zdrenghea, 2014) and the functions of implanted pacemakers (Greenhut, Jenkins, & DiCarlo, 1991).

Respiration rate (RR) is one of the important indications of health conditions and it is calculated by the number of breaths per minute when a person is at rest. This RR can also be observed from ECG where HR increases during inhalation and decreases during exhalation. Figure 2.5 shows the relationship between ECG and the respiration series.

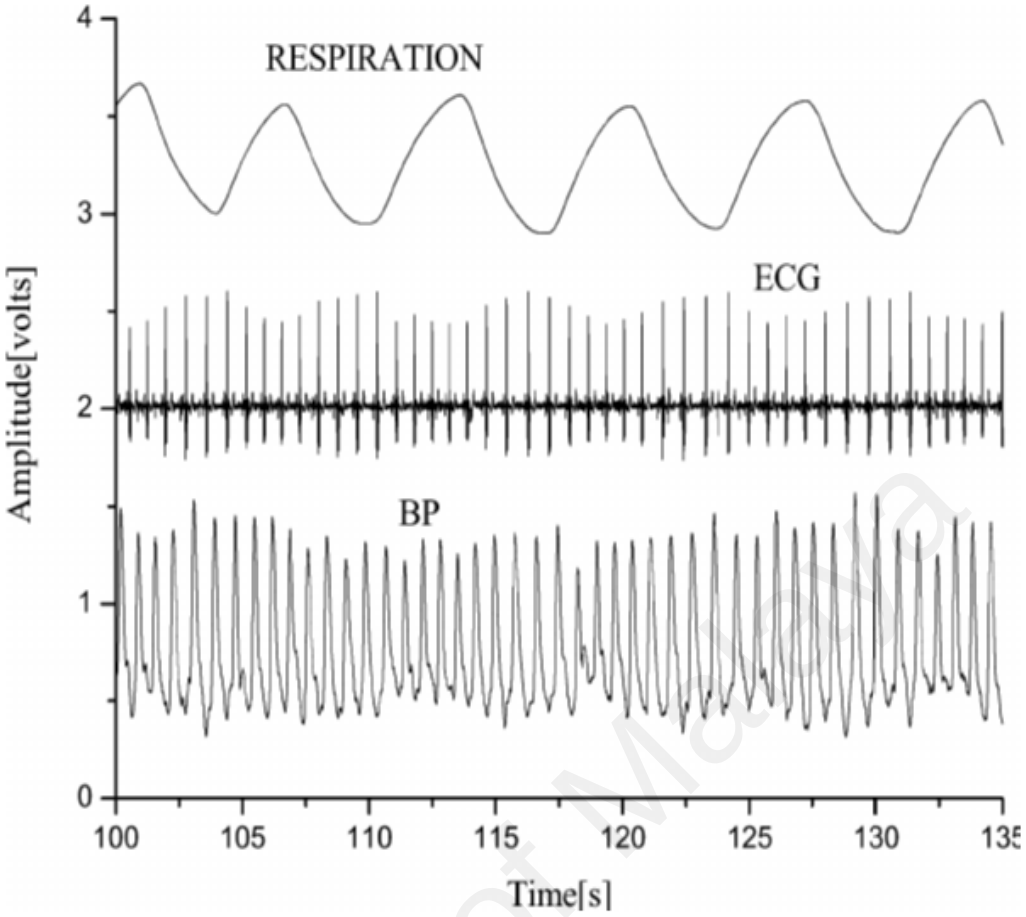

Figure 2.5: Relation between ECG and respiration series (Burke, 2018).

2.1.3 Challenges in ECG signal processing

2.1.3.1 Challenges due to external factors

ECG artifacts are extremely common and may happen due to electrical interference by external sources, electrical noise from elsewhere in the body, poor contact of ECG electrodes, and machine malfunction.

Alternating current (AC) refers to the electric power that is delivered to our housing area. In the US, the AC current is 50Hz while the AC current in Malaysia is 60Hz. Interference by AC power happens when the ECG machine is poorly grounded. This will result in a thick-looking ECG line as shown in Figure 2.6.

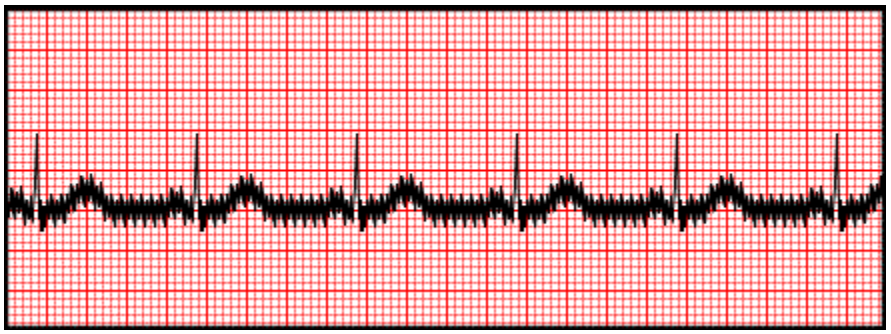

Figure 2.6: 60Hz AC interference ("Section 12 : ECG Artifacts.,").

Pacing spikes are seen in people who have implanted pacemakers. This will lead to a sharp, thin spike, followed by ventricles depolarising (wide QRS complex) as seen in Figure 2.7.

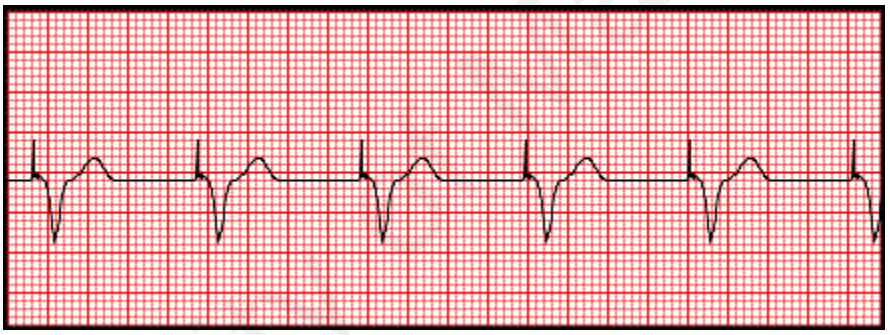

Figure 2.7: Artificial pacemaker spikes ("Section 12 : ECG Artifacts.").

Electrode/lead misplacement may also lead to artifacts. If the lead is misplaced, an upside-down ECG as shown in Figure 2.8 will occur.

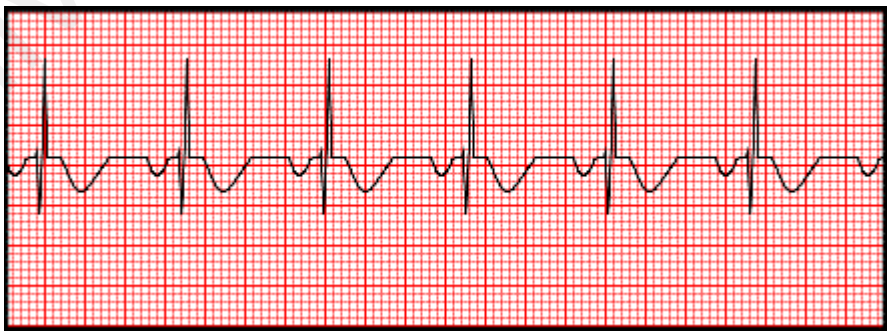

Figure 2.8: Reversed leads ("Section 12 : ECG Artifacts.").

Other than the heart, muscles in our body also produce electricity. When your skeletal muscles undergo tremors, the ECG artifacts as shown in Figure 2.9 will be displayed.

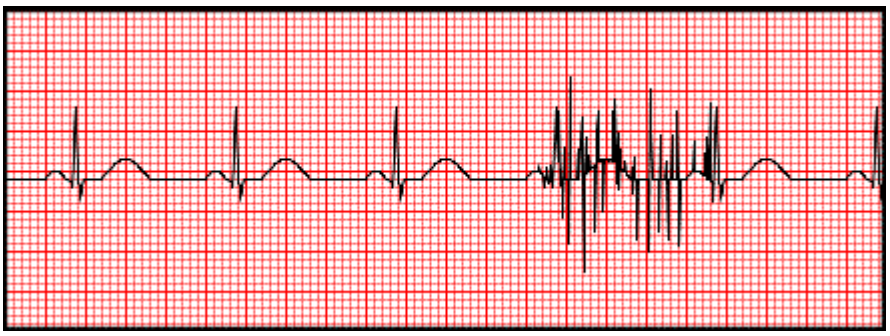

Figure 2.9: Muscle tremors ("Section 12 : ECG Artifacts.").

For the wandering baseline, the ECG is going up and down as shown in Figure 2.10. This is normally caused by the movement of cables during ECG recording. Patient movement, dirty lead wires/electrodes, loose electrodes, and a variety of other things can cause this as well.

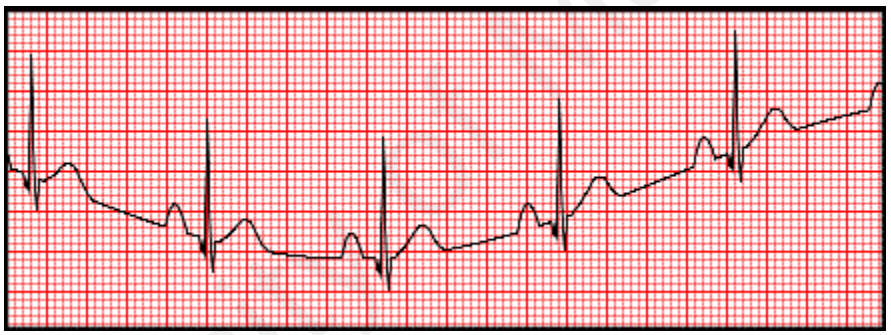

Figure 2.10: Wandering baseline artifact ("Section 12 : ECG Artifacts.").

2.1.3.1 Challenges due to disease conditions

Cardiovascular diseases take 17.9 million of lives every year, and occupies 31% of global deaths ("On World Heart day WHO calls for accelerated action to prevent the world's leading global killer," 2019). Arrhythmia is the most common cardiovascular disease that will lead to HR miscalculation in signal processing. Arrhythmia refers to any condition where there is abnormal electrical activity in the heart. Atrial fibrillation (AF) is the most common type of arrhythmia. AF is caused by rapid and chaotic electrical discharges within the atria as shown in Figure 2.11. These electrical pulses do not start from the SA node, so the ECG will not show any P waves. As the atrial activity is chaotic,

AF shows irregular HR and may lead to error in HR calculation.

Figure 2.11: AF with P wave missing ("Basic ECG Interpretation Learning Package", 2009).

Ventricular arrhythmias are caused by abnormal heart rhythms that start in the ventricles, usually due to early or extra beat generated from ventricles. The depolarisation of cardiac cells starts in the ventricle instead of the SA node. Types of ventricular arrhythmias include premature ventricular contractions (PVCs), ventricular fibrillation and ventricular tachycardia. Figure 2.12 is an example of ventricular arrhythmia, where when the ECG is disturbed, the ECG algorithm may have difficulty in finding the correct R peaks, leading to mistakes of HR measurement.

Figure 2.12: Ventricular arrhythmias ("Basic ECG Interpretation Learning Package", 2009).

Ventricular fibrillation shows a completed ECG abnormal rhythm as shown in Figure 2.13. This is because the heart's ventricular cells are excitable and depolarising randomly, causing the ventricle to not contract properly. The accuracy of HR measurements is highly dependent on the ability of the ECG algorithm to identify the R-peaks from ECG signals. However, when an abnormal rhythm occurs, the ECG algorithm will not be able to execute correctly and thus this leads to error.

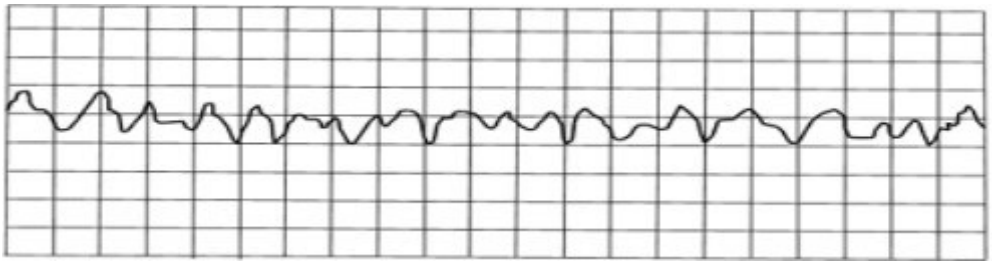

Figure 2.13: Ventricular fibrillation ("Basic ECG Interpretation Learning Package", 2009).

Ventricular tachycardia is a fast HR which originates in the ventricles. It is characterised by the absence of P waves and a wide QRS complex – with duration of greater than 0.12 seconds as shown in Figure 2.14. The measured HR is usually greater than 100 beats per minute. The mechanism of ventricular tachycardia usually causes an area of increased automaticity or a re-entrant or pathway looping in a ventricle. It can sometimes generate an output great enough to produce a pulse; at other times no pulse can be felt.

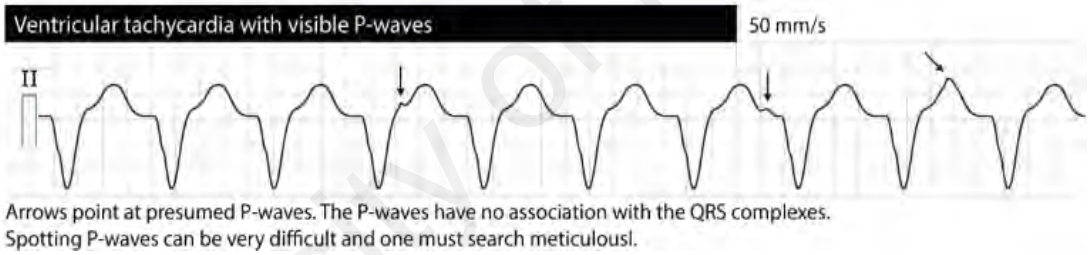

Figure 2.14: Ventricular tachycardia with visible P waves ("Basic ECG Interpretation Learning Package", 2009).

Other than that, asystole might also generate HR measurement error by not showing any cardiac output (ECG will show a flat line). This is caused by the absence of any electrical heart activity. Some of the diseases mentioned above might be correctly identified if the abnormality is occurring throughout the ECG signal. However, the abnormality in ECG might not appear continuously, usually one or two beats in a 10s ECG signal. Therefore, error in HR computation might occur (abnormal increase or decrease in HR).

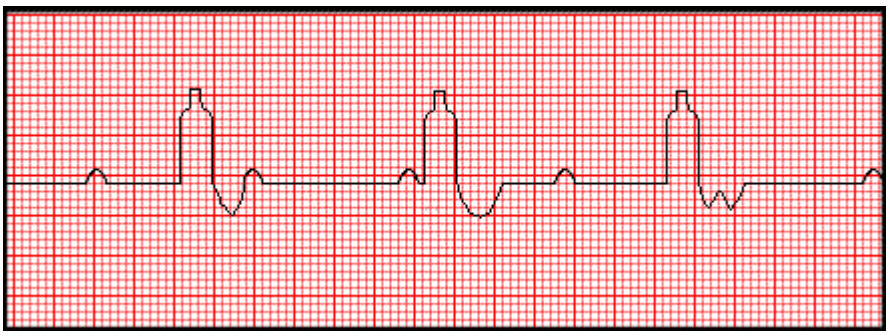

Figure 2.15: Absolute heart block ("Section 12 : ECG Artifacts.").

When absolute heart block happens, QRS complexes are wide and bottle-shaped and show no relationship with the P wave as shown in Figure 2.15.

2.2 Blood Pressure (BP)

BP is the force exerted by your blood against your arteries. As your heart pumps, it forces blood out through arteries that carry the blood throughout your body. The arteries keep tapering off in size until they become tiny vessels, called capillaries. At the capillary level, oxygen and nutrients are released from your blood and delivered to the organs.

BP, commonly expressed in terms of systolic (maximum) and diastolic (minimum) pressures, offers important insights into cardiovascular health. High BP (hypertension), which may lead to stroke and heart failure, has been rated as one of the most important causes of premature death by the World Health Organisation ("World Heart Federation", 2007). On the other hand, excessively low BP (hypotension) may indicate underlying diseases such as heart failure and adrenal insufficiency (Gupta & Lipsitz, 2007). Thus, BP measurement is routinely performed (Perloff et al., 1993). Table 2.2 shows the different categories of BP.

Table 2.3: BP Categories (Whelton et al., 2018). SBP: Systolic Blood Pressure; DBP: Diastolic Blood Pressure.

Category	SBP	Relation	DBP
Hypotension	<90	And	<60
Normal	90-119	And	60-79
Pre-hypertension	120-129	And	<80
Hypertension (Stage 1)	130-139	Or	80-89
Hypertension (Stage 2)	140 or higher	Or	90 or higher
Hypertension Crisis (consult your doctor immediately)	Higher than 180	And/Or	Higher than 120

2.2.1 Techniques of measurements Generally, there are two types of BP measurement techniques which are invasive (also known as direct measurement) and non-invasive (indirect measurement) (Leslie Alexander Geddes, 1970).

2.2.1.1 Invasive Blood Pressure (IBP) measurement

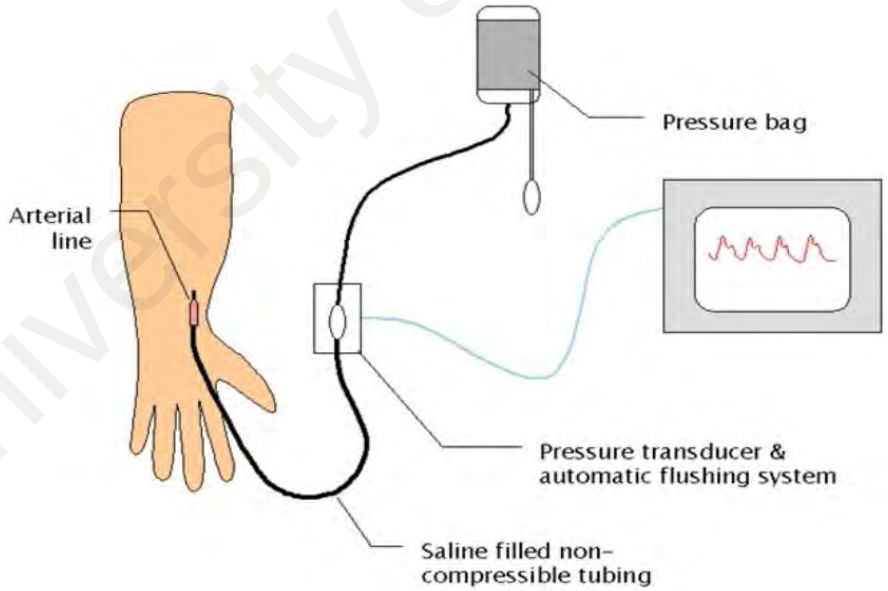

Figure 2.16: IBP measurement.

The IBP measuring system was developed in 1733 by putting an arterial catheter into an artery (this is known as arterial line) (Ward & Langton, 2007). A saline-filled compressible tuning was used to connect the arterial line to an automatic flushing system which is attached to the pressure transducer. The arterial pulse of the pressure waveform

will be transmitted through the column of fluid to the pressure transducer where it is converted into an electrical signal. The electrical signal will then be processed, amplified and displayed by the microprocessor on the screen. Figure 2.16 shows the IBP measurement. This is always done in the ICU, operation room and coronary care units (Raftery, 1978).

However, IBP measurement is not suitable to be used on all patients due to the pain as well as the infection risk that could occur when inserting the catheter into the blood vessel (Heravi, Khalilzadeh, & Joharinia, 2014). Even though there is a certain level of risk of invasive measurement, there are several advantages over non-invasive blood pressure (NIBP) (Jones & Pratt, 2009). IBP allows continuous pulse-to-pulse BP measurement and can be used for further analyses by providing further information about cardiovascular status. This allows close monitoring of the patient's health and increases the accuracy as compared to NIBP.

2.2.1.2 Non-invasive Blood Pressure measurement (NIBP)

As an alternative, several non-invasive BP estimation methods that are safer, quicker and require less expertise experience have been developed. The most common NIBP measurement methods are the auscultatory (manual) and oscillometric (automated) BP methods.

(a) Auscultatory BP recording technique

The auscultatory method (also known as the Riva Rocci Korotkoff) is the listening of Korotkoff sounds in the brachial arterial (Fig. 2.17). This is the gold standard for clinical BP measurement that is only performed by trained healthcare providers. The auscultatory method involves first wrapping a cuff around the subject's upper arm. The cuff is connected to a release valve and also a manometer which expresses the pressure in terms of mmHg. A stethoscope will be placed over the antecubital artery below the cuff. Next,

the cuff will then be inflated until the radial arterial pulse disappears. As long as the cuff pressure is more than the brachial arterial pressure, no sound is heard from the stethoscope. The clinician will then slowly release the pressure in the BP cuff. As the cuff pressure decreases, a pounding sound will be heard, and this is known as the Korotkoff sound (K-Sounds).

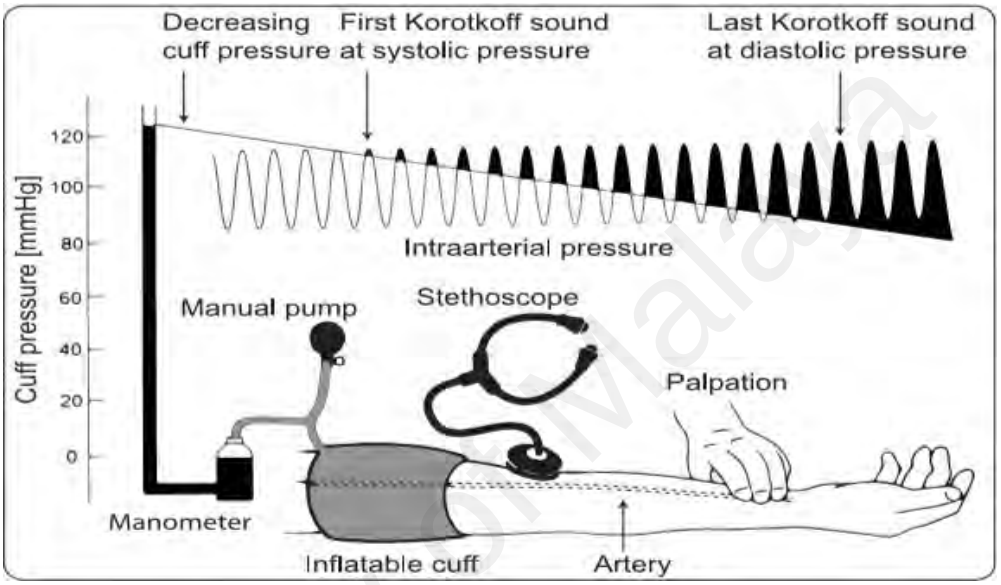

Figure 2.17: Auscultation and palpation principles (Vlachopoulos, O'Rourke, & Nichols, 2011).

These K-Sounds have been classified into five phases (Pickering et al., 2005):

- Phase I: the appearance of clear tapping sounds corresponding to the appearance of a palpable pulse.
- Phase II: the sound becomes softer and longer.
- Phase III: the sound becomes crisper and louder.
- Phase IV: the sound becomes muffled and softer.
- Phase V: the sound disappears completely.

The first K-Sound is defined as SBP. As the pressure continues to fall until the sound disappears, the last K-Sound is defined as DBP. The auscultatory method required the use of a mercury manometer. Mercury is considered as an environment hazard and therefore many countries have started to eliminate this and replace it with

automated BP monitors that do not use mercury. Therefore, in this study, we focus on NIBP that implemented oscillometry techniques.

(b) Oscillometric (automated) BP recording technique

Another type of NIBP measurement is the oscillometric method. Oscillometry is performed in a similar way to the auscultatory method, where a cuff will be placed on the subject's upper arm. However, instead of listening to Korotkoff sounds, oscillometric works by sensing the magnitude of the pressure pulse (known as oscillometric pulses) during the cuff deflation.

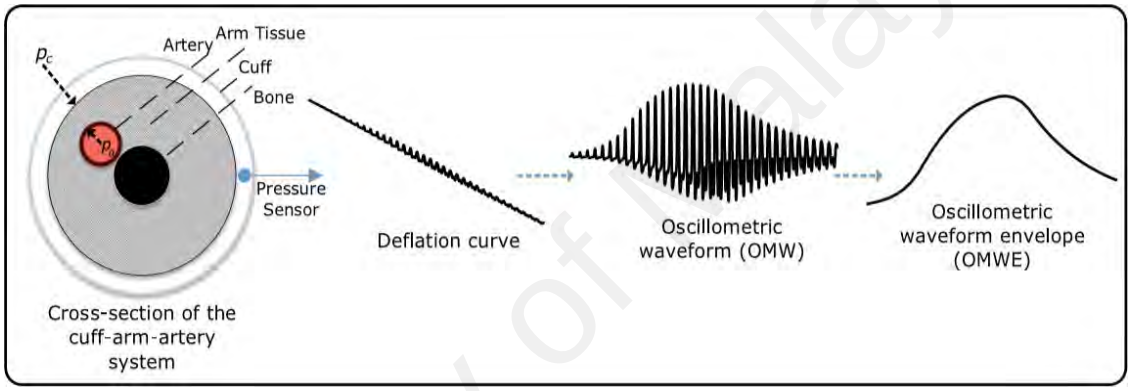

Figure 2.18: Oscillometry system physical setup (Forouzanfar et al., 2015).

Figure 2.18 illustrates the physical setup of the oscillometry system. During the cuff deflation, the recorded pulse pressure forms signals known as the cuff deflation curve. Next, an algorithm was applied to extract this pulse pressure and formed an oscillometric waveform (OMW). Oscillometric waveform Envelope (OMWE) can be used for BP estimation. This is discussed in detail in Section 2.2.2

2.2.2 Systolic/Diastolic BP estimation from oscillometric signal

Different types of algorithms have been applied on the oscillometric signal to estimate BP. Most of the BP estimations were based on the OMWE. We generally classified these algorithms to three categories which are maximum amplitude algorithm (MAA), derivative oscillometry, and machine learning approach.

As the cuff deflates, the time points at which the cuff pressure coincides with the SBP

and DBP were marked. The oscillometric waves superimposed on the cuff pressure were processed to produce the oscillometric waveform envelope (OMWE). Mean arterial pressure (MAP) is defined when the OMWE amplitude increases to its maximum value. The reference systolic BP ratio (SBPR) and diastolic BP ratio (DBPR) were extracted from the OMWE and were defined as follows:

$$SBPR = \frac{SBPA}{MA} \tag{2.3}$$

$$DBPR = \frac{DBPA}{MA} \tag{2.4}$$

where MA represents the maximum amplitude of the OWE corresponding to the location of the MAP, while SBPA and DBPA indicate the amplitudes of the OWE corresponding to the location of the SBP and the DBP respectively. The SBP and DBP are estimated based on the location of MAP. Therefore, MAA is very sensitive to noise and artifacts that may affect the location of MAP (Forouzanfar et al., 2015). Figure 2.19 illustrates an example of the cuff pressure signal, OMW and its corresponding OMWE.

Foster *et al.* (Forster & Turney, 1986) indicated that MAP can be estimated correctly by referring to the maximum of the oscillation amplitude. However, due to the sensitivity of the method to variations in BP waveform, pulse pressure, and arterial compliance, systolic and diastolic pressure may be inaccurate. Besides that, several research have shown that the empirical coefficient (ratio) differs according to different heath care conditions, age group and etc. (Drzewiecki, Hood, & Apple, 1994; J. Liu, Hahn, & Mukkamala, 2013; Raamat, Jagomägi, Talts, & Kivastik, 2013; Talts, Raamat, Jagomägi, & Kivastik, 2011). Lee *et al*. (S. Lee, Rajan, Dajani, Groza, & Bolic, 2011) have tried to use the Bayesian approach to determine the systolic and diastolic ratios. This method assumes that the posteriori distribution of the systolic and diastolic ratios looks like a Gaussian. The likelihood value was chosen to maximise the posteriori probability. Other than that, Gaussian mixture regression techniques have also been used to estimate the

SBPR and DBPR. In this approach, several clusters were built with each representing similar SBP and DBP values. This cluster was identified by using the Gaussian mixture model and followed by using the Gaussian mixture regression technique to acquire the maximum SBPR and DBPR for each cluster. In (S. Lee, Bolic, Groza, Dajani, & Rajan, 2011), Lee *et al.* proposed the use of two-step pseudo-maximum amplitude (TSPMA) to obtain improved confidence intervals (CI) of SBP and DBP using a double bootstrap approach. This method shows a smaller CI as compared to pseudo-maximum amplitude-envelope and maximum amplitude algorithms with Student's t distribution method.

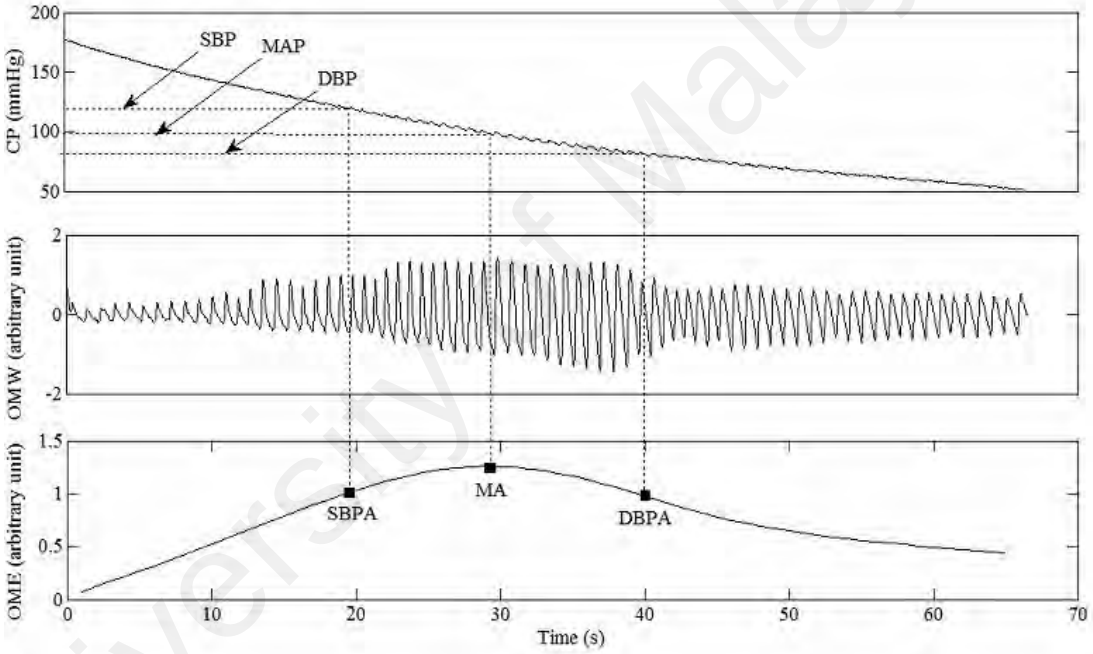

Figure 2.19: An example of the deflating cuff pressure (CP) waveform, pulsatile oscillometric waveform (OMW), and oscillometric waveform envelope (OMWE). MA: Amplitude of the OMWE corresponding to the location of the mean arterial pressure (MAP); SBPA: Amplitude of the OMWE corresponding to the location of the systolic BP (SBP); DBPA: Amplitude of the OMWE corresponding to the location of the diastolic BP (DBP).

The second BP estimation category is derivative oscillometry. Similar to MAA, derivative oscillometry also estimates the BP based on the OMWE. This method estimates the BP based on the slope of the oscillometric envelope instead of the empirical coefficient (ratio) to the maximum amplitude. Drzewiecki *et al.* (Drzewiecki & Bronzino, 2000; Drzewiecki et al., 1994) found that the slope of the OMWE reached maximum

during the SBP while the slope of the OMWE reached its minimum during the DBP. For this method, no empirical coefficient is needed. However, as the slope is derived from the OMWE, the accuracy is highly sensitive to the artifact or noise of the envelope. Besides that, lots of machine learning approaches have been developed to estimate the BP from the OMWE. Neural network (NN) has been used as a non-linear tool to find the relationship between OMWE and BP. For NN, OMWE were used as an input while the BP reading was used as target. Baker *et al*. (P. D. Baker, Orr, Westenskow, & Egbert, 1994) used a two layer feed forward NN to estimate the BP from the superficial temporal artery while Narus *et al.* (Narus, Egbert, Lee, Lu, & Westenskow, 1995) used a three layer feed forward NN from the supraorbital artery. Other than that, Colak *et al.* (S Colak & Can Isik, 2004) used a two layer NN on the upper arm of the subjects and found that the result of NN is better than MAA in terms of standard deviation error (SDE). Using a different approach based on a Fourier series representation of the oscillometric waveform, Barbe *et al.* (Barbe, Van Moer, & Schoors, 2011*)* introduced a Hammerstein-Windkessel model which captures the low frequency oscillations of the cardiovascular system. The systolic and diastolic pressures were derived from the MAP using an intuitive estimator α, which was calculated based on the envelope of the modeled oscillometric waveform. In a more recent study, they (Barbé, Kurylyak, & Lamonaca, 2014) further extended their work to include a statistical learning technique based on ordinal logistic regression for the calibration of oscillometric BP monitors. By applying a linear regression to map the shape of the oscillometric signal to the BP to avoid complex non-linear models, the method could only estimate the correct BP range but not the specific value of the BP. Unlike MAA, NN machine learning algorithms do not depend on the empirical coefficient. Besides that, it is not sensitive to noise like derivative oscillometry. However, this method required a large training dataset, is sensitive to initial network parameters, high computational cost, and there is a lack of a general approach to determine the optimal

network size.

2.2.3 Challenges in oscillometric BP measurement/estimation

2.2.3.1 Challenges due to external factors

The most common error of BP recording is using incorrectly cuff-sized cuffs. An overly small-sized cuff will give a high reading while an overly large-sized cuff will provide a reading that is falsely low. According to the American Heart Association (Pickering et al., 2005), the cuff bladder should encircle 80% or more of the patient's arm circumference. Since this is time consuming, most users skip this procedure.The second most common error in BP measurement is incorrect cuff position. During BP measurement, the cuff should be placed on the arm at the middle of the heart level. If the cuff is placed above the heart level, it will result in low BP and vice versa. Research shows that 2 mmHg of error can occur for each inch of the extremity above and below heart level (Frese, Fick, & Sadowsky, 2011).

During BP measurement, the subject should be seated with his or her back supported, legs uncrossed, arm horizontal to the ground and not talking. Allowing the arm to hang by the side instead of being horizontal can raise the SBP by 23 mmHg and DBP of by 10 mmHg respectively. This margin of error could make a healthy person to appear hypertensive. Meanwhile, crossing the legs can increase SBP by 2 to 8 mmHg (Pinar, Ataalkin, & Watson, 2010).

Another error is operator error. According to the British Medical Journal (Beevers, Lip, & O'Brien, 2001), many operators have a preference to end numbers in 0/5 for BP readings and this always leads to 2 to 3 mmHg error in BP measurement. Besides that, rapid inflation or deflation of cuff pressure can always lead to error in BP measurement.

Another source of recording error is caused by motion artifacts. Asmost BP estimation methods requires the usage of a cuff at the upper arm, any movement will cause the drastic

fluctuations of the measured pressure and this can cause serious distortion to the signal and lead to error in BP estimation.

There are other issues that may affect the BP reading, such as medication, caffeine and the white coat effect. Medication such as Indomethacin and Piroxicam may cause water retention, creating kidney problems and increasing your BP. Moreover, caffeine can cause a short, but dramatic increase in your BP, even if you do not have high BP. However, the reason of the BP changes is unclear (Hartley et al., 2000). The term "white coat" refersto the white coats that are worn traditionally by doctors. Some patients who usually have normal BP show hypertension when they visit the doctor, which also known as the "white coat effect" (Gerin et al., 2006). To avoid all these, multiple readings at different times and locations should be recording before any medical diagnosis.

2.2.3.2 Challenges due to disease conditions

Accurate BP measurements are needed in clinical practice, however, the estimation of BP is difficult in certain patient populations such as patients with obesity (Umana, Ahmed, Fraley, & Alpert, 2006), arterial stiffness (van Popele et al., 2000), and AF (Pagonas et al., 2013; Verberk & De Leeuw, 2012). For these patients, the recorded BP signals may be so weak or in irregular shape and degrade the signal quality, leading to unreliable or wrong BP estimation.

Measuring BP in patients with obesity presents several challenges (Fonseca-Reyes, de Alba-García, Parra-Carrillo, & Paczka-Zapata, 2003; McFarlane, 2012; Umana et al., 2006). A standard cuff size will not be able to fit obese patients due to their large upper arm circumference. Clinicians are having difficulty in finding the right cuff for obese patients. A drop in the accuracy of BP estimation was observed when inappropriate cuff was applied. J. McFarlane *et al.* (McFarlane, 2012) demonstrated the effect of cuff size and cuff position on obese participants (BMI between 36 and 40) in a study. The study

compared the discrepancies of BP measurements obtained from an extra-long cuff on the patient's arm, an appropriately sized cuff on the patient's arm and an appropriately sized cuff on the patient's forearm. Results showed that measurements from the extra-long cuff on the arm position tends to overestimating the BP. Fonseca-Reyes *et al.* also noted that the BP estimation error will increase if the BMI is greater than 40 (Fonseca-Reyes et al., 2003). Other than that, obese patients are normally having cone-shaped arms. The diameter at the top of the arm is greater than the diameter of the arm in the region of the brachial artery. This cause a poor fit of the cuff over the brachial artery and led to inaccurate BP measurement.

Arterial stiffening is always seen in aging populations. During the aging process, the wall of the arteries, especially the aorta, become less elastic and larger in size. This process will increase the pulse wave velocity (PWV) and pulse pressure (PP) (Z. Sun, 2015).The increase of PWV and PP will lead to progressive increase in systolic BP with no changes or even a decrease in diastolic BP which is known as isolated systolic hypertension. Isolated systolic hypertension is defined as SBP > 140 mmHg and DBP < 90 mmHg (Mancia et al., 2014).

Atrial fibrillation (AF) is the most common type of cardiac arrhythmia and it normally comes together with hypertension (Manolis et al., 2012). In the presence of AF, variations in ventricular filling time, stroke volume, and contractility may lead to increased beat-to-beat BP variability, which may affect BP estimation using both the auscultatory and oscillometric methods. There were three studies conducted with 24 hours ambulatory BP monitors (ABPM) that were performed in AF patients (Fonseca-Reyes et al., 2003; McFarlane, 2012; Pagonas et al., 2013). The accuracy of BP recorded was reported around 80% - 93%. Besides that, there were a few studies conducted with home BP monitors. These studies demonstrate satisfactory results with accuracy of more than 92% (Marazzi et al., 2012; Verberk, Omboni, Kollias, & Stergiou, 2016). However, current

guidelines for BP measurement in AF patients recommend that measurements should be taken repeatedly with the auscultatory method (Manolis et al., 2012). Therefore, the automated BP measurement method may be acceptable for self-home and ambulatory monitoring but will not achieve the requirements in a clinical setting. Hence, BP estimation on AF patients remains a challenge until more evidence becomes available.

2.2.4 Artifact detection techniques for BP signal

The performance of BP estimation is highly dependent on the quality of the oscillometric pulse. Since the oscillometric signal is always recorded together with different types of noise such as body movements, environment noise or error created by the operator during BP measurement, an artifact detection or removal stage is required to ensure the signal quality before applying the BP estimation algorithm.

2.2.4.1 Conventional Techniques

The most basic technique used for noise removal is the application of low-pass or band-pass filter to the OMWE (Forouzanfar et al., 2015). For example, Branko *et al.* (Celler, Argha, Le, & Ambikairajah, 2018) used a high-pass filter of 0.7Hz followed by 7Hz low-pass filter to remove the noise from the internal stepper motor. Hidehiko Komine *et al.* 2012 (Komine, Asai, Yokoi, & Yoshizawa, 2012) used a band-pass filter of 0.5 to 10Hz to retain information of the arterial stiffness while (Abolarin et al., 2016) used band-pass filter from 0.5 to 20Hz as it has been found that the BP signal over 20Hz does not contain any useful information. We can see that different types of filter were used as it depends on the artifact and also the feature that we want to preserve.

Another method that is usually used for artifact removal is curve fitting on OMWE. Curve fitting models such as polynomial (Yang, Chen, Zhu, Chen, & Zheng, 2017) (Dingchang Zheng, Amoore, Mieke, & Murray, 2011; D Zheng & Murray, 2008) , Gaussian (Forouzanfar, Dajani, Groza, Bolic, & Rajan, 2011) and log-sigmoid

(Forouzanfar et al., 2014) curve have been used. The performance of the BP estimation is highly dependent on predefined models of the fitting techniques. If the chosen model is not accurate, the shape of the OMWE could be affected and this reduces the performance of BP estimation.

2.2.4.2 BP Artifact removal and detection of motion artifact

Although conventional techniques such as filtering and curve fitting are effective, however, they do not have good performance in the suppression of motion artifacts with low frequency (Forouzanfar et al., 2015). This is because the low frequency artifact may overlap with the fundamental components of the oscillometric pulse. Therefore, different types of algorithms were developed to remove the motion artifact, as described in the following.

Lin *et al.* (Lin, Liu, Wang, & Wen, 2003) developed an algorithm-based fuzzy logic to reduce the interference caused by movement artifacts and cardiovascular disease by determining the truthfulness of the oscillometric pulse. The results proved that this method has improved the accuracy of the BP measurement as compared to the traditional curve fitting method. However, this study does not meet the Association for the Advancement of Medical Instrumentation's (AAMI) standards which required at least 85 subjects (Stergiou, Alpert, Mieke, Wang, & O'Brien, 2018).

Wang *et al.* (S.-H. Liu & Lin, 2001) designed a model-based fuzzy logic control system to measure BP by detecting arterial volume pulsation. A Kalman filter is used to reduce the physiologic and measurement disturbance of the vessel volume oscillation amplitude. The results showed that for the MAP with changing rate of ±10, ±20 or ±30 mmHg, the synthetic fuzzy logic controller would adjust the chamber pressure with a mean square error of 1.9, 2.2 or 2.8 mmHg, respectively. Thomas J. Dorsett (Dorsett, 1991) has developed an algorithm that used the Kalman filter to predict the amplitude of the next

oscillometric pulse and cuff pressure. This algorithm is effective at rejecting motion artifacts and it shows its robustness in ambulatory and helicopter transportation.

Colak *et al.* (S. Colak & C. Isik, 2004) developed a pulse qualifier using fuzzy theory. Pulse features such as shape, height and width were analysed to ensure the quality of each pulse before applying the BP estimation algorithm. Jan Havlík*et al*. (Havlík, Martinovská, Dvořák, & Lhotská, 2014) detected oscillometric artifacts by comparing the HR, HRV and oscillometric pulsations with ECG.

2.2.4.3 Artifact removal using additional sensors

There are also several research works that attempt to reject artifacts by using additional sensors such as ECG (Ahmad et al., 2012), pulse oximeter (Peel III, 1999) and accelerometer (Hasnain, Awan, & Farooq, 2009; Koo et al., 2007) accelerometer. In (Ahmad et al., 2012), an ECG was recorded simultaneously with the oscillometric pulses. The ECG signals were then used as a reference signal to assist the identification of the true oscillometric pulse. Harry *et al.* invented an arrhythmia pulse correcting circuit that corrects the amplitudes of oscillometric pulses produced by arrhythmias with the help of ECG and the pulse oximeter. Kunseo *et al.* (Koo et al., 2007) and Hasnain *et al.* (Hasnain et al., 2009) have developed a new NIBP system to reject motion artifacts by mounting a 3-axis accelerometer on a cuff. Next, an algorithm was developed to construct motion artifacts that were superimposed over the oscillmetric signal based on the recorded acceleration. This constructed motion artifacts were used to remove the motion artifact. Since an extra sensor is needed for the artifact removal, this may increase the computational time and cost. Besides that, it will also increase the complexity of the algorithm.

2.3 Photoplethysmography (PPG) signal

PPG is a signal as shown in Figure 2.20, obtained by using a simple non-invasive

optical technique. It has become popular since it provides valuable information about the cardiovascular system by simply making measurements on the skin surface. Many physiological parameters have been studied and derived from PPG signals, such as blood–oxygen saturation, HR, RR and BP. Patients at the risk of respiratory failure (Uçar, Bozkurt, Bilgin, & Polat, 2017), hypoxemia (Hartmut Gehring, ME, & Schmucker, 2002) or cardiac problems (Ave, Fauzan, Adhitya, & Zakaria, 2015) can easily be detected by clinicians through observing the changes in PPG signals. On top of that, cardiopulmonary diseases and sleep disorders can also be screened (J. L. Moraes et al., 2018).

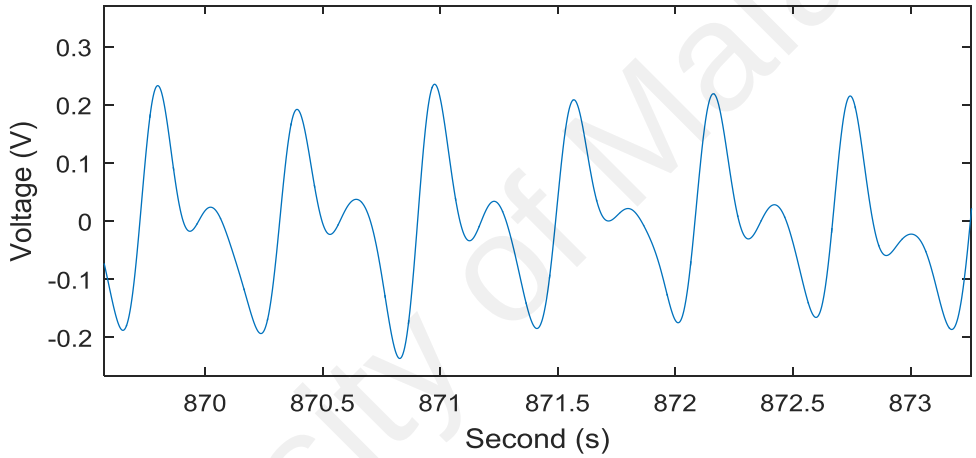

Figure 2.20: A clean PPG signal.

2.3.1 Techniques of measurements

PPG uses a probe which contains a light source (a red and infrared light-emitting diode (LED)) and a photodetector to detect the cardiovascular pulse wave that propagates through the body. There are two methods to measure PPG: transmission and reflectance. For transmission PPG, the light source and photodetector are opposite to one another with the measuring site in between as shown in Figure 2.21. The light can then pass through the biological tissue and be detected by the photodetector at the opposite side.

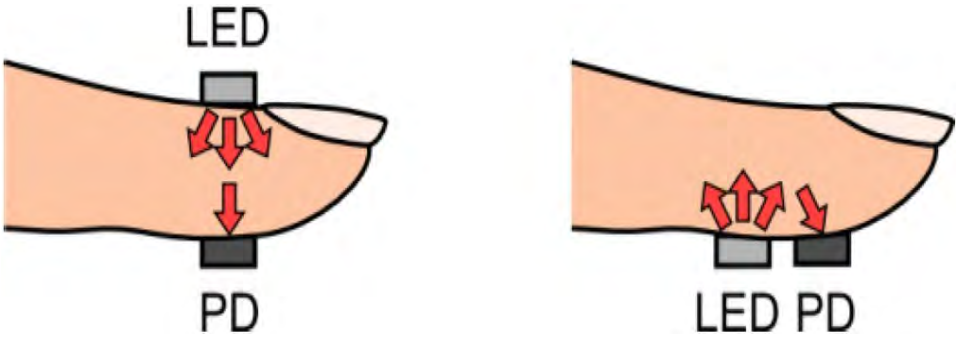

Figure 2.21: Light-emitting diode (LED) and photodetector (PD) placement for transmission- and reflectance-mode PPG (Tamura, Maeda, Sekine, & Yoshida, 2014).

Transmission PPG is mostly used in finger and earlobe PPG (Da He, Winokur, Heldt, & Sodini, 2010; Guo et al., 2008; Hashem, Shams, Kader, & Sayed, 2010; Verma & Bhasin, 2014). For reflection PPG, the light source and photodetector are next to each other as shown in Figure 2.21. The light bounced by the biological tissue will be reflected to the photodetector located next to the light source. This method is mostly applied on one side of the skin, for example: inner ear and forehead.

The PPG signal is comprised of Direct Current (DC) non-pulsatile waveform and Alternating Current (AC) pulsatile waveform. The light that is emitted to the biological tissues was absorbed by different substances, including skin pigments, bones, venous and arterial blood. These act as the DC components in the PPG signal and it is assumed to be constant all the time. However, when the blood moves from the heart to the fingers and toes, the changes of blood volume will generate a pulsatile signal which is also known as the AC component. This AC component is superimposed with the DC component and generate the PPG signal as shown in the figure below.

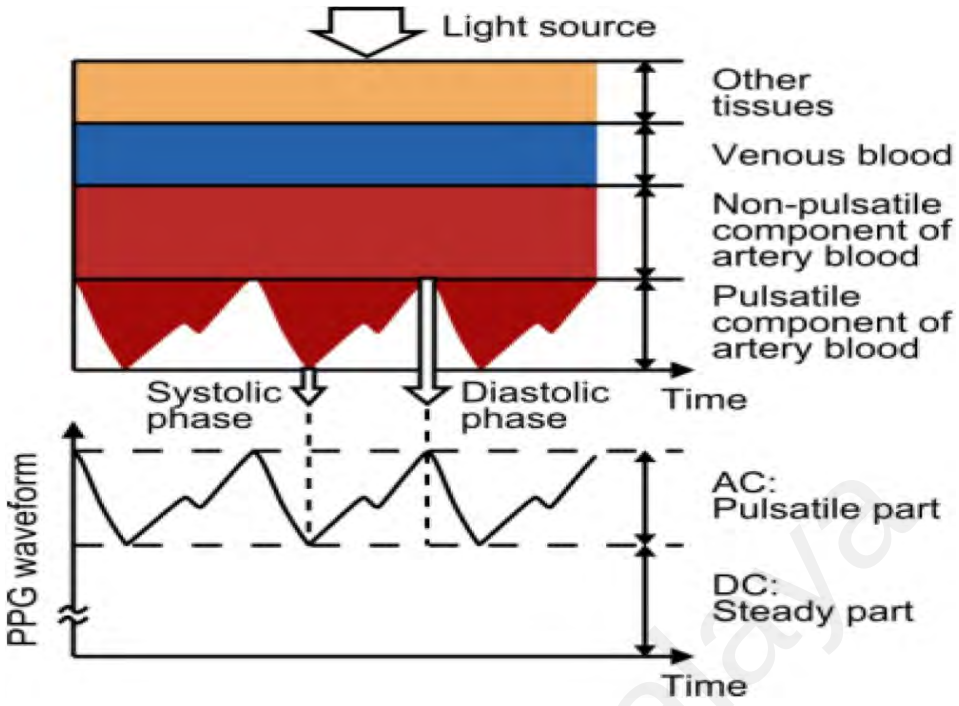

Figure 2.22: Light attenuation and the PPG signal (Tamura et al., 2014).

2.3.2 Applications of PPG signal

PPG has been widely used as it is a low-cost, simple, non-invasive and portable technology. It has always been used in primary care as it can provide valuable information about the cardiovascular system. Clinically important information that can be extracted from PPG are blood oxygen saturation, HR, RR and BP.

Oxygen saturation (SpO2) measures the percentage of oxygenated hemoglobin in the blood stream. It can be a useful indicator of the circulatory and respiratory system. Normal blood oxygen level in the human body is between 95 to 100% (Harvey, Salehizadeh, Mendelson, & Chon, 2018; Organization, 2011; Rasoul Yousefi, Nourani, Ostadabbas, & Panahi, 2013), and the oxygen level below 90% indicates hypoxemia. If the blood oxygen level falls below 80%, this can lead to brain and heart damage. Moreover, continued low oxygen may lead to respiratory or cardiac arrest. Oxygen saturation is defined as the ratio of oxygenated hemoglobin relative to total haemoglobin (oxygenated + deoxygenated) in the blood, as expressed below:

$$SpO_2 = \frac{HbO_2}{HbO_2 + Hb} \quad (2.5)$$

The pulse oximeter that is based on the red (light wavelength of 600 to 750nm) and infrared light (light wavelength of 850 to 1000nm) absorption characteristic can be used to estimate SpO_2. Oxygenated haemoglobin (HbO_2) absorbs more infrared light and allows more red light to pass through while deoxygenated haemoglobin (Hb) absorbs more red light and allows more infrared light to pass through.

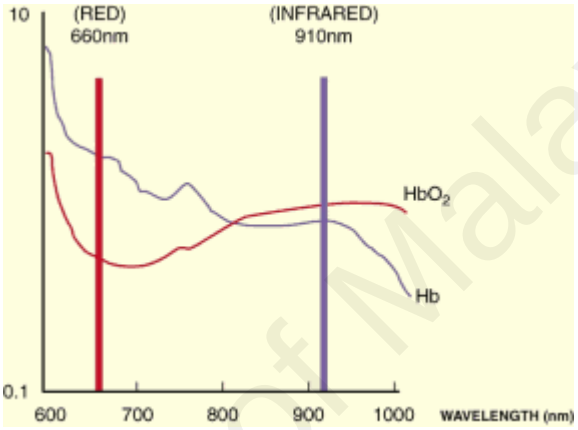

Figure 2.23: Absorption of oxygenated haemoglobin (HbO2) and deoxygenated haemoglobin (Hb) at different light wavelengths (Kaur, Kumar, & Sharma, 2011).

HR can be simply derived from PPG signals by simply calculating the pulse width (PW) which is the time interval between two peaks or troughs. Since PPG is cheap and non-invasive, it has been widely used to derive HR apart from ECG (Georgiou et al., 2018).

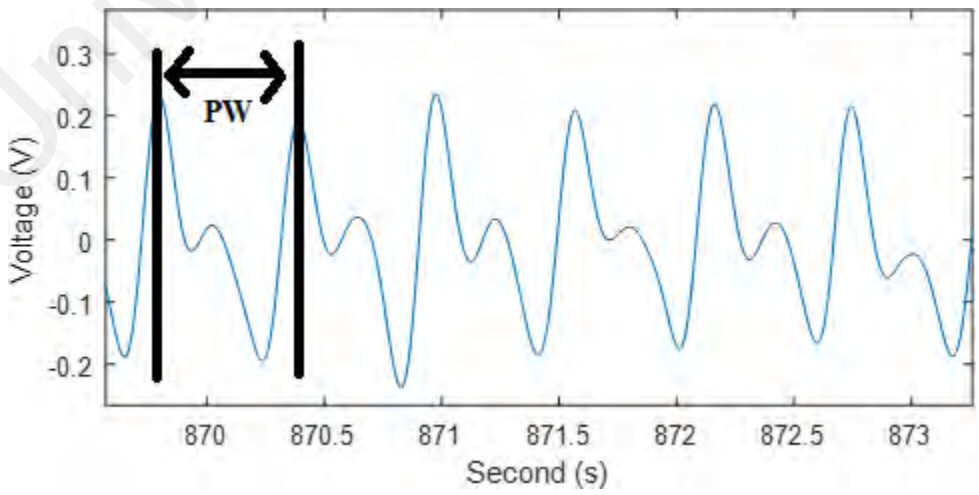

Figure 2.24: PPG signal with pulse width.

$$Heart\ Rate = 60/PW \tag{2.6}$$

Many researchers have attempted to acquire RR information from a PPG signal using different signal processing methods such as Principal component analysis (PCA) (Madhav, Ram, Krishna, Reddy, & Reddy, 2010; Prathyusha, Rao, & Asha, 2012), Empirical mode decomposition (EMD) (Prathyusha et al., 2012), wavelet transform (Addison & Watson, 2004), the Teager-Kaiser energy operator (Nguyen, Le Page, Goujon, Poffo, & Thual, 2011), variable frequency complex demodulation (Chon, Dash, & Ju, 2009; Nam, Lee, & Chon, 2014), the Hilbert transform (Li, Zhao, & Dou, 2015), or the synchro-squeezing transform (Dehkordi et al., 2015). The PPG signal consists of a repeated, double peak waveform riding on a constant DC baseline component as shown in Figure 2.25(a). However, in practice, both the PPG pulse and DC are changing over time. This variation is caused by different factors such as changes in cardiac output, changes in BP, changes in HR and respiratory activity. Respiratory activity usually affects the PPG signal in three ways: (i) Baseline Modulation-PPG pulse riding on top of the changing dashed DC baseline; (ii) Pulse Amplitude Modulation - PPG pulse amplitude changing over the respiratory cycle; and (iii) Pulse Frequency Modulation which is also known as Respiratory Sinus Arrhythmia (RSA) - PPG pulse period changing over the respiratory cycle, which shown in Figure 2.25.

BP is one of the health indicators that can be derived from the PPG signal. Traditionally, pulse transit time (PTT) (R. a. Allen, Schneider, Davidson, Winchester, & Taylor, 1981; L. Geddes, Voelz, Babbs, Bourland, & Tacker, 1981; Naschitz et al., 2004; Obrist, Light, McCubbin, Hutcheson, & Hoffer, 1979; Payne, Symeonides, Webb, & Maxwell, 2006) which is highly related to BP changes has always been used to predict BP (Gao, Olivier, & Mukkamala, 2016; Gao, Zhang, Olivier, & Mukkamala, 2013; L. A. Geddes, Voelz, James, & Reiner, 1981; Ochiai et al., 1999; Pruett,

Bourland, & Geddes, 1988). PTT is defined as the time delay between the invasive proximal arterial waveform and distal pressure waveform in central arteries. To decrease inconvenience, researchers have used the ECG to represent the proximal arterial waveform while the PPG signal at the finger is to represent the distal waveform (Gao et al., 2016). In this case, PTT will be known as pulse arrival time (PAT) (W. Chen, Kobayashi, Ichikawa, Takeuchi, & Togawa, 2000; L. Geddes et al., 1981). The figure below shows the PAT measured between R peak of ECG and a point of PPG signal.

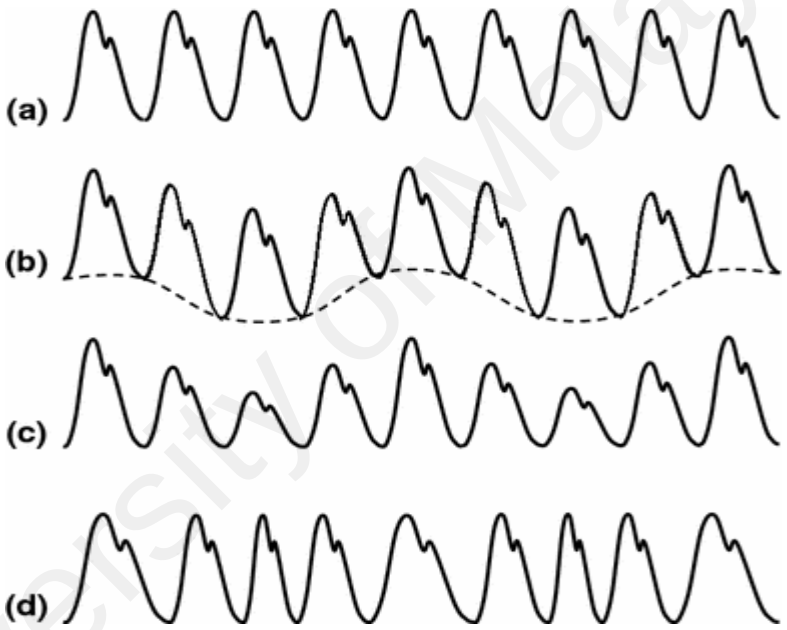

Figure 2.25: Effect of PPG signal by respiratory rate (Addison, 2017). Non-modulated PPG signal. (b) Baseline Modulation. (c) Pulse Amplitude Modulation. (d) Pulse Frequency Modulation.

By using the PAT, different studies were carried out by researchers to find the relationship between BP and PAT such as Fourier transforms (FFT) (Xing & Sun, 2016) and NN (John Allen & Murray, 1999). Reasonably good results were shown in the studies.

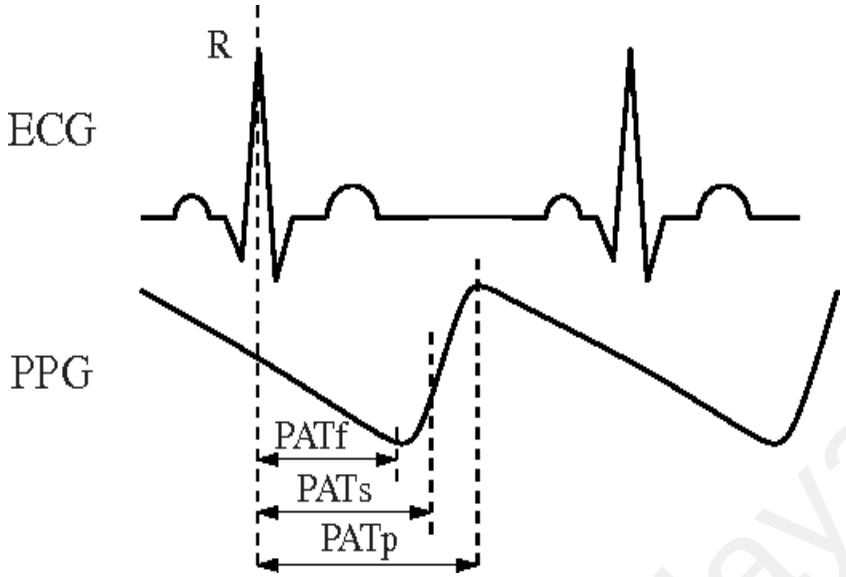

Figure 2.26: PAT measured between R peak of ECG and a particular point of PPG signal, such as foot (PATf), peak (PATp) or maximum slope point (PATs) (Cattivelli & Garudadri, 2009).

2.3.3 Challenges in PPG signal recording/processing

2.3.3.1 Challenges due to external factors

The signal quality of PPG is affected by the location of the LED and photodetector. The location of the measurement site of the probe must be placed to optimise the sensor performance. In recent years, different measurement sites for PPG sensors have been explored. These include ring finger (Rhee, Yang, & Asada, 2001), wrist (Y. Lee, Shin, Jo, & Lee, 2011), brachia (Maeda, Sekine, & Tamura, 2011a, 2011b; Maguire & Ward, 2002), earlobe (Poh, Swenson, & Picard, 2010; K. Shin, Kim, Bae, Park, & Kim, 2009; Vogel, Hülsbusch, Hennig, Blazek, & Leonhardt, 2009), external ear cartilage (Budidha & Kyriacou, 2014; Celka, Verjus, Vetter, Renevey, & Neuman, 2004; Poh, Kim, Goessling, Swenson, & Picard, 2010), and the superior auricular region (Patterson, McIlwraith, & Yang, 2009; C.-Z. Wang & Zheng, 2008; L. Wang, Lo, & Yang, 2007). Commercial PPG sensors on the finger, earlobe and forehead are available in the market (Mendelson & Pujary, 2003) while PPG signals are collected from the esophageal region clinical practice (P. Kyriacou et al., 1999; P. A. Kyriacou, 2013; P. A. Kyriacou, Powell, Langford, & Jones, 2002). Ethel *et al*. have shown

that out of the 52 anatomic sites, fingers, palm, face and ear have higher perfusion values as compared to other measurement sites (Tur, Tur, Maibach, & Guy, 1983).

The PPG signal is affected by the contact force between the sensor and the measurement site. The PPG signals vary with the PPG probe contact pressure. A low contact force will result in low AC signal amplitude due to insufficient contact. However, high contact force will also lead to low AC signal amplitude due to the occlusion of the artery. The ideal PPG signal can be acquired when the pressure difference between the inside and the outside of the vessel are the same (Tamura et al., 2014).

Ambient light intensity can be a main interference component in PPG data acquisition. Whenever ambient light source such as the sun or fluorescent lamp is present, this will lead to unbalanced or uncertain variation of light intensity. This is both reflected in the alternating current (AC) and direct current (DC) components. DC offset depends on the static ambient light intensity and skin colour. A strong constant (DC) ambient light can saturate the photodetector and end up with an undetectable PPG signal. Research has also shown that by increasing light intensity, there is an increase in DC amplitude while the AC component shows an initial increase followed by decrease.

Motion artifacts may occur from voluntary or involuntary subject movement (Foo & Wilson, 2006; Matthew James Hayes & Smith, 2001). When movement occurs, the contact force between the sensor and the measurement site may have considerable effect, causing changes of light intensity and disturbing the PPG signal. Besides that, movement will cause the changes of blood volume in venous and arterial blood, as well as other normally non- pulsatile components (such as tissue fluid in edematous patients) (Petterson, Begnoche, & Graybeal, 2007). This leads to differences as

compared to normal resting conditions. Thus, the PPG signal components may no longer have good quality to represent the pulsatile arterial blood flow.

2.3.3.2 Challenges due to disease conditions

PPG is a non-invasive optical technique to detect changes of blood volume in the tissue. The shape of the PPG signal is dependent on several factors such as one's tissue properties and health condition (Chan et al., 2012; Yuan et al., 2017). Lots of valuable information about the cardiovascular system can be acquired from the PPG signal. However, the challenge in analysing the PPG signal has increased with the occurrence of different types of diseases. In this section, two types of diseases which relate to peripheral blood vessels or cardiovascular system is discussed, including, ageing and arrhythmia. For such patients, the PPG signals are different and the normal equation to estimate SpO2 and HR from the PPG signals may not be applicable. Patient specific calibration may be needed to ensure accuracy.

Ageing has the most noticeable and consistent effect on the PPG signal. As an individual gets older, arteriosclerosis thickens and hardens the walls of arteries and this leads to an early return of the reflection wave of the diastolic peak. As we can see in Figure 2.27, systolic (first peak) and diastolic (second peak) is very obvious in younger subjects (Millasseau, Kelly, Ritter, & Chowienczyk, 2002). In older subjects, by constract, the systolic peak is steeper with almost no diastolic peak. This may be caused by the existence of cardiovascular complications such as wall stiffness and also reduction in systemic vascular compliance. As a consequence, some shape deriving features relevant to SpO_2 estimation are seriously affected.

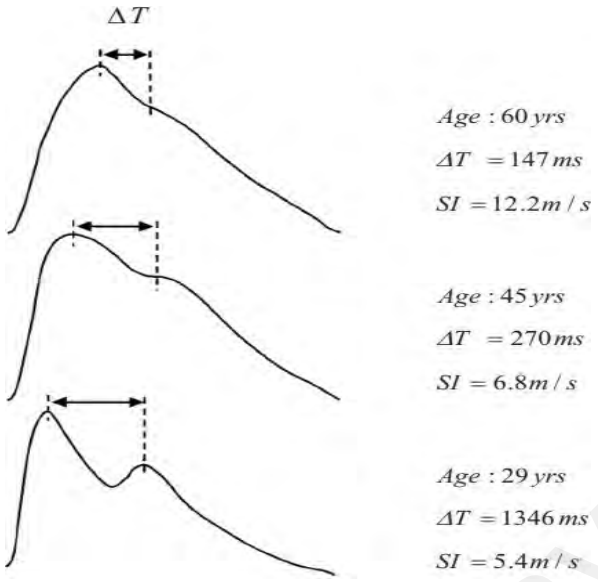

Figure 2.27: Typical PPG signals show the parameters changes with age (Millasseau et al., 2002).

One of the most common cardiovascular diseases is cardiac arrhythmia. In the presence of arrhythmia, the heart rhythm could be faster than normal, slower than normal or having an irregular pattern. The variations in ventricular filling time, stroke volume, and contractility may lead to variations in pulse to pulse. As shown in Figure 2.28, both types of arrhythmia have a significant impact on the morphology of the PPG signal. The occurrence of the second peak is a challenge for the algorithm to differentiate it from the normal PPG signal. The algorithm may misclassify this pulse as dicrotic notches or motion artifacts. As a result, some time deriving features for pulse arrival time and heart beat estimation are seriously affected.

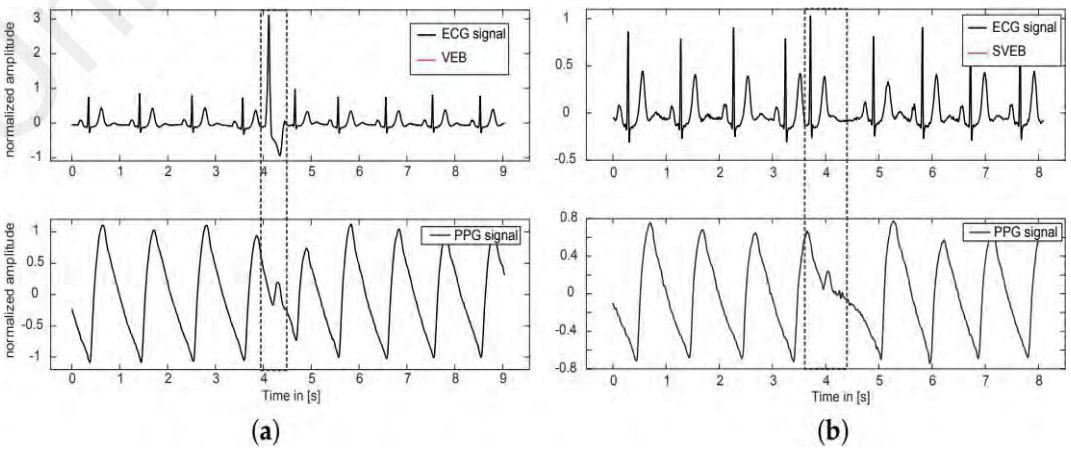

Figure 2.28: Synchronised ECG and PPG signals. (a) Single premature ventricular ectopic beat at t = 4s; and (b) single premature supraventricular ectopic beat at t = 3.8s (Pflugradt, Geissdoerfer, Goernig, & Orglmeister, 2017).

2.3.4 Artifact detection techniques for PPG signal

There is growing interest to use the PPG signal for further analysis such as extraction of HR (Askarian, Jung, & Chong, 2019; Chowdhury, Hyder, Hafiz, & Haque, 2018; Reiss, Indlekofer, Schmidt, & Van Laerhoven, 2019) and oxygen saturation level (Abay & Kyriacou, 2018; Longmore et al., 2019). However, it is well known that the PPG signal is easily corrupted by noise. Various artifact reduction algorithms were previoisly proposed to reduce the artifacts such as moving average (H.-W. Lee, Lee, Jung, & Lee, 2007), independent component analysis (ICA) (Kim & Yoo, 2006) ,wavelet transform (C. Lee & Zhang, 2003), adaptive filters (Madhav et al., 2010; Rasoul Yousefi et al., 2013) and Fourier series analysis (Reddy, George, & Kumar, 2008). However, these algorithms were applied on both clean signals and artifact signals. It might cause unnecessary distortion to the clean signal. Therefore, an artifact detection algorithm which can separate clean signal from the artifact is desirable.

Many authors tried to differentiate the artifacts based on waveform morphology. Li *et al.* (Q. Li & G. D. Clifford, 2012) developed four signal quality metrics, including direct matching, linear resampling, dynamic time warping, and clipping detection, and fused these signal quality informations for artifact classification using the machine learning method. Sukor *et al*.(Jumadi Abdul Sukor, 2012) extracted five different features from the PPG signal, which comprises of the amplitude, trough depth difference, pulse width, Euclidean distance with the average of previous pulses, as well as amplitude ratios. A decision tree was then used to classify the pulse. Fischer *et al*. (C Fischer, Glos, Penzel, & Fietze, 2017) proposed an artifact detection method based on a contour analysis in the time domain such as amplitude, duration, and rise time. Chong *et al*. (Chong et al., 2014) tried to compute four time-domain parameters such as standard deviation of peak-to-peak intervals, standard deviation of peak-to-peak amplitudes, standard deviation of systolic and diastolic interval ratios, and mean standard deviation of pulse shape. Support vector

machine (SVM) was be applied to build a decision boundary for classification of pulses into clean and artifact signals. Karlen *et al*. (Karlen, Kobayashi, Ansermino, & Dumont, 2012) and Orphanidou *et al*. (Orphanidou et al., 2014) assessed the quality of PPG signals by comparing each pulse to a reference template, generated from a number of preceding good pulses. Cherif*et al.* (Cherif, Pastor, Nguyen, & L'Her, 2016) detected PPG artifacts by comparing the pulse to the template using correlation coefficient values. Then, a detection method based on Random Distortion Testing (RDT) was used to perform adaptive thresholding for each record.

Emad *et al.* (Kasaeyan Naeini, Azimi, Rahmani, Liljeberg, & Dutt, 2019) employed the Convolutional Neural Network (CNN) deep learning algorithm to learn a customized hypothesis function from the PPG signals. The PPG pulse was first fed into the CNN without undergoing any feature extraction. Next, the signal was labelled as "reliable" or "unreliable". During the learning process, the quality of the PPG signal was evaluated by referring to a set of Electrocardiogram (ECG) signals, and comparing the heart rates extracted from the PPG signal with that obtained from the ECG signal.

Besides that, some of the studies also work on statistical measures such as skewness, kurtosis, Shannon entropy (SE), and Renyi'sentropy (Selvaraj, Mendelson, Shelley, Silverman, & Chon, 2011). Selvaraj 2011 (Selvaraj et al., 2011) computed the kurtosis and SE measurement from the PPG segments while Shao 2017 (Hanyu & Xiaohui, 2017) classified the artifacts by computing kurtosis, skewness and standard deviation. Since PPG amplitude varies among subjects, it is difficult to get high accuracy by using only PPG morphology. Therefore, statistical algorithms were used to differentiate the pulse by assuming that clean and corrupted PPG signals come from two different frequency groups.

Another approach is to use frequency domain analysis to detect PPG artifacts. Hjorth

proposed Hjorth parameters to quantify the degree of oscillation in a signal, where H1 and H2 represent central frequency and half of the bandwidth of a signal, respectively (Hjorth, 1970, 1973). Gilt *et al*. (Gil, Vergara, & Laguna, 2008) further applied this theory on PPG signals with a hypothesis that H1 and H2 derived from noise-contained signals would be largely different from H1 and H2 derived from noise-free PPG signals.

Some studies also perform artifact detection by using both time and frequency analyse. Couceiro proposed an artifact detection algorithm by analysing the variations in the time and period domain characteristics of the PPG signal. The extracted features are ranked using a feature selection algorithm (NMIFS) and the best features are used in Support Vector Machine classification model to distinguish between clean and corrupted sections of the PPG signals. Krishnan *et al*. (Krishnan, Natarajan, & Warren, 2008) used a sensor fusion approach combining high order statistical features from the time and frequency domains to discriminate corrupted PPG sections. Dao *et al. (Dao et al., 2016)* proposed an algorithm for motion artifact detection using time-frequency features. Their approach requires 8s of data, calculates the spectrum of five 4s wide sliding analysis windows (with a 3s overlap between adjacent windows). Variation across these five spectral estimates indicate the presence of signal artifacts. Bashar et al. used variable frequency complex demodulation (VFCDM) technique to differentiate segments containing artifact from clean PPG segments based on spectral characteristics. Three features, i.e. the root mean square of successive differences, Shannon entropy and sample entropy, were extracted and fed into the linear support vector machine (SVR) classifier to distinguish the clean segments from the corrupted sections of the PPG signal (Bashar, Han, Soni, McManus, & Chon, 2018).

On the other hand, several studies have used additional reference signals to detect PPG motion artifact. These studies indicated that motion artifact can be captured using sensors such as gyroscope (Casson, Vazquez Galvez, & Jarchi, 2016; Jarchi & Casson, 2016),

multi-channel PPG (Chowdhury et al., 2018; Fallet & Vesin, 2017; Lei, Lo, & Guang-Zhong, 2007; R. Yousefi, Nourani, Ostadabbas, & Panahi, 2014; Zhang et al., 2019), ECG (Rundo, Conoci, Ortis, & Battiato, 2018) and accelerometer (Pereira et al., 2020; Vandecasteele et al., 2018). Using a combination of the time-frequency spectrum of the PPG-signal and tri-axial acceleration as inputs to the CNN, Attila Reiss *et al.* (Reiss et al., 2019) demonstrated a reduction in the mean absolute error by 31% on the new dataset *PPG-DaLiA*, and 21% on the *WESAD* dataset.

As we have seen, there are many different methods and approaches to perform artifact detection for PPG signals. Every method has its own advantages and drawbacks, but all of them have some limits and issues in common. First, the proposed algorithm identifies the artifact segment by segment and not pulse by pulse. This means that if those segments of data consist of both good and bad pulses, part of these segments might be misclassified. Besides that, only a few studies have considered data with artifacts. Most of the algorithms are only applied on ICU data where the patient is highly immobile with a small amount of artifacts. Next, some of the algorithms were patient-specific; it might not work on different types of data source. Besides that, most of the algorithms only used a short segment of data (less than 5mins) and this is not suitable to be applied on continuous data.

2.4 Chapter summary

Telehealth involves remote monitoring of physiological data. These data are transferred to health care professionals for monitoring. As the physiological data are normally collected from the patient in an unsupervised environment, the data frequently contains a lot of artifacts as compared to those physiological data acquired by clinicians in controlled environment. As physiological signals play an important role in clinical diagnosis, it is crucial to evaluate signal quality before making any important clinical decision.

Up to date, some manufacturers have acknowledged the presence and deteriorating effects of motion artifacts and implemented proprietary algorithms in their devices, whereby, their methods were not made known to the public. Different types of artifact detection methods have been proposed but most only focused on ICU data where patients were highly immobile. Limited studies have focused on artifact detection and removal in unsupervised environment. Therefore, the robustness of these algorithms in the presence of motion artifacts remains to be investigated.

In addition, different disease conditions also affect the quality of physiological signals. The ability of these algorithm in differentiating the artifact from different disease conditions remains to be studied.

CHAPTER 3: SIGNAL QUALITY ASSESSMENT FOR UNSUPERVISED BLOOD PRESSURE MEASUREMENT

3.1 Introduction

This chapter introduced an automatic algorithm to detect and remove artifact in continuous oscillometric BP measurements. Three BP measurement algorithms (MAA, MLR and SVR) were used to estimate SBP and DBP values in the oscillometric waveform corrupted with artifacts. Effect of noise detection (outlier removal) on the performance of the BP estimation algorithm were then presented.

3.2 Literature review

BP, commonly expressed in terms of systolic (maximum) and diastolic (minimum) pressures, offers important insights into cardiovascular health. High BP (hypertension), which may lead to stroke and heart failure, has been rated as one of the most important causes of premature death by the World Health Organization ("World Heart Federation," 2017). On the other hand, excessively low BP (hypotension) may indicate underlying diseases such as heart failure and adrenal insufficiency (Gupta & Lipsitz, 2007; Landgraf, Wishner, & Kloner, 2010). Thus, noninvasive measurement of BP using either auscultatory or oscillometric methods are routinely performed (Perloff et al., 1993).

For the oscillometric method, the Systolic Blood Pressure (SBP) and Diastolic Blood Pressure (DBP) values are usually estimated from the oscillometric waveform envelope (OMWE) using the maximum amplitude algorithm (MAA) either with the slope-based or height-based method (Jazbinsek, Luznik, Mieke, & Trontelj, 2010). The estimation of SBP and DBP using this experimentally-derived, quasi-empirical characteristic ratio is prone to error as it is subject to significant continuous variability over time(S. Lee, S. Rajan, et al., 2011; J. Liu et al., 2013; Soueidan, Chen, Dajani, Bolic, & Groza, 2012). Furthermore, the characteristic ratio has been reported to be sensitive to changes in physiological conditions, in particular the degree of arterial stiffness (Babbs, 2012; J. Liu

et al., 2013; van Popele et al., 2000). For instance, the fixed-ratio method overestimates SBP but underestimates DBP in individuals with stiffening of the brachial artery (J. Liu et al., 2013). Despite these findings, very limited studies have assessed alternative methods to improve the accuracy of SBP and DBP measurements. Feature-based Gaussian mixture regression approach (S. Lee, Chang, et al., 2013), as well as neural networks (Forouzanfar et al., 2011), Bayesian models (S. Lee, Jeon, & Lee, 2013), and a statistical learning techniques based on logistic regression (Barbé et al., 2014) were among the alternative methods. Five features, such as mean arterial pressure (MAP), maximum amplitude, length of the maximum amplitude's position, length of OMWE maximum amplitude, length of the maximum amplitude's position, length of OMWE and asymmetry ratio of the OMWE were used to estimate SBP and DBP using the Gaussian mixture regression model (S. Lee, Chang, et al., 2013).

In this chapter, we evaluated the performance of ten features from the OWE, which included previously used features in addition to newly proposed features, in describing the systolic (SBPR) and diastolic blood pressure ratio (DBPR). Furthermore, we attempted to minimize the usage of multiple features by applying the sequential forward floating selection (SFFS) method and to identify the combination of features that result in the best performance. Two different models, using multiple linear regression (MLR) and support vector regression (SVR) methods were used to estimate SBP and DBP. Carefully designed experiments were performed to obtain noise-free signals and signals containing noise induced by movement so as to evaluate the robustness of the algorithm to motion artifact in an unsupervised environment. A pre- processing step was carried out to detect and eliminate data points corrupted by movement artifact.

3.3 Methods

Figure 3.1 shows the sequence of events in BP estimation.

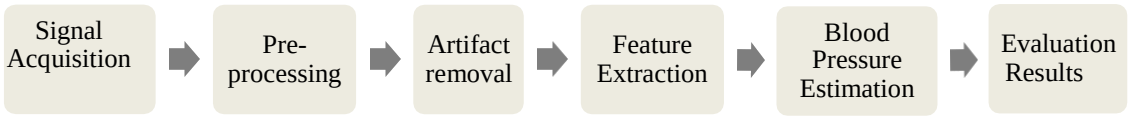

Figure 3.1: Block diagram of sequence of events in BP estimation.

3.3.1 Raw Signal Acquisition

The experimental data were obtained from 25 healthy subjects aged 28 ± 5 years (16 females). Four sets of measurements (two from each arm), which contain simultaneous ECG, cuff pressure and Korotkoff sound were acquired from each volunteer, resulting in a total of 100 measurements. Our data were acquired using an automated BP measurement system with a cuff pressure recorder, a stethoscope with a built-in microphone to capture the auscultatory waveform, together with an ECG recorder. All the signals were acquired simultaneously using a data acquisition system with a sampling rate of 1 kHz. To acquire the oscillometric pulse, the cuff pressure was first increased to approximately 180 mmHg, followed by deflation of the cuff pressure using a release valve, which reduced the pressure to approximately 40 mmHg in a linear fashion and with a rate of 2–3 mmHg/s. To investigate the robustness of the BP estimation algorithm, one of the two measurements on each arm was intentionally contaminated with movement artifact during cuff deflation. The movements were selected from the following options: (1) gently lift the ipsilateral arm, then return to a resting position; (2) spontaneously move the ipsilateral arm right and left; (3) bend the ipsilateral arm and then return to a resting position; (4) tap the stethoscope bell three times with the contralateral hand; (5) squeeze and release the ipsilateral fingers; (6) lift and replace a book with the ipsilateral hand; (7) spontaneously shake the ipsilateral arm for a few seconds; and (8) suddenly remove the cuff. The recorded Korotkoff sound was used by two clinical experts as the basis for estimating the reference SBP and DBP as a reference system (RS). Out of the 100 signals,

only 81 SBP and 84 DBP were available for this study due to a lack of reference reading in the remaining samples, in which the clinical experts were unable to identify the SBP and DBP accurately due to the presence of a large amount of noise in the Korotkoff sound. Figure 3.2 shows the distribution of SBP, DBP and pulse pressure (PP) in the collected data. A more detailed description of the experimental protocol as well as equipment configuration are provided in (J Abdul Sukor, Redmond, Chan, & Lovell, 2012).

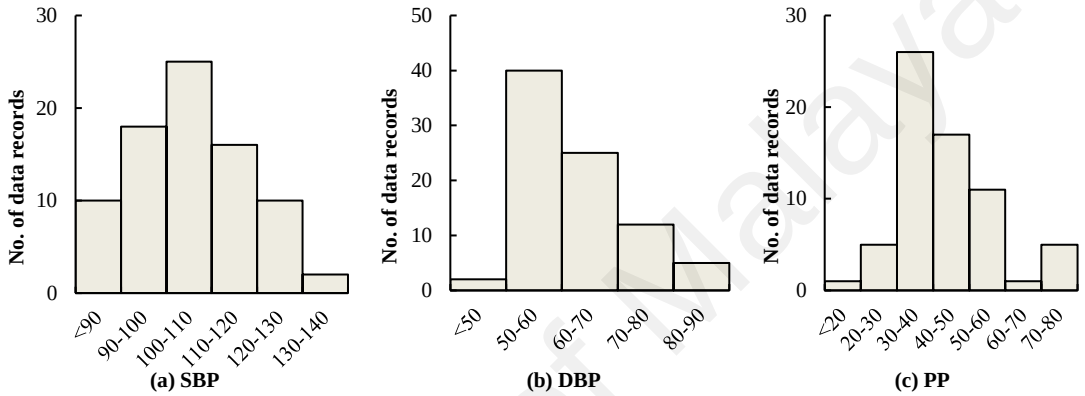

Figure 3.2: Distribution of (a) Systolic Blood Pressure (SBP). (b) Diastolic Blood Pressure (DBP). (c) Pulse Pressure (PP).

3.3.2 Pre-Processing

The cuff pressure signal was detrended using a first-order band-pass Butterworth filter of 0.5–5 Hz, chosen based on the assumption of a maximum heart rate of 300 beats per minute (Jumadi Abdul Sukor, 2012) transform the signal morphology into a pulsatile oscillometric waveform. A forward-backward filter was used to achieve a zero-phase response. Since the ECG signals were not affected by the movement of the subjects, the intervals between two consecutive R-peaks in the ECG waveforms were used to determine each cardiac cycle. Figure 3.3 illustrates an example of the cuff pressure signal, pulsatile oscillometric waveform and its corresponding OMWE. The reference SBPR and DBPR were extracted from the OMWE and were defined as follows:

$$SBPR = \frac{SBPA}{MA} \tag{3.1}$$

$$DBPR = \frac{DBPA}{MA} \tag{3.2}$$

where MA represents the maximum amplitude of the OMWE corresponding to the location of the MAP, while SBPA and DBPA indicate the amplitudes of the OMWE corresponding to the location of the SBP and the DBP during cuff deflation. Mean arterial pressure (MAP) is defined when the OMWE amplitude increases to its maximum value.

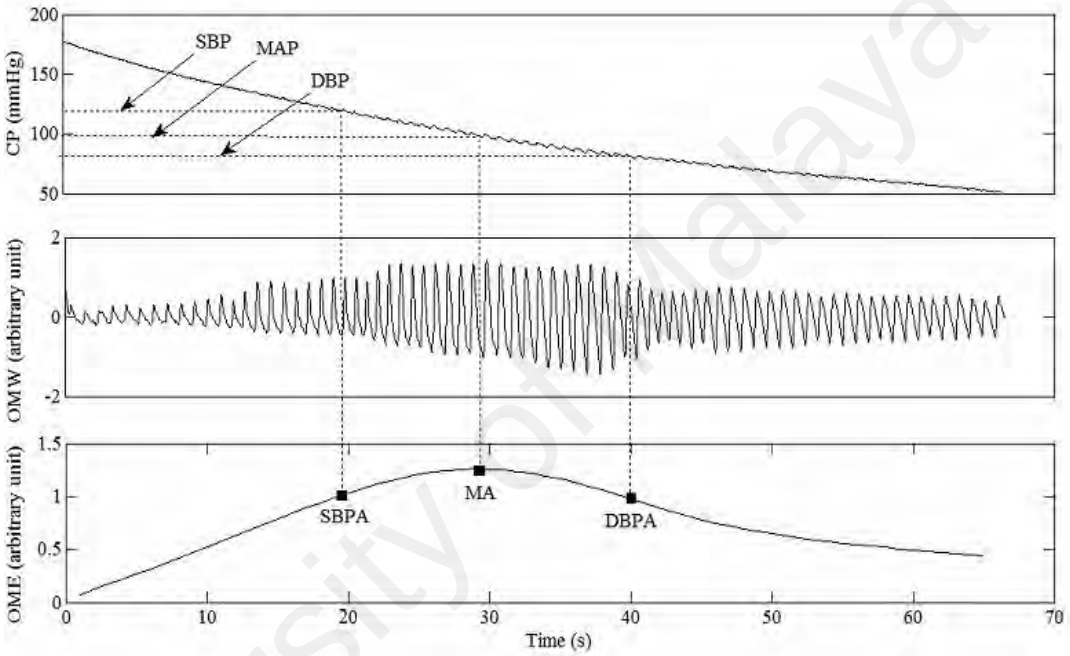

Figure 3.3: An example of the deflating cuff pressure (CP) waveform, pulsatile oscillometric waveform (OMW), and oscillometric waveform envelope (OMWE). MA: Amplitude of the OMWE corresponding to the location of the mean arterial pressure (MAP); SBPA: Amplitude of the OMWE corresponding to the location of the systolic blood pressure (SBP); DBPA: Amplitude of the OMWE corresponding to the location of the diastolic blood pressure (DBP).

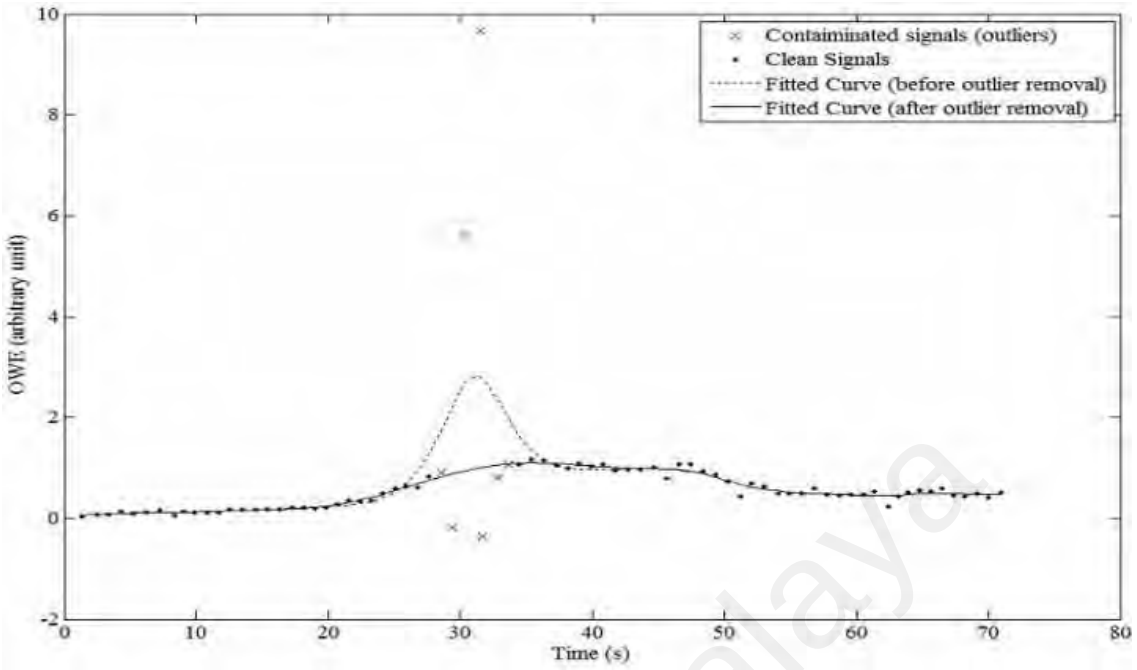

Figure 3.4: Cubic spline curve fitted to the oscillometric waveform envelope (OMWE) before and after removal of outlier pulses.

3.3.3 Detection and Removal of Outlier Points

A cubic spline curve was used to fit the OMWE (S. Lee, Jeon, et al., 2013). In order to increase the accuracy of the SBP and DBP estimation, data points contaminated with motion artifact were treated as outliers and removed during the OMWE curve fitting process. First, an automatic algorithm was used to detect these outlier points based on the sudden increase of cuff pressure during deflation and the oscillometric pulses relative to their respective neighbouring pulses. The peak, peak-to-peak, peak-to-bottom andbottom points of every oscillometric pulses were investigated. To be considered as clean data pulses, the absolute variations of the heights should not be more than 0.4 arbitrary unit and the height of each of these points should lie within ±50% of their respective neighbour pulses based on modification of (Antonova, 2013). Furthermore, a suddenly increasing pressure during cuff deflation were also considered as artifact. Figure 3.4 illustrates how outliers were removed on the fitted curve for the OMWE.

3.3.4 Feature Extraction

In this study, a total of 10 features were extracted from the OMWE, as illustrated in Figure 3.5 and defined in Table 3.1, of which six have been used in a previous study (S. Lee, Chang, et al., 2013), whereas the remaining features were newly proposed in this study. These features can be classified into five different classes: (I) Amplitude; (II) Duration; (III) Area; (IV) Ratio; and (V) MAP estimated using the MAA approach.

Table 3.1: Features extracted from the OMWE. The * symbol in the "References" column refers to features proposed in this study.

Feature	Description/ Equation	References
Amp_1	Maximum amplitude of OMWE	(S. Lee, Chang, et al., 2013)
Dur_1	Duration for maximum amplitude (MA) to occur	(S. Lee, Chang, et al., 2013)
Dur_2	Duration of OMWE	(S. Lee, Chang, et al., 2013)
$Area_1$	Area under OMWE	(S. Lee, Chang, et al., 2013)
$Area_2$	Area under OMWE before the MA's position	*
$Area_3$	Area under OMWE after the MA's position	*
$Ratio_1$	Duration for maximum amplitude to occur/Duration of OMWE	(S. Lee, Chang, et al., 2013)
$Ratio_2$	Area under OMWE before the MA's position /Area under OMWE	*
$Ratio_3$	Area under OMWE after the MA's position /Area under the OMWE	*
MAP	MAP estimated using the MAA algorithm	(S. Lee, Chang, et al., 2013)

Features from the amplitude class have been previously proposed by Lee et al. (S. Lee, Chang, et al., 2013). Amp_1 was motivated by the theoretical analysis findings by Baker which demonstrates the dependence of MAA estimates on the arterial mechanical properties, BP pulse shape and BP pressure (P. Baker, Westenskow, & Kück, 1997). The second class of features was derived based on duration. Dur_1 and Dur_2 were motivated by their other study (S. Lee, M. Bolic, et al., 2011), which demonstrated an improvement in the SBP and DBP estimates using the new relationships between the mean cuff pressure and the pseudo-envelopes that relate the duration of the MA's position and OMWE. The

third class of features was derived based on area measurements. The area under OMWE ($Area_1$) was proposed by Lee et al. (S. Lee, Chang, et al., 2013) based on Baker et al.'s (P. Baker et al., 1997) findings. However, SBP was only affected by OMWE before the MAP while DBP was affected by OMWE after the MAP. This led us to propose two other relevant features, i.e., the area before ($Area_2$) and after ($Area_3$) the MA's position. The third class of features were derived based on the morphology of the OMWE, which demonstrated the dependence of the SBP and DBP estimates on the shape of the OMWE (P. Baker et al., 1997). The ratio between the duration of the MA's position to duration of OMWE ($Ratio_1$) was proposed by Lee et al. (S. Lee, Chang, et al., 2013), while two other features were newly proposed in the present study based on the modification of Ratio1. Instead of relying on the position of the MA, $Ratio_2$ and Ratio3 also took into consideration the height of the OMWE curve by relating the area under the OMWE before and after the MA's position to the area under the OMWE. The last feature, i.e., MAP, has also been previously proposed by Lee et al. (S. Lee, Chang, et al., 2013) based on Moraes' findings (J. C. T. d. B. Moraes, Cerulli, & Ng, 2000) which indicated a close correlation between SBPR and DBPR with the MAP values.

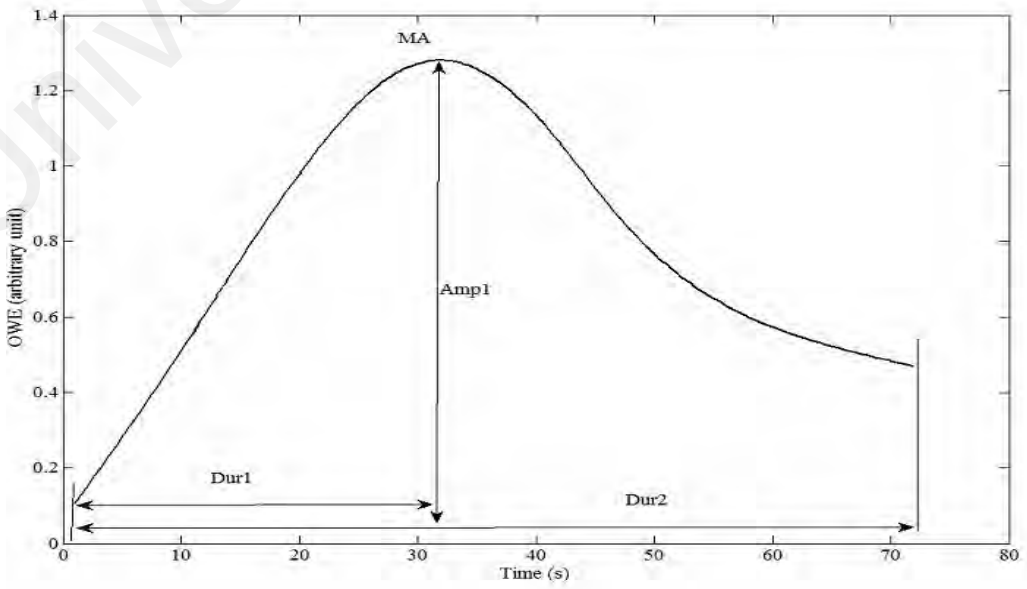

Figure 3.5: Description of features extracted from the OWE.

3.3.5 Blood Pressure Estimation Models

Three different BP estimation models were evaluated in the present study, including the conventional Maximum Amplitude Algorithm (MAA) method based on fixed characteristic ratios, and two newly proposed models using multiple linear regression (MLR) and support vector regression (SVR).

3.3.5.1 Maximum Amplitude Algorithm (MAA)

The conventional MAA method based on a fixed characteristic ratio were used to determine SBP and DBP. The fixed SBPR and DBPR were obtained as averages of the SBPR and DBPR derived from our Reference Scoring (RS).

3.3.5.2 Multiple Linear Regression (MLR) Model

MLR was used to model the relationship between the SBPR and DBPR with the features extracted from the OMWE. The model is defined as follows:

$$y = b_0 + b_1x_1 + b_2x_2 + \cdots + b_nx_n + \varepsilon \tag{3.3}$$

where y denotes either SBPR or DBPR, x_n denotes the n^{th} input feature, b_n denotes the n^{th} multiple regression coefficient, while ε is a sequence of unknown errors. Depending on the number of measurements, denoted by p, a matrix form containing information from each measurement is defined as follows (S. Lee, Lim, & Chang, 2014):

$$Y = X\beta + E \tag{3.4}$$

$$\mathrm{Y} = \begin{pmatrix} y_1 \\ y_2 \\ \cdot \\ \cdot \\ \cdot \\ y_p \end{pmatrix} \quad \mathrm{X} = \begin{pmatrix} x_{11} & Xx_{1p} \\ x_{21} & Xx_{2p} \\ \cdot & \cdot \\ \cdot & \cdot \\ \cdot & \cdot \\ x_{n1} & x_{np} \end{pmatrix} \quad \beta = \begin{pmatrix} b_1 \\ b_2 \\ \cdot \\ \cdot \\ \cdot \\ b_p \end{pmatrix} \quad \mathrm{E} = \begin{pmatrix} \varepsilon_1 \\ \varepsilon_2 \\ \cdot \\ \cdot \\ \cdot \\ \varepsilon_p \end{pmatrix} \tag{3.5}$$

The multiple regression coefficients, β, can then be obtained based on the minimum sum of squared errors by solving Eq. 3.7:

$$y = b_0 + b_1 x_1 + b_2 x_2 + \cdots + b_n x_n + \varepsilon \tag{3.6}$$

$$\beta = (\mathrm{X^T X})^{-1} \mathrm{X^T Y} \tag{3.7}$$

3.3.5.3 Linear ν-Support Vector Regression (ν-SVR) model

Consider a set of training points, $\{(x1, y1), \ldots, (xl, yl)\}$, where $x_i \in R_n$ is a feature vector while $y_i \in R_n$ is the target output. The ν- SVR model searches for the best approximation of the actual output y_i (i.e., SBPR and DBPR in the present study) based on the input features, xi, with an acceptable error tolerance of ε. Let x_i be mapped into a feature space by a nonlinear function (x_i); the decision function becomes:

$$y = f(w, b) = \langle w.x \rangle + b \tag{3.8}$$

where *w* and *b* are parameters vectors of the SVR model. The parameter w vector determines the flatness of the approximation function, with lower w values giving smoother and less complicated approximation function (Basak, Pal, & Patranabis, 2007; Yu, Chen, & Chang, 2006). The mapping function $\varphi(x_i)$ transforms the data into a higher dimensional feature space to make it possible to perform the linear separation. Parameter $\nu \in (0,1]$ is used to control the number of support vectors and training errors. The regression problem was formulated as the following convex optimization problem:

$$\underset{w, b, \xi_i, \xi_i^*, \varepsilon}{Minimize} \quad \frac{1}{2}|w^T w| + C(\nu\varepsilon + \frac{1}{n}\sum_{i=1}^{i=n}(\xi_i + \xi_i^*)) \tag{3.9}$$

$$Subject\ to \quad \begin{Bmatrix} (w^T\varphi(x_i) + b) - y_i \leq \varepsilon + \xi_i \\ y_i - (w^T\varphi(x_i) + b) \leq \varepsilon + \xi_i^* \\ \xi_i, \xi_i^* \geq 0, i = 1,2,\dots,n \end{Bmatrix} \tag{3.10}$$

ξ_i and ξ^* specify the upper and lower training errors subjected to the error tolerance, ε, while C is a positive constant which determines the trade-off between the flatness and the amount up to which deviations larger than ε are tolerated (Smola & Schölkopf, 2004; Yu et al., 2006). In this study, the LIBSVM, a Matlab library for SVM (Chang & Lin, 2011) is used to generate the proposed features based regression model for the SVR algorithm. The linear function is employed as a SVR mapping function with parameter C = 14.49 and v = -1.89 for both SBP and DBP models. These two parameters were selected with dynamic range from −20 to 20 and −20 to 0 for C and v respectively. The parameter b was 0.9865 and 0.6554 for SBP and DBP models respectively.

3.3.6 Evaluation of Results

In the present study, two standard protocols commonly used for the evaluation of the accuracy of BP estimation, i.e., the British Hypertension Society (BHS) and the American Association for the Advancement of Medical Instrumentation (AAMI), were applied. BHS evaluates the performance of the BP estimation based on the cumulative percentage of readings which fall within absolute differences of 5, 10 and 15 mmHg from the mercury standard. The mercury standard refers to the SBP and DBP values obtained by a trained person using the auscultatory method (i.e., using a stethoscope to listen to the Korotkoff sounds and a mercury sphygmomanometer to measure the pressure level in the cuff). To fulfil the BHS protocol, the tested device must achieve at least grade B, i.e., 50% of readings falling within 5 mmHg, 75% within 10 mmHg, and 90% within 15 mmHg of the readings obtained from the gold standard (GS) method, as illustrated in Table 3.2.

On the other hand, to satisfy the AAMI standard, the mean difference between the measurements obtained from the tested device and from the GS method should lie within

±5 mmHg (O'Brien et al., 1993)). The upper limit on the standard deviation (SD) depends on the level of the mean difference, as listed in Table 3.3 (O'Brien et al., 1993).

Table 3.2: Grading criteria according to the British Hypertension Society (BHS) protocol. Grades are derived based on the cumulative percentages of readings which fall within absolute differences of 5, 10 and 15 mmHg from the mercury standard. To achieve a particular grade, all three percentages must be equal to or greater than the tabulated values (Association for the Advancement of Medical Instrumentation: Arlington, 2003).

Grade	≤mmHg	≤10 mmHg	≤15 mmHg
	Cumulative percentage of reading (%)		
A	60	85	95
B	50	75	90
C	40	65	85
D	Worse than C		

Table 3.3: Upper limit on the standard deviation of paired differences for given values of the mean of the paired differences (adapted from (O'Brien et al., 1993)).

Mean difference (mmHg)	Standard Deviation (mmHg)
0	6.95 or less
±0.5	6.93 or less
±1.0	6.87 or less
±1.5	6.78 or less
±2.0	6.65 or less
±2.5	6.47 or less
±3.0	6.25 or less
±3.5	5.97 or less
±4.0	5.64 or less
±4.5	5.24 or less
±5.0	4.81 or less

3.3.7 Analyses

Two analyses were performed. In the first, we attempted to determine the effect of noise detection (outlier removal) on SBP and DBP estimation errors. In the second, we sought to establish the SBP and DBP estimation performance using conventional MAA, MLR and SVR models. The performance of the individual features were evaluated, followed by identification of the best combination of features for the two different types of BP estimation models. We performed a comprehensive study on the performance of all possible combinations of two features on the BP estimation methods, resulting in a total of 55 combinations. To search for the best combination of more than two indices, we

applied SFFS starting from the best combination of two features provided by the exhaustive search. Our results revealed that adding a third feature did not provide an improvement in the results. A four-fold cross validation was applied during the implementation of all the BP estimation methods.

3.4 Results

3.4.1 Parameter tuning of *C* and v value for SVR

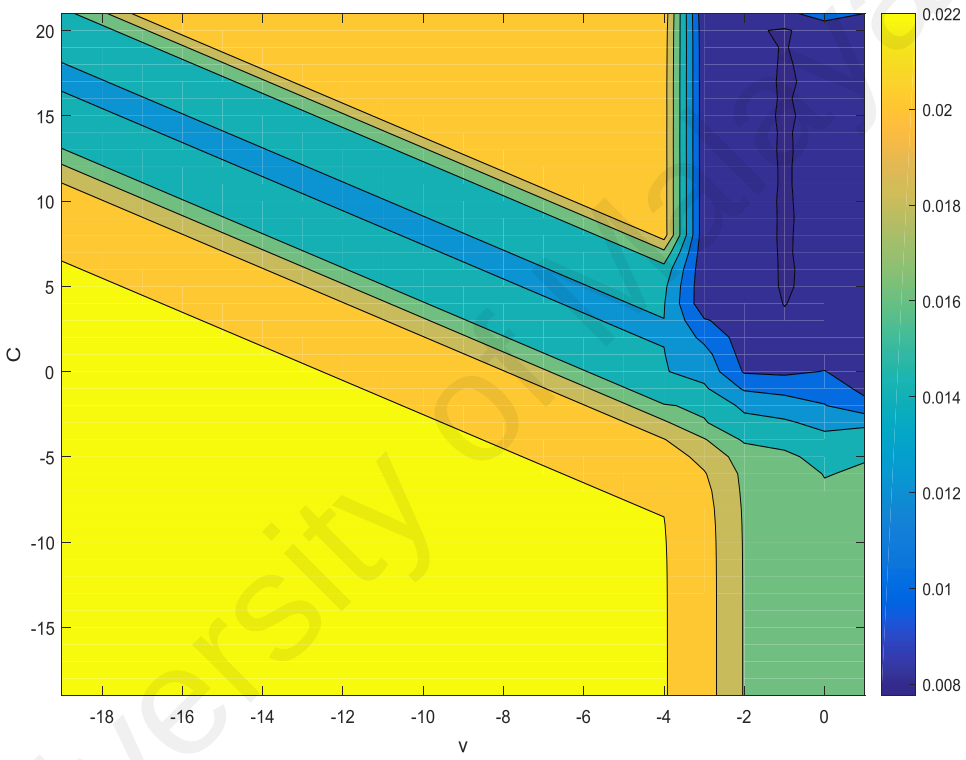

Figure 3.6: Response surface plot of the error with respect to c and v with step size of 1 using the training data. Color bar on the right indicates the error scale. A *C* and v yielded the lower error of 0.078.

As shown in Figure 3.6, all possible combinations of *C* and *v* were varied with a step size of 1 (*C* from -20 to 20 and *v* from -20 to 0). Region of *C* within 10 - 15, and region of *v* within -3 - 0 yielded the lowest error. Parameter search range was then focused on these regions, with a refined step size of 0.25 to further narrow down the range with the lowest error. The above procedure was repeated with refined step sizes of 0.05 and 0.01. Using this search method, the best parameters for *C* and *v* were 14.49 and -1.89, respectively, which yielded a minimum error of 0.076.

3.4.2 Systolic and Diastolic Blood Pressure Estimation Performance Using Conventional MAA, MLR and SVR Models

Conventional MAA method estimated the SBP and DBP using fixed characteristic ratio from maximum amplitude located on OMWE. Therefore, comparison among features extracted from the OMWE envelope was omitted for MAA. Tables 3.4 and 3.5 showed the performance of each of the ten features extracted from the OMWE in SBP and DBP estimation using the MLR and SVR models respectively. With regards to SBP, most features achieved a Grade B performance with both models according to the BHS standard, except for $Area_3$ which obtained a Grade C performance using the MLR model. Individually, MAP as well as $Ratio_2$ and $Ratio_3$ derived based on the morphology of the OMWE outperformed other features using both MLR and SVR models, as they provided lower mean and SD of differences between RS and estimated SBP values. In terms of DBP, most features achieved a Grade A performance according to the BHS protocol, except for Dur_2 (Grade B using both MLR and SVR models), Dur_1 and $Ratio_3$ (both achieving Grade B with the SVR model). Based on the AAMI standard, comparable performances were observed among all ten features using both MLR and SVM models, with most features passing the AAMI standard marginally. Using the SFFS approach, we identified $Ratio_2$ and $Area_3$ to be the best combination of two features.

Table 3.4: Comparison among features extracted from the OWE envelope in BP estimation performance using the MLR model.

Feature		Grade	Cumulative percentage of reading (%)			Mean ± SD (mmHg)	Mean ± SD of differences (mmHg)
			≤5	≤10	≤15		
Amp_1	SBP	B	53	84	93	105±17	-1.2±14.2
	DBP	A	70	92	95	63±9	0.5±6.1
Dur_1	SBP	B	58	86	95	105±13	-0.7±10.6
	DBP	A	69	89	95	63±10	0.6±6.6
Dur_2	SBP	B	54	79	91	105±16	-1.1±14.3
	DBP	B	63	87	94	63±9	0.4±6.8
$Area_1$	SBP	B	50	84	93	105±17	-1.3±14
	DBP	A	70	89	95	63±9	0.2±6.2

Table 3.5 continued: Comparison among features extracted from the OWE envelope in BP estimation performance using the MLR model.

$Area_2$	SBP	B	61	86	94	105±15	-0.4±10.2
	DBP	A	71	92	95	63±9	0.4±6.2
$Area_3$	SBP	C	50	79	86	104±18	-1.9±16.9
	DBP	A	73	89	95	63±9	0.1±6.3
$Ratio_1$	SBP	B	55	80	93	106±10	0.1±8.0
	DBP	A	73	89	95	63±9	0.3±6.5
$Ratio_2$	SBP	B	55	85	96	106±10	0.5±7.0
	DBP	A	68	89	96	63±9	0.1±6.6
$Ratio_3$	SBP	B	55	85	96	106±10	0.5±7.0
	DBP	A	68	89	96	63±9	0.1±6.6
MAP	SBP	B	55	89	98	106±10	0.3±6.6
	DBP	A	71	89	95	63±9	0.1±6.6

SBP, systolic blood pressure (range: 70 – 133 mmHg); DBP, diastolic blood pressure (range: 42 – 88 mmHg).

Table 3.6: Comparison among features extracted from the OWE envelope in BP estimation performance using the SVR model.

Feature		Grade	Cumulative percentage of reading (%)			Mean ± SD (mmHg)	Mean ± SD of differences (mmHg)
			≤5	≤10	≤15		
Amp_1	SBP	B	60	86	94	105±18	-1.2±15.4
	DBP	A	70	93	95	63±9	0.4±6.4
Dur_1	SBP	B	60	88	94	104±13	-1.7±9.7
	DBP	B	65	89	94	64±9	0.8±6.4
Dur_2	SBP	B	55	83	91	104±15	-1.8±13
	DBP	B	69	89	94	63±9	0.7±6.6
$Area_1$	SBP	B	58	87	93	104±16	-1.5±15
	DBP	A	70	90	95	63±9	0.2±6.2
$Area_2$	SBP	B	64	89	94	106±14	-0.1±9
	DBP	A	69	89	96	63±9	-0.2±6.4
$Area_3$	SBP	B	53	81	91	104±16	-1.5±14
	DBP	A	70	91	95	63±9	0.6±6.5
$Ratio_1$	SBP	B	58	84	94	106±10	0.3±7.6
	DBP	A	68	89	95	64±9	1.0±6.6
$Ratio_2$	SBP	B	59	89	98	107±10	1.0±6.3
	DBP	A	70	90	95	63±9	0.6±6.6
$Ratio_3$	SBP	B	58	88	98	107±11	1.1±6.4
	DBP	B	58	85	95	64±9	1.4±7.2
MAP	SBP	B	58	85	95	106±10	0.2±6.8
	DBP	A	70	89	95	63±9	0.5±6.7

SBSBP, systolic blood pressure (range: 70 – 133 mmHg); DBP, diastolic blood pressure (range: 42 – 88 mmHg).

Table 3.7: Comparison among conventional MAA method, MLR and SVR models in blood pressure (SBP and DBP) estimation performance using the best combination of features ($Ratio_2$ and $Area_3$)

	Grade	Cumulative percentage of reading (%)			Mean ± SD (mmHg)	Mean ± SD of differences (mmHg)
	Absolute difference with RS	≤5	≤10	≤15		
Conventional MAA method (using fixed characteristic ratio)						
SBP	B	55	84	90	107 ± 13	-1.6 ± 8.6
DBP	A	70	89	95	62 ± 9	0.3 ± 6.7
MLR model (using the best combination of features)						
SBP	A	63	91	98	106 ± 11	-0.3 ± 5.8
DBP	A	71	89	95	63 ± 9	-0.2 ± 6.4
SVR model (using the best combination of features)						
SBP	A	66	94	98	107 ± 12	-0.6 ± 5.4
DBP	A	68	90	95	62 ± 9	0.4 ± 6.3
Method comparison (Differences between MLR and SVR)						
SBP	A	98	100	100		-0.3 ± 1.6
DBP	A	100	100	100		0.6 ± 1.0

SBP, systolic blood pressure (range: 70 – 133 mmHg); DBP, diastolic blood pressure (range: 42 – 88 mmHg).

As compared to the conventional MAA method using a fixed characteristic ratio (Table 3.6), the variable characteristic ratio method using both MLR and SVR models applied on the best combination of features significantly reduced the mean and SD of differences between the estimated SBP and that obtained from RS. Meanwhile, only a slight reduction in SD was observed for DBP as compared to the conventional MAA. Based on the BHS standard, both MLR and SVR models, as well as the conventional MAA method could achieve a Grade A performance for SBP estimation. Generally, comparable performance was obtained for both MLR and SVR models, with up to 98% (95%) of data lying within ±15 mmHg from RS for SBP (DBP) estimation. The difference in the performance between the MLR and the SVR models was not statistically different (p-value > 0.05). In addition, both model satisfied the performance criteria set by the AAMI standard, with SVR model achieving a slightly lower SD of difference with RS but at a slightly higher mean difference value.

As illustrated in Figures 3.8 and 3.9, their estimated values for SBP (DBP) data used in the present study were very similar. Figure 3.10 shows the difference of SBP and DBP estimated between MLR and SVR, all the values lied within the range of ±5 mmHg (with the exceptions of only 2 values for SBP). At higher SBP values, SVR model appeared to

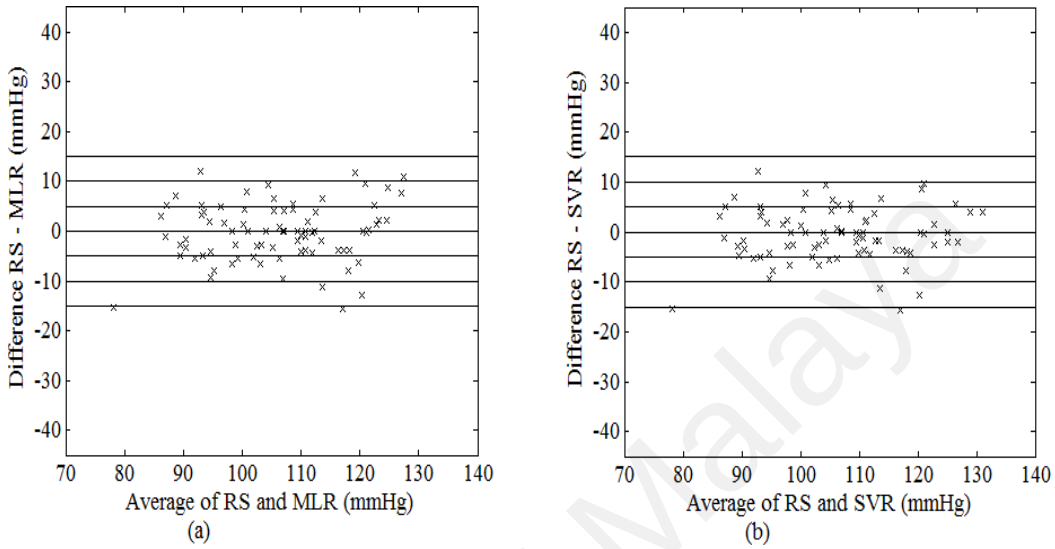

provide larger values as compared to that estimated using the MLR model while an opposite trend was observed in the middle range of SBP.

Figure 3.7: Bland–Altman plot of possible SBP between RS and (a) MLR model; (b) SVR model using the best combination of features.

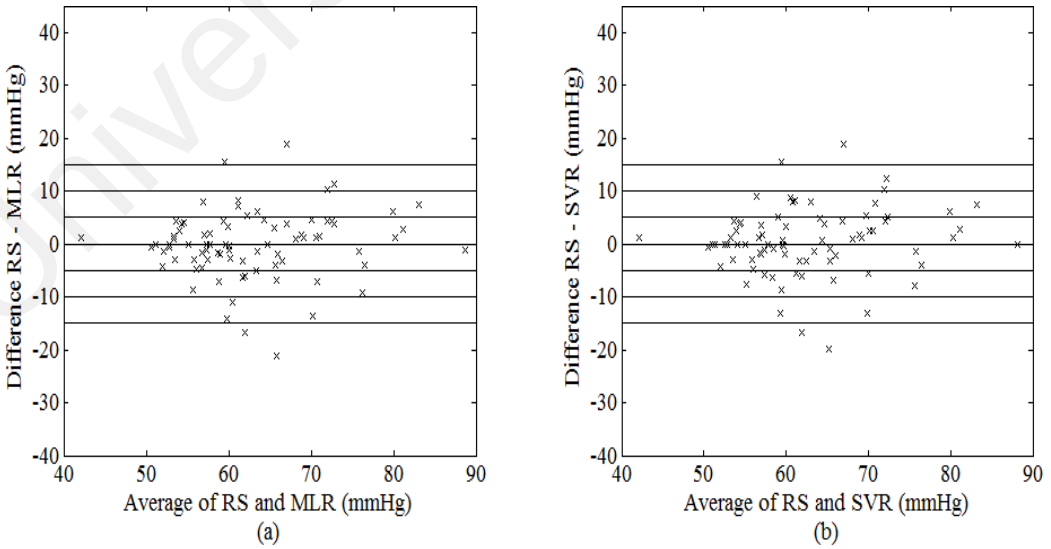

Figure 3.8: Bland–Altman plot of possible DBP between RS and (a) MLR model; (b) SVR model using the best combination of features

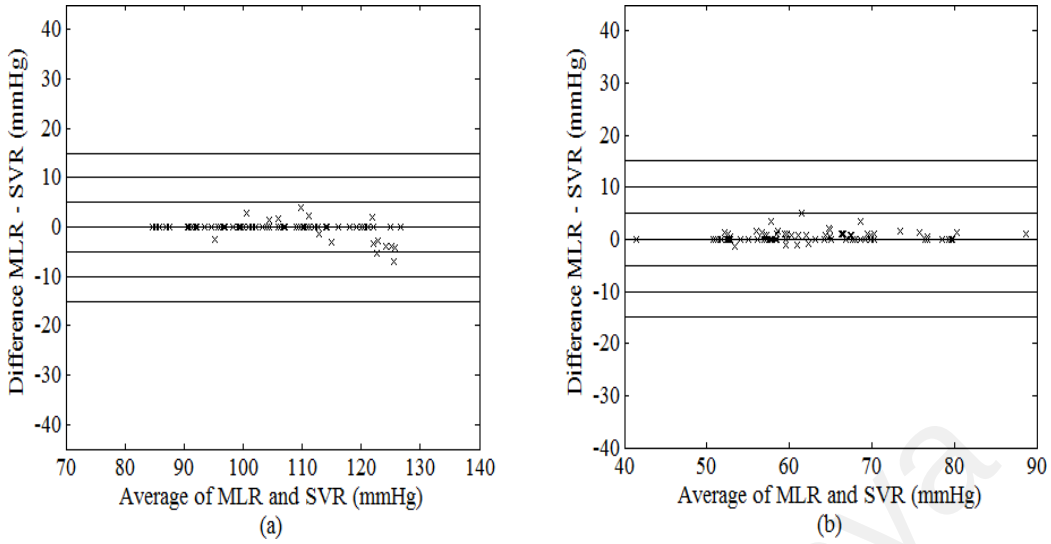

Figure 3.9: Bland–Altman plot of possible (a) SBP and (b) DBP between MLR and SVR models using the best combination of features.

3.4.3 Effect of Noise Detection (Outlier Removal) on Systolic and Diastolic Blood Pressure Estimation Errors

Figures 3.11 and 3.12 are the Bland-Altman plots demonstrating the performance of estimated SBP and DBP using the conventional MAA algorithm, with and without using the outlier removal algorithm before the OMWE curve fitting process. On the other hand, cumulative percentage of BP readings which fall within absolute differences of 5, 10 and 15 mmHg from RS (required for evaluation using the BHS standard) as well as mean ± SD difference between RS and conventional MAA algorithm (required for evaluation using the AAMI standard) were presented in Table 3.4. Based on the Bland– Altman plots for SBP (illustrated in Figure 3.6), the errors between the estimated pressure and the RS were large without outlier removal (up to 125 mmHg at low SBP), and substantially reduced upon elimination of the outlier points, with most data points lying within ±20 mmHg errors from the RS. Similar observations were found for the DBP (Figure 3.7).

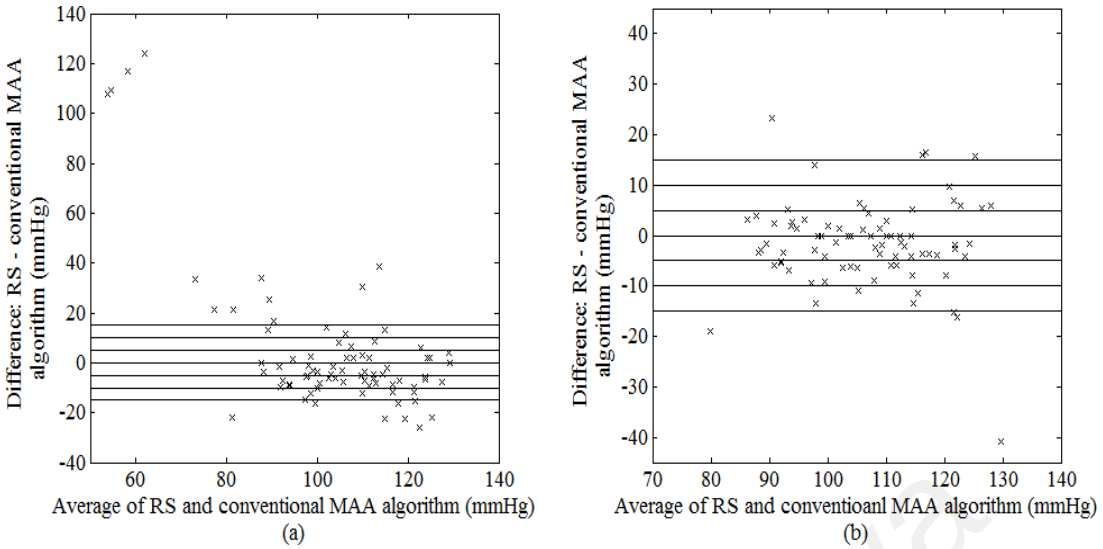

Figure 3.10: Bland–Altman plot of possible SBP between RS and conventional MAA algorithm (a) before and (b) after outlier removal.

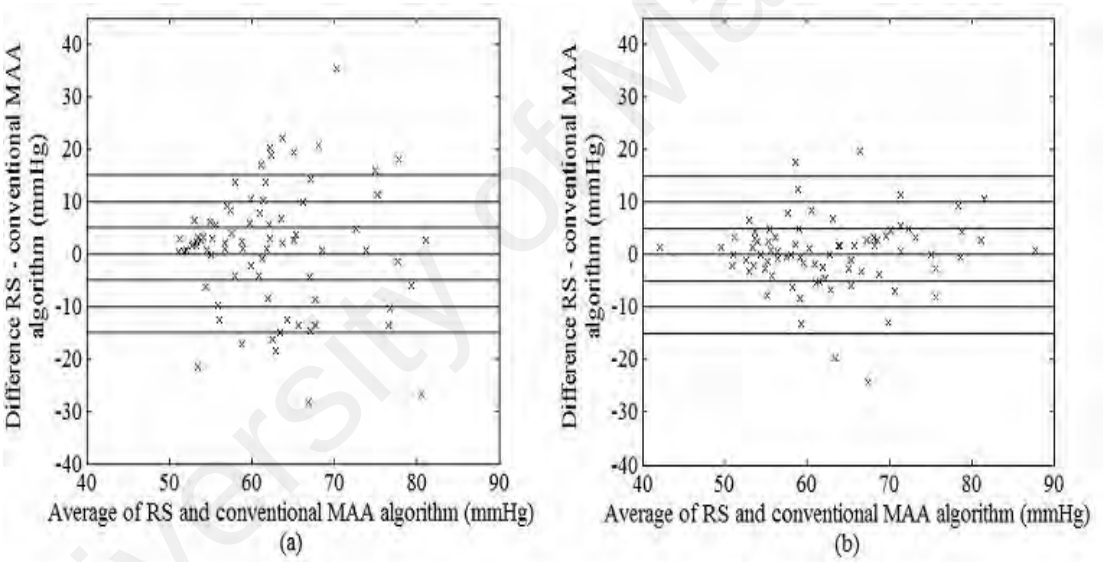

Figure 3.11: Bland–Altman plot of possible DBP between RS and conventional MAA algorithm (a) before and (b) after outlier removal.

As shown in Table 3.7, the outlier removal method proposed in this study significantly improved the accuracy of the estimated pressures, with an improvement in BHS grades from D to B and A for SBP and DBP respectively. With regards to the AAMI standard, although a significant improvement was found in both mean and SD difference for SBP after outlier removal, the conventional MAA method failed to satisfy the AAMI standard (with a mean ± SD of −1.6 ± 8.6 mmHg, refer to Table 3.4). In terms of DBP, the mean ± SD difference improved from 0 ± 14.2 mmHg to 0.3 ± 6.7 mmHg upon outlier removal,

which satisfied the passing criteria for the AAMI standard.

Table 3.8: Cumulative percentage of readings which fall within absolute differences of 5, 10 and 15 mmHg from RS using the conventional MAA algorithm with the respective BHS grades, as well as mean±SD and mean±SD difference between RS and conventional MAA algorithm for BP estimation before and after outlier removal.

Grade		Cumulative percentage of reading (%)			Mean ± SD (mmHg)	Mean ± SD of differences (mmHg)
	Absolute difference: RS – MAA	≤5	≤10	≤15		
Before outlier removal						
SBP	D	30	61	74	101 ± 29	4.5 ± 28.6
DBP	D	43	61	79	63 ± 12	0.0 ± 14.2
After outlier removal						
SBP	B	55	84	90	107 ± 13	-1.6 ± 8.6
DBP	A	70	89	95	62 ± 9	0.3 ± 6.7

SBP, systolic blood pressure (range: 70 – 133 mmHg); DBP, diastolic blood pressure (range: 42 – 88 mmHg).

Figures 3.13 and 3.14 are the Bland-Altman plots demonstrating the performance of estimated SBP and DBP using the MLR algorithm, with and without using the outlier removal algorithm before the OMWE curve fitting process using the best combination of features ($Ratio_2$ and $Area_3$) acquired in section 3.4.2.

On the other hand, cumulative percentage of BP readings which fall within absolute differences of 5, 10 and 15 mmHg from RS (required for evaluation using the BHS standard) as well as mean ± SD difference between RS and conventional MAA algorithm (required for evaluation using the AAMI standard) were presented in Table 3.4. Based on the Bland– Altman plots for SBP (illustrated in Figure 3.6), the errors between the estimated pressure and the RS were large without outlier removal (up to 47 mmHg at DBP), and substantially reduced upon elimination of the outlier points, with most data points lying within ±20 mmHg errors from the RS. Similar observations were found for the DBP (Figure 3.7).

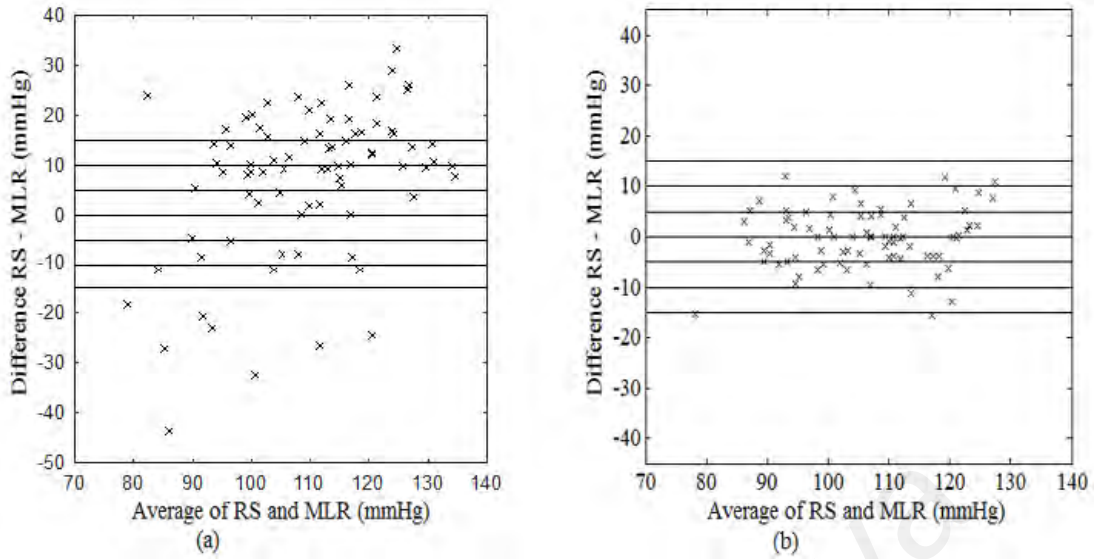

Figure 3.12: Bland–Altman plot of possible SBP between RS and MLR algorithm (a) before and (b) after outlier removal.

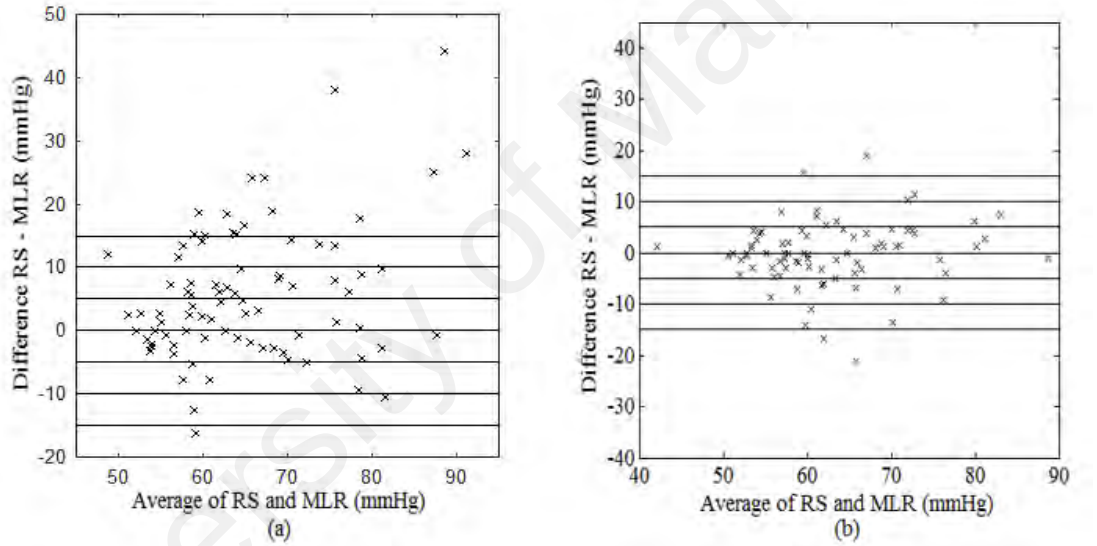

Figure 3.13: Bland–Altman plot of possible DBP between RS and MLR algorithm (a) before and (b) after outlier removal.

As shown in Table 3.8, the outlier removal method proposed in this study significantly improved the accuracy of the estimated pressures, with an improvement in BHS grades from D to A and A for SBP and DBP respectively. With regards to the AAMI standard, although a significant improvement was found in both mean and SD difference for SBP after outlier removal. In terms of SBP, the mean ± SD difference improved from 14.2 ± 8.3 mmHg to -0.3 ± 5.8 mmHg upon outlier removal. For DBP, the mean ± SD difference improved from 8.6 ± 8.4 mmHg to -0.2 ± 6.4 mmHg upon outlier removal. Both SBP and DBP satisfied the passing criteria for the AAMI standard.

Table 3.9: Cumulative percentage of readings which fall within absolute differences of 5, 10 and 15 mmHg from RS using the MLR algorithm with the respective BHS grades, as well as mean±SD and mean±SD difference between RS and MLR algorithm for BP estimation before and after outlier removal.

	Grade	Cumulative percentage of reading (%)			Mean ± SD (mmHg)	Mean ± SD of differences (mmHg)
	Absolute difference with RS	≤5	≤10	≤15		
Before outlier removal						
SBP	D	9	30	49	112 ±17	14.2 ± 8.3
DBP	D	38	58	67	68 ± 13	8.6 ± 8.4
After outlier removal						
SBP	A	63	91	98	106 ± 11	-0.3 ± 5.8
DBP	A	71	89	95	63 ± 9	-0.2 ± 6.4

SBP, systolic blood pressure (range: 70 – 133 mmHg); DBP, diastolic blood pressure (range: 42 – 88 mmHg).

Figures 3.15 and 3.16 are the Bland-Altman plots demonstrating the performance of estimated SBP and DBP using the SVR algorithm, with and without using the outlier removal algorithm before the OMWE curve fitting process using the best combination of features ($Ratio_2$ and $Area_3$) acquired in section 3.4.2.

On the other hand, cumulative percentage of BP readings which fall within absolute differences of 5, 10 and 15 mmHg from RS (required for evaluation using the BHS standard) as well as mean ± SD difference between RS and conventional MAA algorithm (required for evaluation using the AAMI standard) were presented in Table 3.9. Based on the Bland– Altman plots for SBP (illustrated in Figure 3156), the errors between the estimated pressure and the RS were large without outlier removal (up to 37 mmHg at DBP), and substantially reduced upon elimination of the outlier points, with most data points lying within ±20 mmHg errors from the RS. Similar observations were found for the DBP (Figure 3.16).

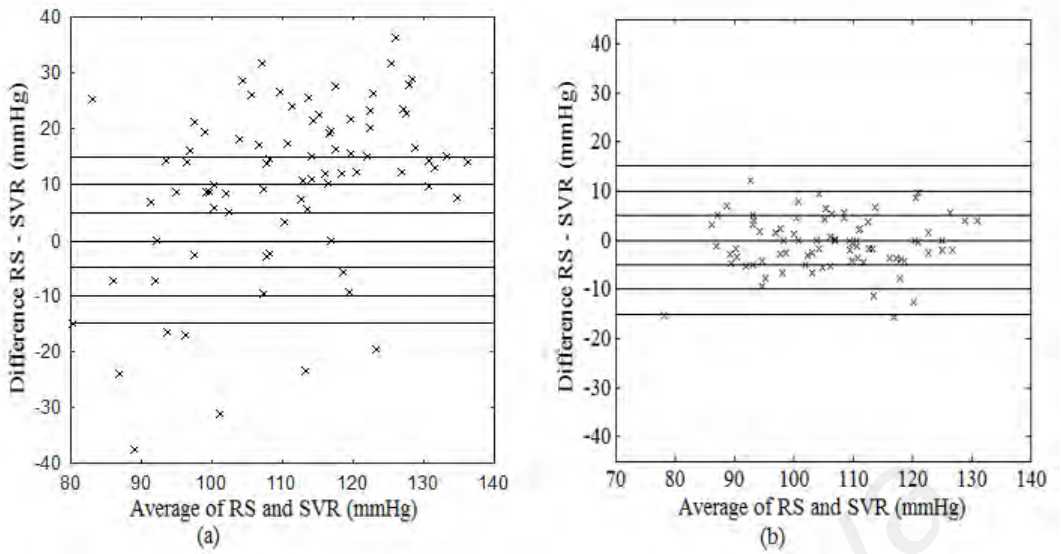

Figure 3.14: Bland–Altman plot of possible SBP between RS and SVR algorithm (a) before and (b) after outlier removal.

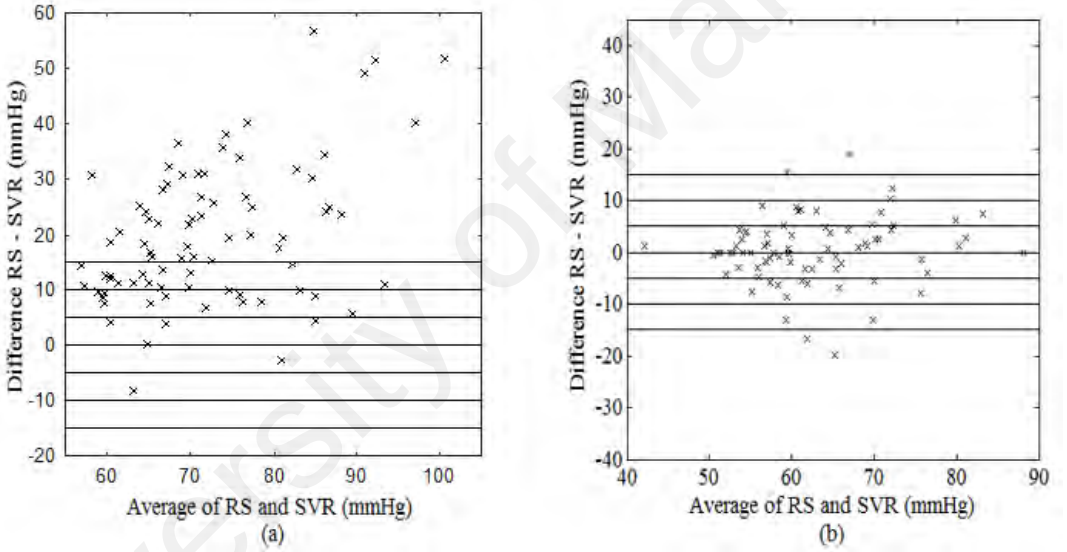

Figure 3.15: Bland–Altman plot of possible DBP between RS and SVR algorithm (a) before and (b) after outlier removal.

As shown in Table 3.9, the outlier removal method proposed in this study significantly improved the accuracy of the estimated pressures, with an improvement in BHS grades from D to A and A for SBP and DBP respectively. With regards to the AAMI standard, although a significant improvement was found in both mean and SD difference for SBP after outlier removal. In terms of SBP, the mean ± SD difference improved from 15.8 ± 8.7 mmHg to -0.6 ± 5.4 mmHg upon outlier removal. For DBP, the mean ± SD difference improved from 8.4 ± 8.1 mmHg to 0.4 ± 6.3 mmHg upon outlier removal. Both SBP and DBP satisfied the passing criteria for the AAMI standard.

Table 3.10: Cumulative percentage of readings which fall within absolute differences of 5, 10 and 15 mmHg from RS using the conventional MAA algorithm with the respective BHS grades, as well as mean±SD and mean±SD difference between RS and conventional MAA algorithm for BP estimation before and after outlier removal.

	Grade	Cumulative percentage of reading (%)			Mean ± SD (mmHg)	Mean ± SD of differences (mmHg)
	Absolute difference: RS – MAA	≤5	≤10	≤15		
Before outlier removal						
SBP	D	7	25	40	115 ± 18	15.8 ± 8.7
DBP	D	38	58	69	67 ± 12	8.4 ± 8.1
After outlier removal						
SBP	A	66	94	98	107 ± 12	-0.6 ± 5.4
DBP	A	68	90	95	62 ± 9	0.4 ± 6.3

SBP, systolic blood pressure (range: 70 – 133 mmHg); DBP, diastolic blood pressure (range: 42 – 88 mmHg).

3.5 Discussion

Accurate oscillometric BP estimation in an unsupervised environment is challenging in the presence of interference, notably movement artifact which interrupts the air flow in the deflating cuff. While several studies have attempted to detect noise in the BP signals using additional sensing devices such as acceleration and capacitive sensors (Choi, Park, & Lee, 2007) , as well as morphological comparison with good-quality reference pulses (Charbonnier, Siche, & Vancura, 2000) , none of these studies have investigated the effect of the detected noise on the extraction of accurate BP values from the contaminated signals. In the present study, we integrated an artifact removal block (Figure 3.1) in our SBP and DBP estimation algorithm which was based solely on the oscillometric signal without using additional sensors or reference signals. Our results demonstrated that the mean and standard deviation of the BP estimation errors between the MAA algorithm and the RS substantially decreased upon artifact removal (Figures 3.6 and 3.7, Table 3.4), which strongly advocates the importance of the artifact removal component proposed in the present study. Furthermore, the MAA algorithm has been well recognized to be susceptible to additive noise as it is derived based on the amplitude of the pulse (Mafi, Rajan, Bolic, Groza, & Dajani, 2011). The cubic spline interpolation method (Table 3.4-

before outlier removal), commonly used to smooth the envelope of the OMW for eliminating the erroneous peak values generated by artifact, was shown in this study to be ineffective in reducing the interference caused by movement artifact (S. Chen et al., 2010).

We further demonstrated from our analysis results (Tables 3.5 and 3.6) that the usage of variable characteristic ratio derived based on several features extracted from the OMWE improved the BP estimation accuracy over the conventional MAA method using fixed characteristic ratios (SBP: mean ± SD = −1.6 ± 8.6 mmHg; DBP: mean ± SD = 0.3 ± 6.7 mmHg). Due to the large uncertainties in the characteristic ratios reported in the literature (Barbé, Van Moer, & Lauwers, 2010; S. Lee, Jeon, et al., 2013; J. Liu et al., 2013), we used averages of the SBPR and DBPR ratios derived from our reference SBP and DBP measurements based on the clinical expert readings. When evaluated individually (Tables 3.5 and 3.6), the MAP feature proposed by Lee et al. (S. Lee, Chang, et al., 2013) as well as the two newly proposed features in the present study, i.e., $Ratio_2$ and $Ratio_3$, outperformed other features in providing accurate SBP estimates (MAP: mean ± SD = 0.3 ± 6.6 mmHg for MLR and 0.2 ± 6.8 mmHg for SVR; $Ratio_2$: mean ± SD = 0.5 ± 7.0 mmHg for MLR and 1.0 ± 6.3 mmHg for SVR; $Ratio_3$: mean ± SD = 0.5±7.0 mmHg for MLR and 1.1 ± 6.4 mmHg for SVR). The $Ratio_2$ and $Ratio_3$ features were derived based on the morphology of the OMWE, which has been reported to reflect the stiffness characteristics of the vessel (Babbs, 2012). Consistent with previously published findings, the degree of arterial stiffness and thus pulse pressure as well as the shape of the OWE has the largest influence on the SBP and DBP errors determined based on the conventional MAA method (J. Liu et al., 2013), leading to errors as high as 15%–20% (Ursino & Cristalli, 1996) or 58 mmHg (J. Liu et al., 2013). To the contrary, the $Ratio_1$ feature proposed by Lee et al. (S. Lee, Chang, et al., 2013), which also described the shape of the OMWE, was found to be inferior in our study as compared to $Ratio_2$ and $Ratio_3$. The main difference between these features were that while $Ratio_1$ was derived based on

length of the oscillometric waveform, $Ratio_2$ and $Ratio_3$ described asymmetry in the waveform based on area of the OMWE, thus took into consideration both amplitude and length of the waveform. Compared to length, measurements based on area of the OWE, e.g., $Ratio_2$ and $Ratio_3$ are more robust to noise interference as well as errors associated with difficulties in determining the starting and ending points of the cuff pressure oscillations. The Dur_2, Amp_1 and $Area_1$ features proposed by Lee et al. (S. Lee, Chang, et al., 2013) demonstrated poor performance in SBP estimates individually when applied on data set used in the present study.

Using the SFFS approach, we were able to achieve a significant reduction in the mean and standard deviation of differences between the estimated SBP values and the RS (MLR: mean ± SD = −0.3 ± 5.8 mmHg; SVR: mean ± SD = −0.6 ± 5.4 mmHg) with only two features, i.e., $Ratio_2$ and $Area_3$ (Table 3.7), as compared to the conventional MAA method (mean ± SD = −1.6 ± 8.6 mmHg). To the contrary, negligible improvement was achieved for DBP estimation. Our results were comparable with that reported by Lee et al. (S. Lee, Chang, et al., 2013), which utilized three features, i.e., $Area_1$, $Ratio_1$ and MAP selected based on t-test evaluation on their clean dataset. While t-test evaluates the significance of features independently (filter-based method), the SFFS method takes into account interaction among features (wrapper-based method). The advantages of wrapper-based methods include taking into account feature dependencies (Z. Zhu, Ong, & Dash, 2007), and they typically perform better in prediction accuracy when compared with filter-based methods (Z. Zhu et al., 2007).

Despite its simplicity, our results showed that the MLR model was able to achieve comparable performance with that obtained from the SVR model (Table 3.7, Figures 3.8– 3.10), which requires optimization of the model parameters through repeated training. The MLR model was able to estimate the best fitting surface of a suitable function that

relates the independent and dependent variables (Matthews, 2005). On the other hand, Gaussian mixture regression (S. Lee, Chang, et al., 2013) as well as Bayesian model (S. Lee, Jeon, et al., 2013), applied on a combination of five features, have also been recently proposed by Lee et al. (Forouzanfar et al., 2011) and evaluated on experimental data acquired from 85 healthy subjects. As compared to these methods, our MLR and SVR models do not need careful formulation of prior distributions of the data. In addition, the same research group has also presented a feature-based neural network approach for the estimation of BP (Forouzanfar et al., 2011), which used features extracted from the OMWE (consisting of the amplitudes, spreads, and centres of the modelled Gaussian functions) as inputs to the neural network. Although the proposed approach was shown to achieve lower values of mean and standard deviation of error in the estimations (SBP: mean ± SD = 6.76 ± 8.89 mmHg; DBP: mean ± SD = 5.98 ± 7.90 mmHg) as compared to the conventional MAA method, their results did not meet the AAMI standard. This was probably because their oscillometric measurements were taken at different time points with that acquired by the nurse, which served as RS. As suggested by Soueidan et al. (Soueidan et al., 2012), natural BP variability often exceeds the maximum allowable error set by the AAMI standard (i.e., ±5 mmHg), thus it is advisable to acquire simultaneous recordings of both oscillometric signal and RS for accurate comparison, as that performed in the present study.

Using a different approach based on a Fourier series representation of the oscillometric waveform, Barbe et al. (Barbe et al., 2011) introduced a Hammerstein-Windkessel model which captures the low frequency oscillations of the cardiovascular system. The systolic and diastolic pressures were derived from the mean arterial pressure using an intuitive estimator α, which was calculated based on the envelope of the modeled oscillometric waveform. The α parameter, which reflects the symmetry of the oscillometric waveform, is similar to one of the best performing feature in the present study, i.e., $Ratio_3$. In a more

recent study, they (Barbé et al., 2014) further extended their work to include a statistical learning technique based on ordinal logistic regression for the calibration of oscillometric BP monitors. By applying a linear regression to map the shape of the oscillometric signal to the BP to avoid complex nonlinear models, the method could only estimate the correct BP range but not the specific value of the BP.

3.6 Conclusion

In this chapter, we proposed a novel approach in estimating SBP and DBP using variable characteristic ratios derived from features extracted from the OMWE, on data corrupted with movement artifact. An automatic algorithm based on changes in the oscillometric pulses relative to their respective neighbour pulses was proposed to remove outlier points before the curve fitting process. Substantial reduction in the mean and standard deviation of the BP estimation errors between the MAA algorithm and the RS were obtained upon artifact removal. Comparing all ten features extracted from the OMWE, the MAP feature as well as the two newly proposed features, i.e., $Ratio_2$ and $Ratio_3$, showed superior performance in providing accurate SBP estimates. Using SFFS, we were able to achieve a significant reduction in the mean and standard deviation of differences between the estimated SBP values and the RS (MLR: mean ± SD = −0.3 ± 5.8 mmHg; SVR and −0.6 ± 5.4 mmHg) with only two features, i.e., $Ratio_2$ and $Area_3$, as compared to the conventional MAA method (mean ± SD = −1.6 ± 8.6 mmHg). To the contrary, negligible improvement was achieved for DBP estimation. Comparing both MLR and SVR models, our results showed that the MLR model was able to achieve comparable performance with that obtained from the SVR model despite its simplicity. In the next chapter, automatic artifact detection algorithms for another common phsyiological signal which the PPG signal is studied.

CHAPTER 4: ADAPTIVE TEMPLATE MATCHING OF PHOTOPLETHYSMOGRAM PULSES TO DETECT MOTION ARTIFACT

4.1 Introduction

This chapter introduced an adaptive template algorithm to detect artifact in the PPG signal. Two PPG master templates were generated from the Physionet database (Goldberger et al., 2000) (a publicly available database). The developed algorithm was tested on both short (6s) and continuous PPG (i.e. longer than 30 mins) data collected from the healthy subjects.

4.2 Literature Review

The photoplethysmograph (PPG) is commonly used to monitor heart rate and peripheral capillary oxygen saturation (SpO_2). It has the advantage of being non-invasive, low cost, and portable, which makes it useful in all healthcare settings, for both risk stratification and continuous monitoring. However, the quality of the PPG signal is easily degraded by poor blood circulation, fluctuations in ambient light, as well as motion artifact (Matthew J Hayes & Smith, 1998; Matthew James Hayes & Smith, 2001; Jumadi Abdul Sukor, 2012), which can lead to clinical feature extraction or diagnostic errors. Due to the high susceptibility of PPG signals to artifact, several researchers have questioned the reliability of pulse oximetry in uncontrolled environments, such as normal clinical practice (Costarino, Davis, & Keon, 1987), during exercise (Benoit et al., 1997), and in a home care setting (R Couceiro, Carvalho, Paiva, Henriques, & Muehlsteff, 2014).

Artifact detection is crucial to eliminate poor quality intervals of the PPG waveform that would be impossible to recover via an artifact suppression technique. To date, a number of artifact detection methods have been proposed. These include the morphological methods (Chong et al., 2014; R Couceiro et al., 2014; Selvaraj, Jaryal, Santhosh, Deepak, & Anand, 2008; J Abdul Sukor, Redmond, & Lovell, 2011; X. Sun, Yang, & Zhang, 2012) and statistical descriptor. One limitation of these studies was that

subject- specific templates need to be constructed to account for inherent differences in the PPG waveform morphology across subjects owing to various cardiovascular factors (Hickey, Phillips, & Kyriacou, 2016). Recently, Dao et al. (2017) proposed an algorithm for motion artifact detection using time-frequency features which did not require an a priori pulse segmentation step. Their approach requires 8 s of data, calculating the spectrum of five 4s wide sliding analysis windows, with a 3 s overlap between adjacent windows; variation across these five spectral estimates indicate the presence of signal artifact.

Moreover, most algorithms were only applied to data obtained from the intensive care unit (ICU) or controlled clinical environment, where motion artifacts are likely to be minimized. As the use of medical devices in remote monitoring increases at pace, data are more likely to contain motion artifacts as compared to conventional bedside monitoring. To date, limited artifact detection studies have been performed on datasets containing motion artifacts. Among those few studies which have evaluated their algorithms against motion-corrupted data are Sukor et al. (2011) and Chong et al. (2014). In both studies, only short segments of PPG signals (i.e., 1 minute duration) were used, thus the performance of their respective algorithms on long-duration continuous PPG signals (i.e., longer than 30 minutes), which have been observed to vary with posture or hand elevation (Addison, 2017; Hickey et al., 2016), as well as changes in the vascular resistance, is still unknown.

In this chapter, we propose a novel algorithm for artifact detection using an adaptive pulse shape template, and investigate its performance on signals corrupted with various types of motion artifact. Two master templates are initially generated using data obtained from the PhysioNet MIMIC II database (Goldberger et al., 2000). Instead of using a fixed template, the master template is periodically updated to enable online artifact detection in long-duration continuous PPG signals. Linear correlation is used to classify the PPG

pulses into either good or bad quality categories. The performance of our algorithm is evaluated using data obtained from two different sources: (i) ambulatory long-duration continuous data (i.e., longer than 30 minutes) collected from the wearable Sotera Visi Mobile system (Sotera Wireless Inc.) which contained signals recorded as the subjects performed several types of motion; and (ii) short duration (6 s segments) of ICU data provided by the PhysioNet MIMIC II database. On top of that, the importance of artifact detection in providing reliable SpO_2 estimation was investigated by estimating SpO_2 values from our collected PPG signals.

4.3 Methodology

4.3.1 Signal acquisition

Nineteen subjects (twelve male) aged between 18 and 45 years were recruited for the study and gave informed consent. This study was approved by the Human Research Ethics Advisory (HREA) panel, University of New South Wales (UNSW); reference number HC15398.

A portable physiological signal acquisition device called the Sotera Visi Mobile system (Hravnak M, 2017) (Sotera Wireless Inc., San Diego, California, USA) was used to collect the electrocardiogram (ECG), oscillometric BP (not used in this study), 3D acceleration, and PPG signals from each subject (Figure 4.1). During the data collection process, the ECG electrodes together with a chest accelerometer were attached on the subject's chest. A BP cuff and an arm accelerometer were placed on the subject's left arm. A PPG sensor was placed at the radial artery of the left thumb, and a wrist accelerometer was attached on the left wrist. All recorded data were then wirelessly transmitted and saved in a server to be downloaded later for post-processing.

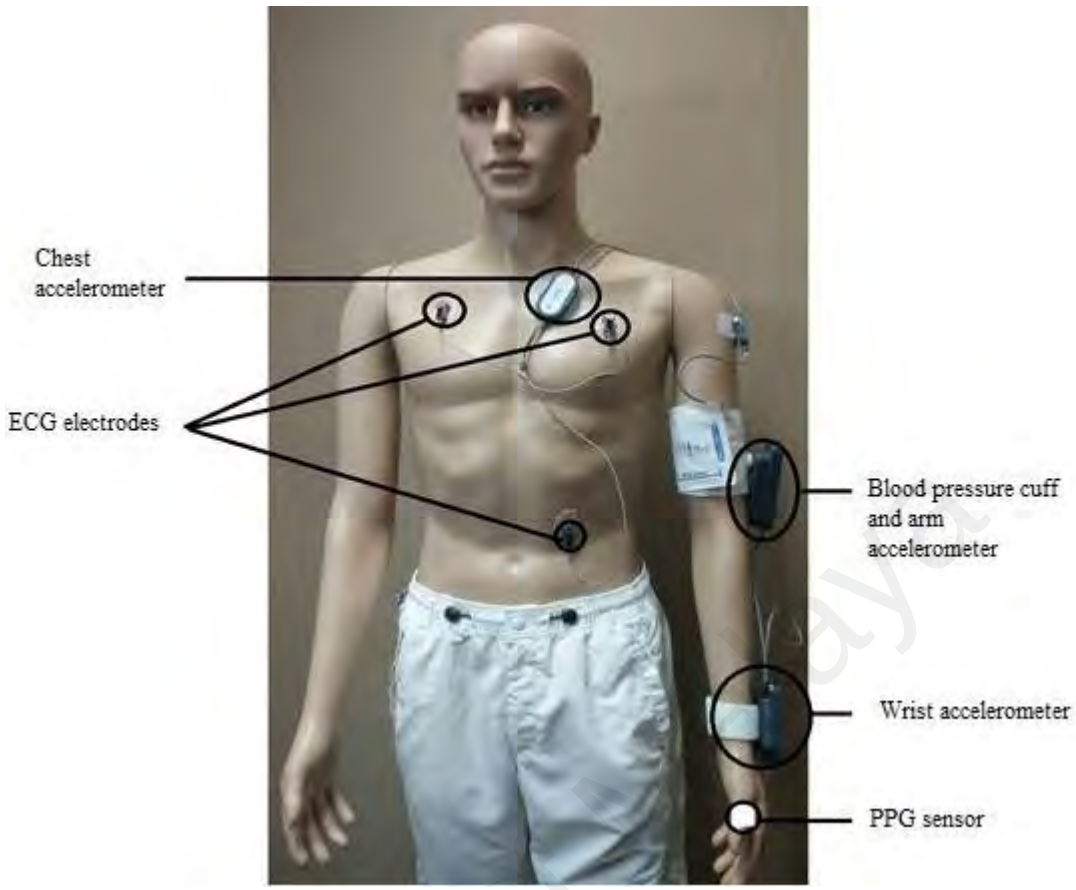

Figure 4.1: Experimental set-up for data collection using the Sotera's ViSi Mobile System.

Table 4.1: List of stationary poses.

Stationary pose	Description	Duration
Sit_S0	Sit stationary on a sofa with both arms by sides.	5mins
Sit_S1	Sit stationary with both arms crossed across the chest.	30s
Stand_S0	Stand still with both arms by the sides of the body.	30s
Lie_S0	Lie down with both arms by the sides of the body.	30s
Lie_S1	Lie on the left side of the body with self-selected arm positions.	30s
Lie_S2	Lie down with face facing downward with self-selected arm positions.	30s
Lie_S3	Lie on the right side of the body with self-selected arm positions.	30s
Hand_S0	Place the left arm (the side of the arm with device attached) on the table while sitting.	30s

Prior to the start of the experiment, each subject was allowed five minutes' rest (in the sitting position) to ensure steady state heart rate and BP readings. Each subject was then required to perform a predefined set of movements and poses usually encountered in daily life, as described in Tables 4.1 and 4.2. The stationary poses were normally performed in between two movements. Each movement was performed naturally instead of adhering

to a predefined movement speed. During the experiment, video recordings were taken to record the movements of the trunk, arms and lowerbody.

Table 4.2: List of movements.

Movement type	Description	Duration (Median with interquartile range), s
Arm_M0	Lift the left arm (the arm with device attached) overhead and back down, three times, consecutively.	7.3 (6.8-10.0)
Arm_M1	Lift both arms overhead and back down, five times, consecutively.	15.3 (11.5-15.3)
Arm_M2	Abduct both arms away from midline of the body 90 degrees, and back, five times, consecutively.	12.0 (10.0-13.5)
Arm_M3	Shuffle playing cards with both hands.	30
Arm_M4	Bend the left thumb five times slowly, consecutively.	7.3 (6.1-9.1)
Arm_M5	Bend the left elbow five times, consecutively.	9.4 (9.0-11.9)
Arm_M6	Bend the left wrist from side to side five times, consecutively.	8.5 (6.9-10.0)
Arm_M7	Eat food from a plastic packet.	30
Arm_M8	Flip through pages of a book slowly.	30
Body_M0	Sit-to-stand with both arms by sides, five times, consecutively.	17.8 (14.5-22.7)
Body_M1	Standing, twist the body from side to side, five times, consecutively.	15.0 (13.4-17.3)
Body_M2	Walk slowly (for around 100 m).	28.0 (14.2-42.8)
Body_M3	Sit-to-lie-to sit, five times, with pauses in between.	27.6 (21.0-32.9)
Body_M4	Walk up the stairs from the ground floor to the first floor.	13.9 (11.5-21.5)
Body_M5	Pick up a pen from the floor using the left hand.	8.0 (5.8-9.3)
Body_M6	Walk down stairs from the first floor to the ground floor.	15.9 (10.0-20.8)

4.3.2 Development of a gold standard (GS) annotation

In this study, we adopted the method applied in Sukor et al. (2012) and Sukor et al. (2011) for pulse oximetry and BP signals to develop a gold standard (GS) annotation, against which algorithm performance is compared. First, two clinical experts (termed

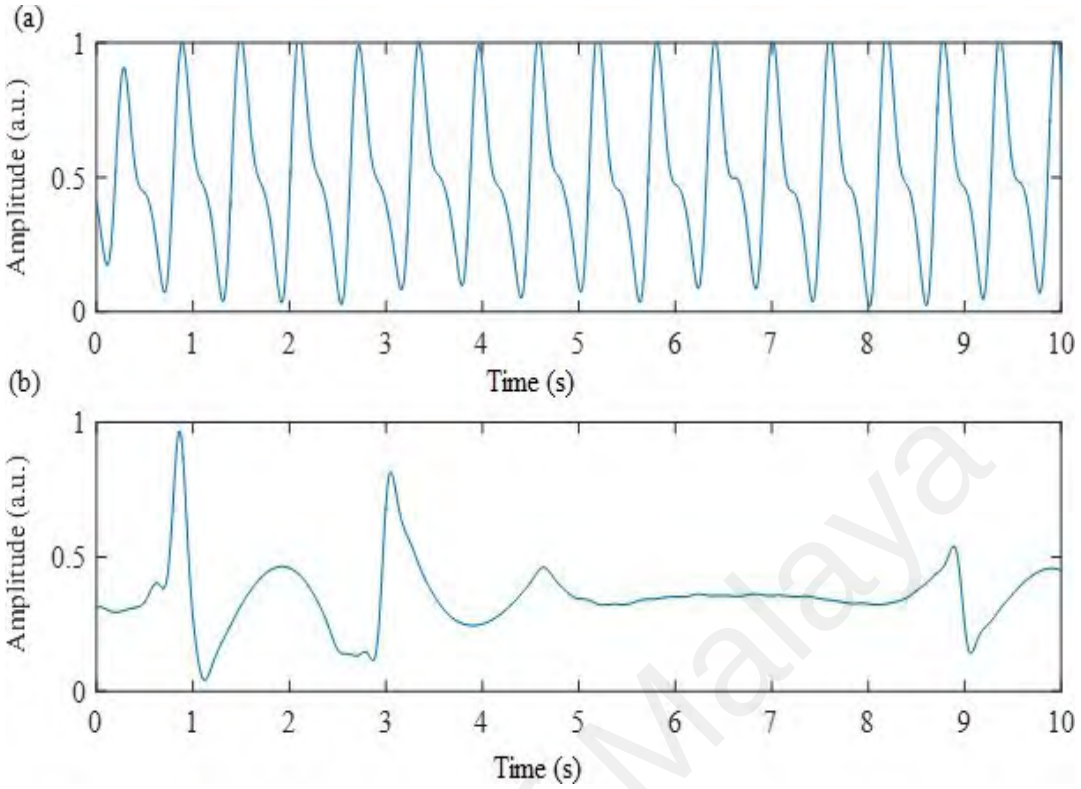

Figure 4.2: Illustration of: (a) a PPG signal interval containing no artifact and all good pulses; (b) containing artifact and bad PPG pulses.

Rater 1 and Rater 2) were presented with the simultaneously-recorded ECG and PPG signals using a custom-designed MATLAB graphical user interface (GUI) software tool. By observing the shape of the PPG pulses and referring to the R-wave from the simultaneously-recorded ECG signal, the clinical experts could classify each PPG pulse into either good or bad quality categories. A good pulse was defined as a pulse that matches a typical morphology, as shown in Figure 4.2(a), and that had similar morphology, amplitude, and width to other adjacent pulses. A bad pulse was defined as a pulse which has significantly different morphology, amplitude, and width to other adjacent pulses, as shown in Figure 4.2(b). Then, a third clinical expert was asked to re-annotate all recordings to reconcile any disagreement in the annotations of Raters 1 & 2. This reconciled annotation result was used as the GS.

4.3.3 Algorithm development

Figure 4.3 illustrates the artifact detection algorithm proposed in the present study.

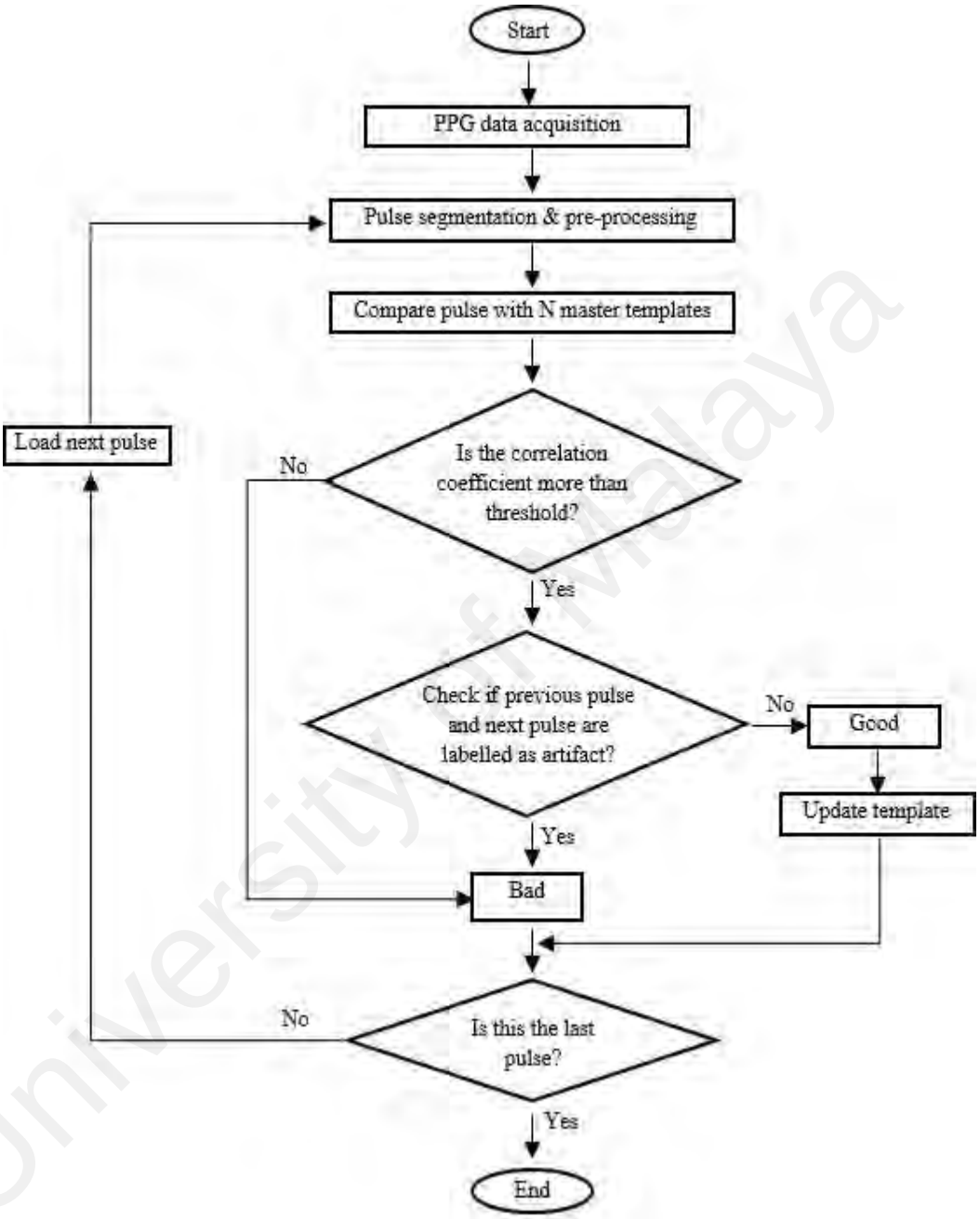

Figure 4.3: Flow chart illustrating the proposed artifact detection algorithm using adaptive template matching.

4.3.3.1 Preprocessing and pulse segmentation

Figure 4.4 illustrates the pulse segmentation method used in the present study. Firstly, bottom points of the PPG signal were identified using a minimum filter with a pulse width of 0.5 s. In order to ensure the identification of valid bottom turning points, the reference

pulse width ($refPW$) was first determined based on the duration between the first two bottom points.

$$refPW = Bottom\ point_2 - Bottom\ point_1 \tag{4.1}$$

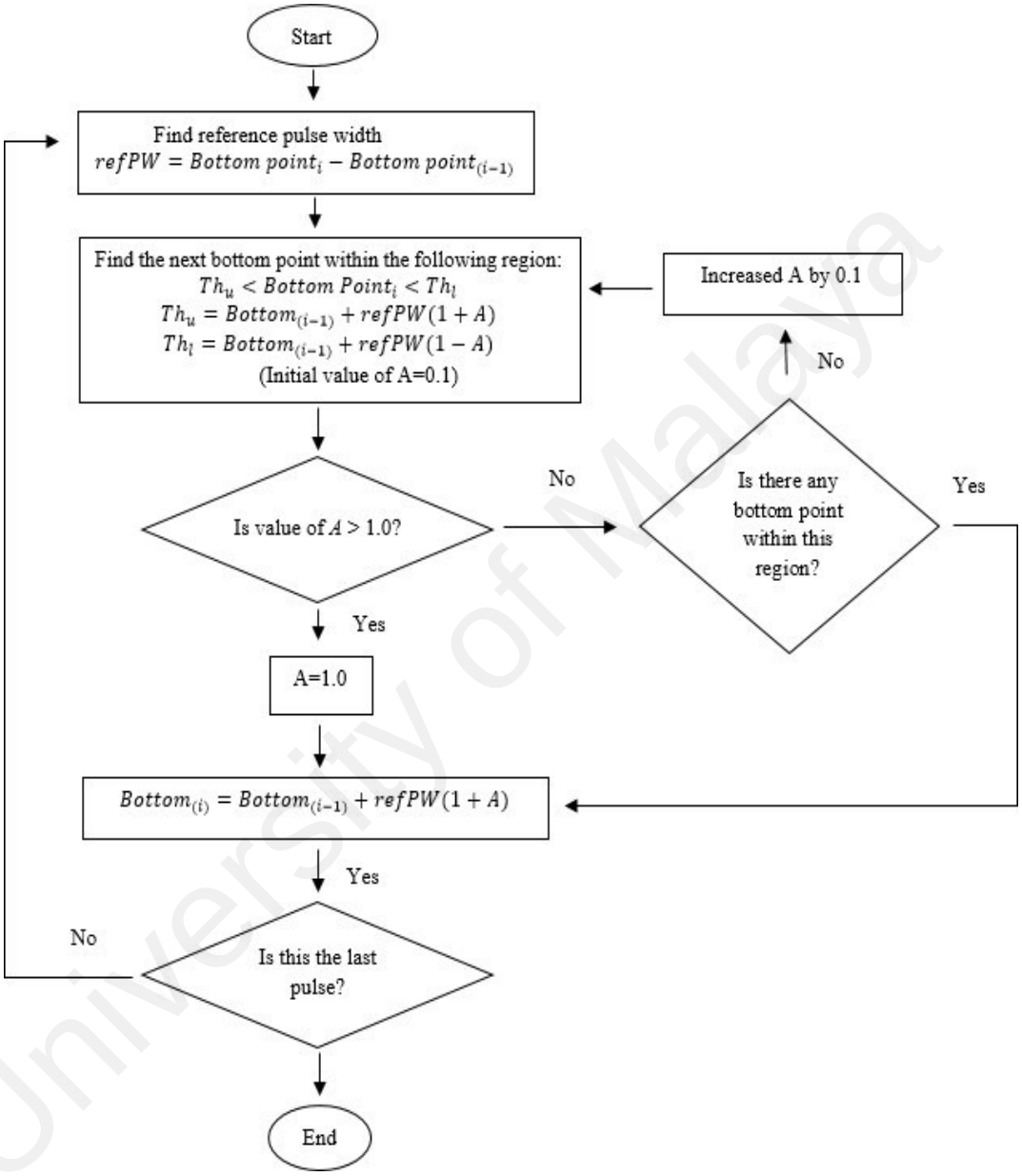

Figure 4.4: Flow chart of pulse segmentation algorithm.

An adaptive threshold technique was used to identify the time interval where the next bottom point should be located. This is done by using a pair of threshold limits named the upper threshold limit (Th_u) and the lower threshold limit (Th_l).

$$Th_u = Bottom_{(i-1)} + refPW(1 + A) \tag{4.2}$$

$$Th_l = Bottom_{(i-1)} + refPW(1 - A) \tag{4.3}$$

$Bottom_{(i-1)}$ represents the time where the current bottom point occurs, while the initial value for A was set at 0.1.

The next bottom point is expected to be located in the time interval between Th_u and Th_l. If no bottom point is detected, the value of A is increased by 0.1 and the same procedure is repeated until a bottom point is identified, or A has reached a value of 1.0. If no beat was found when A has reached a value of 1.0, then the value of A will be set to 1.0. The algorithm searches forward within an interval of width $\mathbf{2}\boldsymbol{A}$ seconds centered at $\boldsymbol{refPW}$ seconds after the most recently detected bottom point. If no bottom turning point is found, $\boldsymbol{A}$ is increased to widen the search window.

Next, each PPG pulse was filtered with a band-pass Butterworth filter (0.5-5 Hz pass band, assuming a maximum heart rate of 300 beats per min) using forward-backward filtering to achieve a zero-phase response. In order to assess the accuracy of our pulse segmentation results, each of the segmented PPG pulse was compared against the simultaneously-recorded ECG signals as the GS to check if the identified pulse was actually a PPG pulse. Based on our analysis, the pulse segmentation accuracy was 98.2%; detection errors occurred in intervals containing artifact where the signal was completely obscured by noise.

4.3.3.2 Master template generation

In this study, the principal component analysis (PCA) technique was used to generate a number of master templates. The master templates were created using all good pulses extracted from the PhysioNet MIMIC II database, which also contains the signal quality annotations. This amounted to a total of 6,802good pulses from the 825 6-s clean PPG segments contained in the database, with each clean segment containing 6-14 pulses.

Before PCA is applied, each PPG pulse is first segmented from the signal and uniformly re-sampled in time to contain 256 samples, hence normalizing all pulse durations. The master templates are then created using two cascading applications of PCA. PCA is implemented using the `pca` function in MATLAB R2015b.

PCA is first applied independently to each of the 825 clean PPG segments, each of which contains between 6 and 14 pulses. For each clean PPG segment, the input data is a matrix with dimensions of 256 samples (of each normalized pulse) × 6-14 pulses (per clean PPG segment). Standard data preparation practice is followed, subtracting the mean of each column and then dividing the column by its standard deviation to so the column has unit variance. Note also, the 256 rows are taken as observations and the 6-14 columns are taken as variables; the application of PCA in this way results in a principal components (PCs) which are effectively weighted sums of each beat contained in the PPG segment. The resulting principal components (PCs) which contain 95% of the variance for this clean PPG segment serve as an intermediate master template(s) for this clean PPG segment, and will be used later in a second application of PCA, this time across all 825 segments. This first per-segment application of PCA resulted in between 1 and 3 PCs for each of the 825 segments, giving the total of 1,485 PCs from all the 825 segments.

PCA was then applied for a second time, to these 1,485 intermediate templates. This time the input data dimensions were 256 samples (of each normalized pulse) ×1,485 pulses (from the first application of PCA, above). The result of this second application of PCA was two final principal components which contained 99% of the variance (PC1=85%, PC2=14%), as shown in Figure 4.5.

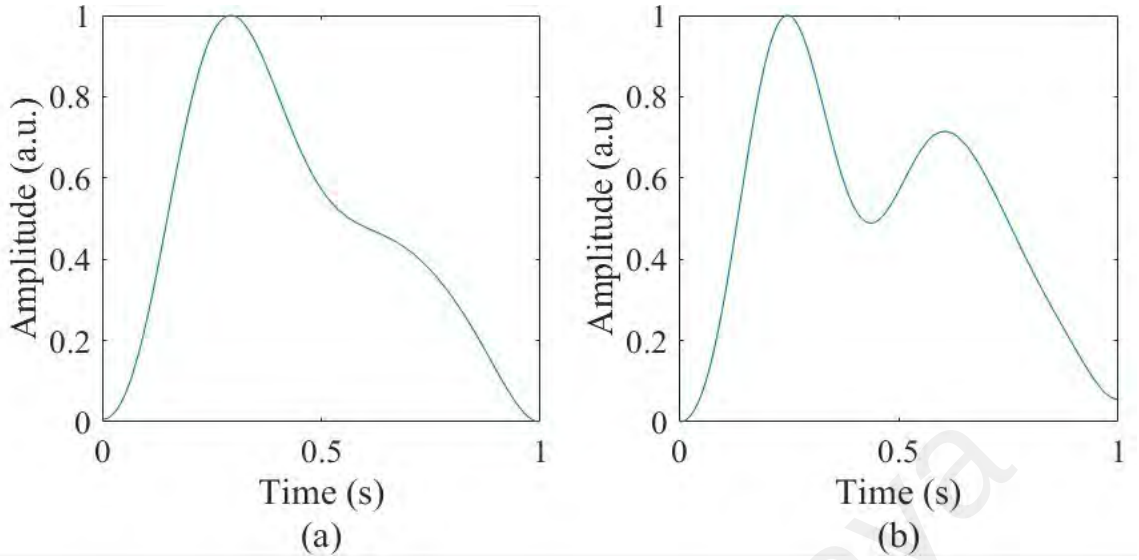

Figure 4.5: Master templates generated by using the PCA method based on clean pulses extracted from the PhysioNet MIMIC II database: (a) time-normalized master template (first principle component, PC1) with one peak; and (b) time-normalized master template (second principle component, PC2) with two peaks.

4.3.3.3 Template matching

After pulse segmentation, linear resampling was applied on each PPG pulse (Q. Li & G. D. Clifford, 2012) to match the pulse width of the master template. The number of samples used for linear resampling was 256, which corresponds to a heart cycle duration of 1 s. Pulses with pulse widths less than that of the master template were linearly stretched, whereas those with a longer pulse width were compressed to match the length of the master template. Normalization of pulse amplitude was done on both master templates and each PPG pulse to fall in the interval between 0 and 1. Next, Pearson's correlation coefficient was calculated between the normalized linearly re-sampled PPG pulses and each of the two normalized master templates. The resultant maximum correlation coefficient value was taken as the signal quality index (SQI) for the PPG pulse under investigation.

$$SQI = corr(Current\ pulse, Master\ template) \tag{4.4}$$

Pulses with an SQI value exceeding the correlation threshold value (Th) are considered as good. This was then followed by a template updating procedure. An exponential

smoothing method was used, as described in Eq. 4.5. This allows us to generate master templates that evolve with time should the pulse characteristics change.

$$T_{norm,new} = \alpha T_{norm,c} + (1 - \alpha) P_{norm} \quad (4.5)$$

$T_{norm,new}$ refers to the newly-updated normalized master template, $T_{norm,c}$ refers to the current normalized master template,α refers to the learning rate, while P_{norm} refers to the current normalized good pulse.

4.3.3.4 Comparison of adjacent pulses

As clinical experts frequently label PPG signals by referring to nearby pulses instead of examining each pulse individually, we have taken an extra step to compare each pulse to previous and following pulses. If both pulses were classified as bad, the current pulse will be automatically labelled as bad.

4.3.3.5 Determination of optimal parameter values

Ten subjects were randomly selected as the training set (named "outer training set") while the remaining nine subjects were withheld to be used as the testing set once the best parameter values were selected (named "outer test set").The "outer training set" was further differentiated into the "inner holdout set" and the "inner training set", which were used to determine the optimum parameter values based on the standard ten-fold cross validation approach. The best learning rate (α) and correlation threshold (Th) values were selected as those which yielded the highest classification accuracy when evaluated on the "outer training set". To do this, each of these parameters was first varied between 0 and 1 with a step size of 0.05 to obtain the classification accuracy. This is further refined by varying the highest performing α and Th combination (α_1 and Th_1) within the range of $\alpha_1 \pm 0.05$ and $Th_1 \pm 0.05$, with a smaller step size of 0.01. Once the parameter selection step was complete, the "outer test set" was used for testing.

4.3.4 Evaluation of our algorithm using the PhysioNet MIMIC II database

We also applied our algorithm to a PPG dataset developed by the PhysioNet MIMIC II database (Goldberger et al., 2000) for benchmarking purposes. This clinical expert-labelled dataset contains simultaneously-recorded ECG, PPG and BP signals from 104 subjects in an ICU, each segment with a 6s duration, containing a total of 1437 segments with signal quality annotations. Two clinical experts independently segmented and labelled the pulses into good (1), bad (0), or uncertain (other) quality categories based on the waveform around the time when arrhythmia alarm occurs, and disagreement was reconciled by a third clinical expert. Out of the 1437 segments of data with signal quality annotations, only 1055 segments, which were labelled as good (1) or bad (0), were used in this study. The distribution of the annotation results based on both datasets (i.e., PhysioNet database and those collected from the Sotera Visi Mobile system) is shown in Table 4.3.

Table 4.3: Summary of PPG pulse quality distributions for the PhysioNet MIMIC II database and the Sotera Visi Mobile dataset.

Number of PPG beat quality annotations	PPG beat quality categories		
	Good	Bad	Total
PhysioNet MIMIC II database	6,802	1,663	8,465
SoteraVisi Mobile dataset	40,706	27,194	67,900
Total	47,508	28,857	76,365

4.3.5 SpO_2 estimation

Ten segments of one-minute PPG signals were extracted from each subject, with five segments labelled as good while the remaining labelled as bad. The labelling was performed based on our previous classification results, where good segments were those containing all good pulses, whereas the majority of pulses in the bad segments were classified as bad. Out of the nineteen subjects, we were unable to obtain SpO_2 estimates from two subjects due to missing information about the amplifier gain setting during the

data acquisition process.

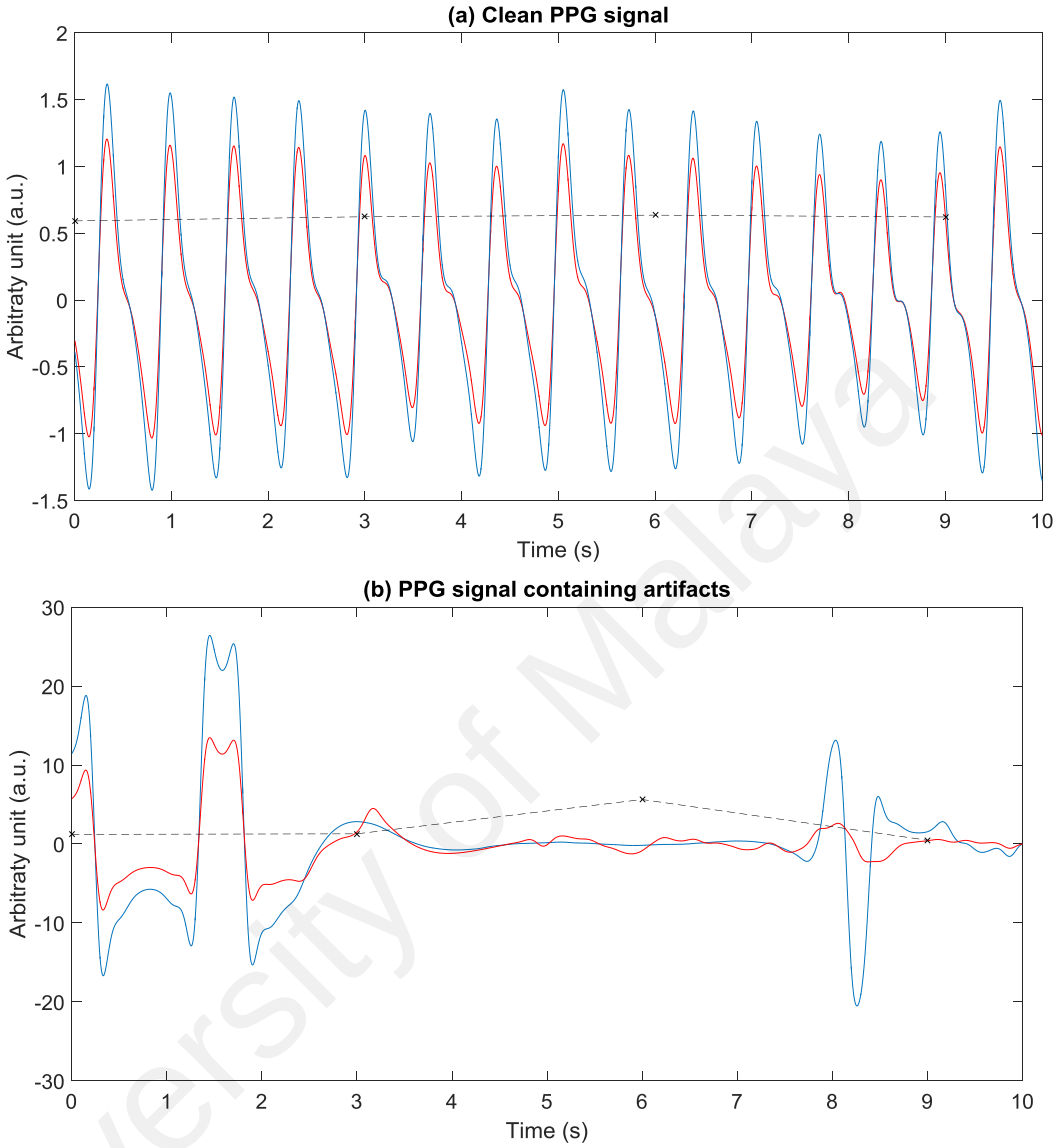

Figure 4.6: Illustration of (a) good PPG signal and (b) bad PPG signal containing artifacts. Blue color line represents the infrared PPG signal (PPG-IR), red color line represents the red PPG signal (PPG-RED), while the black cross mark represents R values computed for the previous three-second PPG segment based on Equation 4.7.

In order to estimate SpO_2 values, the infrared and red PPG signals were separated into the AC and DC components. The pulsatile components of the infrared and red PPG signals were denoted as AC_{IR} and AC_{RED}, while the baseline components were denoted as DC_{IR} and DC_{RED}, respectively. Then, the "ratio-of-ratio" was defined as:

$$R = \frac{AC_{RED} / DC_{RED}}{AC_{IR} / DC_{IR}} \tag{4.6}$$

For every three second of the PPG signal, the SpO_2 value was estimated according to the empirical linear approximation as in Equation 4.7.

$$SpO_2(\%) = 112.91 - 28.09 * R \tag{4.7}$$

4.4 Results

In this section, we first report the results of the optimized learning rate (α) and correlation threshold values (*Th*) to achieve the highest classification accuracy. In addition, we show the effect of varying the learning rate (α) and correlation threshold values (*Th*) separately. We then present the performance of our artifact detection algorithm using the optimized parameter values on our dataset, which contains various types of motion-corrupted PPG signal. Lastly, for benchmarking purposes, we report the performance of our algorithm on the publicly-available PhysioNet MIMIC II database.

4.4.1 Optimization of the learning rate (α) and correlation threshold values (*Th*)

Data collected using the Sotera Visi Mobile system were split into separate training (ten subjects selected randomly) and testing (the nine remaining subjects) groups. As shown in Figure 4.7, by varying the learning rate (α) and correlation threshold values (*Th*) from 0 to 1 with a step size of 0.05 on the training data, we found that region with a learning rate (α) of 0.95 and a correlation threshold value (*Th*) of 0.9 yielded the highest accuracy. We further calculated the classification accuracy with a finer step size of 0.01 for both learning rate (α) (within the range 0.90 to 1.00) and correlation threshold value (*Th*) (within the range 0.85 to 0.95).The optimized learning rate (α) and correlation threshold (*Th*) value were 0.93 and 0.91. By having a learning rate (α) of 0.93, each new template would contain 93% of the information from the current template and the remaining information from the current good pulse. With these optimized parameters, our algorithm was able to achieve an overall accuracy of 92.5 ± 3.1% (median = 92.3%, interquartile range = 5.1%) with a sensitivity and specificity of 90.7 ± 5.6% (median = 89.2%, interquartile range = 7.7%) and 94.0 ± 2.3% (median = 93.7%, interquartile range =

4.1%), respectively, when evaluated on all subjects in the training dataset. Meanwhile, an overall accuracy of 91.5 ± 2.9% (median = 91.0%, interquartile range = 5.5%), with a sensitivity and specificity of 94.1 ± 2.7% (median = 94.1%, interquartile range = 4.4%) and 89.7 ± 5.1% (median = 89.2%, interquartile range = 7.4%) were achieved when evaluated on all subjects in the testing dataset.

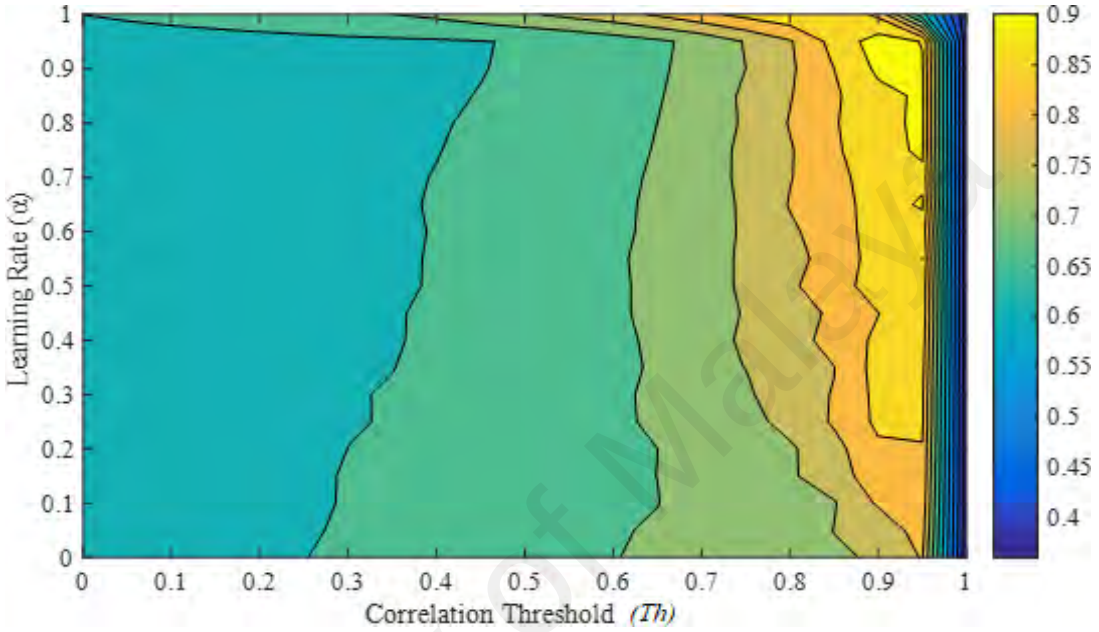

Figure 4.7: Response surface plot of the classification accuracy with respect to correlation threshold (*Th*) value and learning rate (α) (search step size = 0.05) using the training data. Color bar on the right indicates the accuracy scale. A learning rate of α = 0.95 with a correlation threshold value (*Th*) of 0.90 yielded the highest accuracy (92.0%).

4.4.2 Effect of varying the correlation threshold (*Th*) value

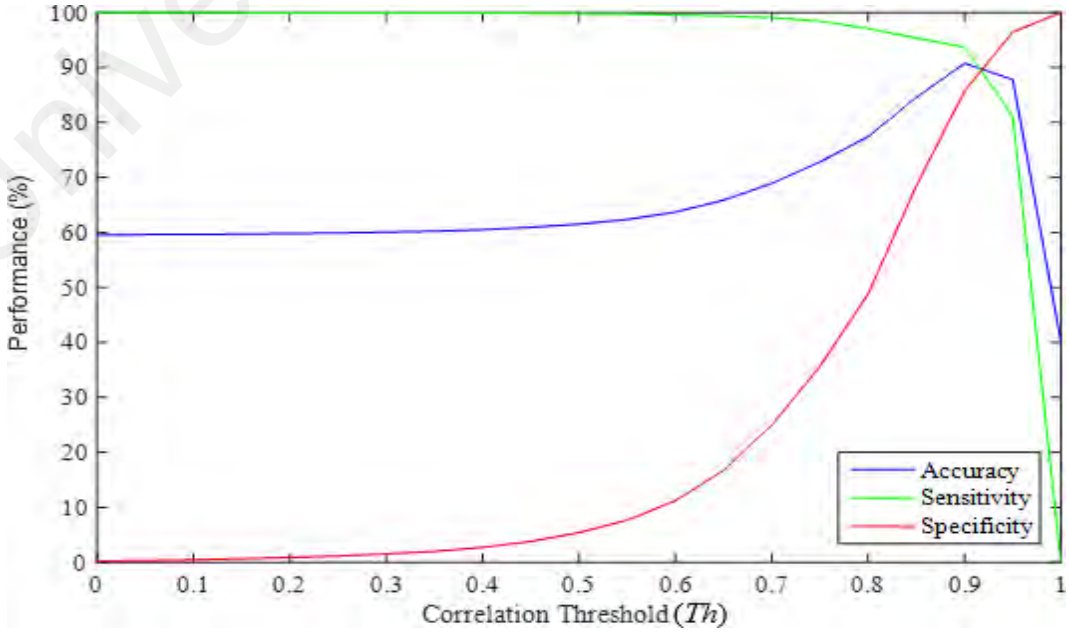

Figure 4.8: Classification results with varying correlation threshold (*Th*) values at a fixed learning rate (α) of 0.93.

Figure 4.8 illustrates the effect of changing the correlation threshold (*Th*) value with step size of 0.05 on the classification accuracy, sensitivity, and specificity at a fixed learning rate (α) of 0.93 using the testing dataset. At low correlation threshold (*Th*) values, almost all pulses were classified as good (accuracy: 58.6%; sensitivity: 100.0%; specificity: 0.2%).With an increase in the correlation threshold (*Th*) value above 0.6, both the accuracy and specificity levels showed a steep increase, at the expense of a slight drop in the sensitivity (accuracy: 63.7%; sensitivity: 99.6%; specificity: 11.2%, with a correlation threshold (*Th*) value of 0.6). The highest accuracy was achieved when the correlation threshold (*Th*) value reached 0.91 with an accuracy of 91.5%, sensitivity of 94.1% and specificity of 89.7% respectively.

4.4.3 Effect of varying the learning rate (α)

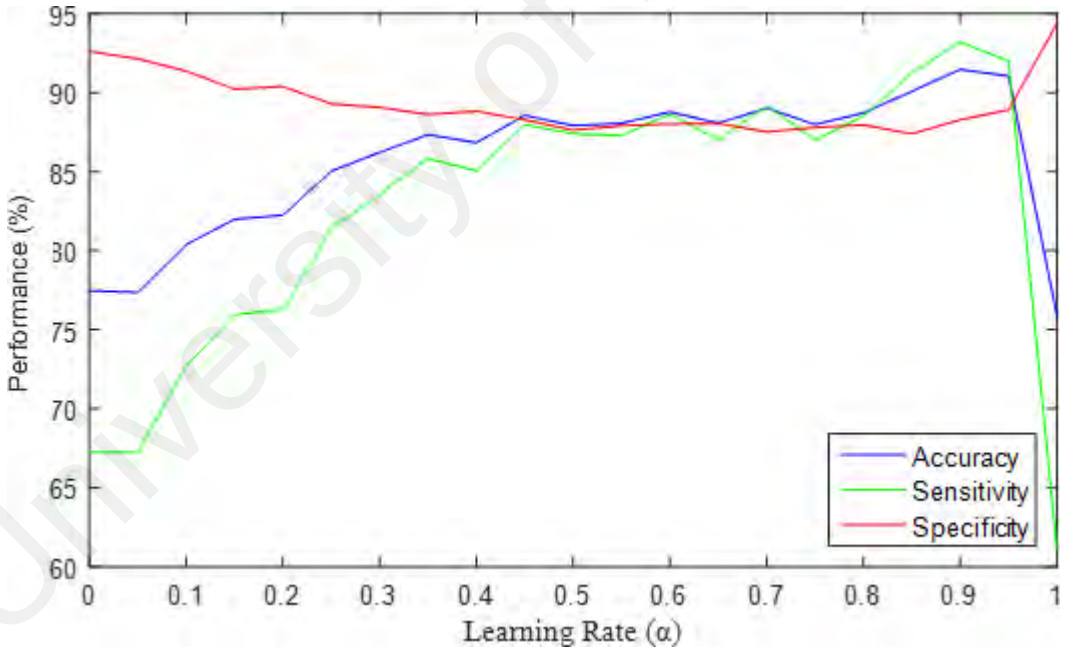

Figure 4.9: Classification results with varying learning rate (α) at a fixed correlation threshold (*Th*) value of 0.91.

Figure 4.9 illustrates the effect of changing the learning rate (α), with step size of 0.05, on the classification accuracy, sensitivity, and specificity at a fixed threshold value (*Th*) of 0.91 using the testing dataset. With no template update (i.e., with a learning rate (α) of 0), although most artifact was identified correctly (specificity: 92.6%), 32.8% of the good pulses were wrongly classified as artifact (sensitivity: 67.2%), thus leading to poor

accuracy (77.5%). The ability of the algorithm to correctly identify good pulses substantially improved with an increase in the learning rate (α) from 0.05 to 0.45. Fluctuation in the classification results happened when the learning rate (α) was increased further from 0.45 to 0.8. The highest accuracy was achieved when the learning rate (α) reached 0.93, with accuracy of 91.5%, sensitivity of 94.1% and specificity of 89.7%, respectively.

4.4.4 Algorithm performance on different movements

Tables 4.5 and 4.6 show the mean classification results for stationary poses and movements on the testing subjects, respectively. Our algorithm achieved a mean accuracy of 91.3% when tested on data containing stationary poses, and 94.7% when evaluated on movement data. The average sensitivity for the stationary poses (94.3%) was larger when compared to that of the movements (83.1%). An opposite trend was observed in the average specificity, where a significantly smaller value was obtained for the stationary poses (82.0%) when compared to that of movements (94.7%).

Table 4.4: PPG pulse quality classification results for stationary poses (mean±SD).

Stationary	Accuracy (%)	Sensitivity (%)	Specificity (%)
Sit_S0	87.0 ± 8.1	88.5 ± 7.9	81.1± 15.1
Sit_S1	89.5 ± 15.2	95.9 ±2.2	86.2± 18.7
Stand_S0	86.4 ± 20.3	88.3 ± 14.3	85.9±17.9
Lie_S0	95.8 ± 4.9	96.4 ±2.5	85.4±18.6
Lie_S1	89.0 ± 3.5	93.3±2.6	85.4±20.4
Lie_S2	95.1 ± 7.4	97.4± 6.4	84.2±24.6
Lie_S3	94.3 ± 8.1	98.4± 3.8	66.7±22.4
Hand_S0	93.8 ± 6.2	96.1± 7.5	75.9± 21.7
	91.3 ± 4.2	94.3±3.9	82.0±6.9

Table 4.5: PPG pulse quality classification results for movements (mean ± SD).

Movement	Accuracy (%)	Sensitivity	Specificity (%)
Arm_M0	98.3 ± 2.7	75.6 ± 0.0	99.3 ± 2.7
Arm_M1	97.0 ± 4.5	78.9 ± 0.0	98.0 ± 4.5
Arm_M2	99.2 ± 2.6	80.5 ± 13.4	100 ± 0.0
Arm_M3	96.2 ± 3.5	86.7 ± 8.9	96.4 ± 3.8
Arm_M4	88.3 ± 0.0	89.4 ± 0.0	86.0 ± 18.8
Arm_M5	97.0 ± 7.0	78.9 ± 0.0	97.5 ± 7.0
Arm_M6	91.1 ± 9.1	83.3 ± 0.0	92.3 ± 12.5
Arm_M7	87.3 ± 6.5	89.8 ± 9.7	86.7 ± 7.6
Arm_M8	93.5 ± 5.3	95.8 ± 5.9	91.1 ± 5.3
Body_M0	94.4 ± 5.8	72.7 ± 14.2	95.6 ± 3.7
Body_M1	97.9 ± 3.7	79.4 ± 13.8	98.7 ± 3.5
Body_M2	88.1 ± 12.9	80.8 ± 10.9	88.4 ± 12.9
Body_M3	99.3 ± 1.2	77.6 ± 6.5	99.5 ± 8.9
Body_M4	95.9 ± 3.1	98.9 ± 1.2	93.7 ± 3.1
Body_M5	97.2 ± 6.1	78.1 ± 4.1	97.9 ± 5.5
Body_M6	92.9 ± 12.1	83.9 ± 0.0	93.1 ± 12.2
	94.7 ± 4.1	83.1 ± 5.3	94.7 ± 4.6

4.4.5 Classification results on the PhysioNet MIMIC II dataset

Table 4.6: Comparison of classification performance between our algorithm and Li et al. (Q. Li & G. D. Clifford, 2012) on the PhysioNet MIMIC II database.

Algorithm	Accuracy (%)	Sensitivity (%)	Specificity (%)
Our algorithm	98.0	99.0	96.1
Li et al. method (Q. Li & G. Clifford, 2012)	95.2	99.0	80.6

In this study, the same optimized correlation threshold (*Th*) value and learning rate (α) as described in Section 2.3.A were used. Compared to Li et al. (2012), our algorithm produced a higher average accuracy (98.0% vs. 95.2%) even though we used a fixed correlation threshold (*Th*) value and learning rate (α) derived from our training cohort. Although our average sensitivity results were the same (both 99.0%), our algorithm yielded a much higher specificity compared to Li et al. (2012) (96.1% vs. 80.6%).

4.4.6 SpO_2 estimation

Table 4.8 shows the estimated SpO_2values (both mean and standard deviation) forboth good and bad segments from all the seventeen subjects. Overall, the estimated SpO_2

values for the good PPG segments were above 94%, except for subjects 17 and 19. This was caused by the presence of several unavoidable bad pulses in the good PPG segments. These subjects may have accidentally moved their fingers or hands when they were supposed to be performing stationary poses. On the contrary, the estimated SpO_2 values for the bad segments were below 91%, with an average of 84.81%, much lower than the reported healthy SpO_2 range (i.e. 95% - 100%). Besides, as compared to the good PPG segments, the standard deviations of the estimated SpO_2 for the bad segments were also much greater.

Table 4.7: Mean and standard deviation of the estimated SpO_2 values for both clean and bad PPG segments contaminated by artifact.

	Good PPG segments		Bad PPG segments	
Subject	**Mean (%)**	**SD**	**Mean (%)**	**SD**
1	96.5	1.8	87.0	7.3
2	96.7	3.0	85.3	7.3
3	97.4	0.9	74.9	35.0
4	96.7	2.7	86.5	9.0
5	96.6	2.9	82.7	35.2
6	95.3	1.2	84.3	26.5
7	94.3	3.1	87.4	8.5
9	97.9	1.3	89.8	9.8
11	95.6	2.1	89.5	16.8
12	97.9	1.4	83.7	33.3
13	96.8	2.3	89.8	6.7
14	99.0	1.4	90.3	14.9
15	94.4	1.7	90.5	12.8
16	97.3	1.3	73.3	42.2
17	90.6	4.0	76.1	38.4
18	95.8	2.5	83.7	22.9
19	90.4	1.2	87.1	4.8
Average	**95.8**	**2.3**	**84.8**	**5.4**

4.5 Discussion

Accurate derivation of physiological parameters, such as SpO_2, from the PPG signal recorded in an unsupervised environment is challenging in the presence of movement artifact which affects the signal quality. Several studies have attempted to detect artifact in the PPG signal using additional sensing devices, such as accelerometer (B. Lee et al.,

2010), extra reference signals, such as ECG (Foo & Wilson, 2006), as well as various signal processing methods, including Gaussian filtering (Karlen et al., 2012) and morphological waveform analysis (R Couceiro et al., 2014; J Abdul Sukor et al., 2011). However, none of these studies have investigated the effectiveness of their artifact detection techniques on continuous PPG data recorded for a duration of more than 30 minutes. Previous studies have reported continuous variation in PPG morphological waveforms within individual subjects due to respiratory activity (Addison, 2017) and changes hand position (Hickey et al., 2016).

In this chapter, we have introduced a novel and simple algorithm which is suitable for online artifact detection of continuous PPG signal recording without requiring additional sensors. Since the algorithm requires information about the next pulse in order to make a decision on the pulse under analysis, the online implementation of the algorithm will have a time delay of one pulse plus processing time (within 2s) when making a decision about the current pulse. Our results show that the algorithm was able to achieve high accuracy on both short (6 s) (i.e., PhysioNet MIMIC II dataset, with an accuracy of 98.0%, sensitivity of 99.0% and specificity of 96.1%) and continuous (around 40 mins) unsupervised datasets (our own dataset, with an accuracy of 91.5%, sensitivity of 94.1% and specificity of 89.7%). When tested on our dataset, the algorithm yielded significantly lower specificities for stationary poses when compared to those activities involving movement (Tables 4.5 and 4.6). Although subjects were requested not to move during the stationary pose experiments, artifact may occur due to unintentional movement. This may lead to some minor artifact contaminating the signal, creating waveform shapes resembling good signals, thus making artifact detection more challenging. In contrast, artifact caused by intentional movement was more easily identified as the larger movements resulted in more obvious artifact.

To date, various artifact detection algorithms have been proposed for the PPG signal.

Li et al. (2012) developed four signal quality metrics, including direct matching, linear resampling, dynamic time warping, and clipping detection, and fused this signal quality information for artifact classification using a machine learning method. Sukor et al. (2012) extracted five different features from the PPG pulses, which comprised of the amplitude, trough depth difference, pulse width, Euclidean distance to the average of previous pulses, as well as amplitude ratios. A decision tree was then used to classify the pulse. The characteristics of the PPG signal, which vary over time (Elgendi, 2016), requires the threshold values for the features to be determined for individual datasets to maintain high performance. This may not be suitable for long-term continuous PPG analysis. In order to address this, we have generated two master templates, based on the bulk data obtained from the PhysioNet MIMIC II database, and updated the master template thereafter according to each incoming good pulse, thus making our algorithm robust and suitable for online artifact detection purposes. In this study, we demonstrated a large improvement in the classification results when template updating was applied (accuracy: 91.5%; sensitivity: 94.1%; specificity: 89.7%), compared to no template adaptation (accuracy: 77.5%; sensitivity: 67.2%; specificity: 92.6%). Furthermore, our algorithm only requires the selection of two variables, which include the correlation threshold (*Th*) value and the learning rate (α). By using the optimized parameter values trained with our own dataset, our algorithm was able to achieve a high accuracy when evaluated on the PhysioNet MIMIC II database without retraining.

Karlen et al. (2012) calculated the SQI of their PPG pulses by comparing each of the pulse to a reference template generated based on ten previous good pulses. Although a high sensitivity for beat segmentation (96.21%) was reported in Karlen's study (Karlen et al., 2012), the datasets used by their study (i.e., the Capnobase (CB) and the Complex System Laboratory (CSL) databases) contained only 0.7% and 5.8% of artifact data, respectively. These datasets were obtained from the operating room and the ICU, where

the subjects were anesthetized. To the contrary, our data contains 40.05% artifact data. Moreover, similar to Li's study (Q. Li & G. D. Clifford, 2012), Karlen's study (Karlen et al., 2012) involves a longer processing time compared to our study, as a new template needs to be generated for each subject.

SpO_2 reflects the amount of oxygen in the blood, and is defined as the percentage ratio of the oxygenated haemoglobin to the total amount of haemoglobin in the blood. A good blood oxygenation is necessary in order to ensure adequate supply of energy to our muscle for proper functioning. Under healthy body condition and a well-controlled environment, SpO_2 of an subject should only vary between 95% and 100% (Harvey et al., 2018; Organization, 2011; R. Yousefi et al., 2014). Multiple factors may contribute to abnormal SpO_2 values: abnormal haemoglobin amount in the blood, medical dyes or manicure that could influence the level of light transmission, large body motion causing motion artifacts in the acquired data (Harvey et al., 2018; Yan, Poon, & Zhang, 2005; Rasoul Yousefi et al., 2013) as well as blockage of blood flow due to excessive pressure on the arms or fingers (Organization, 2011). In this study, the good PPG segments (based on our artifact detection results) were able to achieve normal SpO_2 ranges, with an average of 95.84% across all subjects, while the bad PPG segments showed much lower SpO_2 values, with an average of 85%. This demonstrates the importance of a prior artifact detection stage to assure quality of the acquired signals and thus the reliability of the extracted physiological variables (SpO_2 in this case), as false alarms indicating hypoxia could be triggered when bad signals are acquired and used to extract these important parameters.

4.6 Conclusion

As physiological signals play an important role in clinical diagnosis, it is crucial to evaluate signal quality before making any important clinical decision. In this chapter, we have developed an effective online artifact detection system suitable for continuous PPG

monitoring based on dynamic templates, where a new template is generated for each incoming good PPG pulse. We have evaluated the performance of our algorithm on both short-segment datasets and continuous PPG signals containing various motion artifacts. As compared to using a fixed template, our adaptive template method demonstrated a large improvement in pulse classification accuracy, up from 77.5% to 91.5%. By applying this method, no prior knowledge of amplitude, slope, or pulse width of the PPG signal is required, thus making it suitable for a diverse range of datasets acquired from different devices.

CHAPTER 5: VALIDATION OF ADAPTIVE TEMPLATE MATCHING ALGORITHM TO DETECT MOTION ARTIFACT FROM PHOTOPLETHYSMOGRAM SIGNALS IN OLDER SUBJECTS

5.1 Introduction

Chapter 4 evaluated the performance of the newly proposed PPG artifact detection algorithm on healthy subjects. In this chapter, the performance of the algorithm was examined on different study cohorts (i.e. older subjects with and without arrhythmia). \

5.2 Literature Review

With an aging population that continues to grow, there is a rising demand for assistive living technologies that could monitor and ensure the wellbeing of older subjects (Poon, Liu, Gao, Lin, & Zhang, 2011). It is beneficial for older patients with chronic diseases to be monitored at home, in terms of vital signs such as HR, BP and SpO_2 level, while performing daily activities. Photoplethysmography serves as a useful tool to effectively monitor these vital signs continuously as it is easy to set up (i.e. requires only a single fingertip sensor), convenient to apply and relatively inexpensive (Hong, Park, & Ahn, 2015; K. Shin et al., 2009)).

Each PPG pulse consists of an incident wave or a systolic phase (which begins from the valley and ends at the peak point forming an upward slope), and a reflected wave or a diastolic phase (which begins from the peak point and ends at the subsequent valley forming a downward slope). The morphology of the PPG signal can be distinguished into five different types according to its changes during the diastolic phase (i.e. the downward slope) (Christoph Fischer, Dömer, Wibmer, & Penzel, 2016; C Fischer et al., 2017).

Generally, PPG signal can be influenced by either intrinsic or extrinsic factors. Intrinsic factors such as age, vessel stiffness, skin condition (properties of skin, skin temperature and skin depth) and respiratory rate could affect the morphology of the PPG signal (Baron, Häbler, Heckmann, & Porschke, 1996; Hong et al., 2015; K. Shin et al., 2009).

Previous studies have demonstrated that the rate of decline of the downward slope (i.e. during the diastolic phase) in the PPG pulse increases with aging and vessel stiffening (J Allen & Murray, 2002; John Allen & Murray, 2003). Apart from that, it has also been postulated that physical and physiological characteristics of respiration affect PPG morphology (through BP and HR): the slower the respiratory rate, the higher the tidal volume (indicated by the amplitude between the valley and the peak point) and the smaller the minute volume (Baron et al., 1996). Disappearance of notch in the diastolic phase of the PPG signal has also been observed in older subjects, and this may be caused by a reduction in systemic vascular compliance due to aging and the existence of cardiovascular complications. On the other hand, extrinsic factors include environmental conditions, sensor fitting method and location, as well as motion artefact (Ricardo Couceiro, Carvalho, Paiva, Henriques, & Muehlsteff, 2012; Hong et al., 2015; H. S. Shin, Lee, & Lee, 2009). In unsupervised environments such as home care setting, motion artefact happens frequently, leading to enormous baseline drift (H. S. Shin et al., 2009) and changes in the morphology of the PPG signal, which subsequently reduce the reliability of PPG-derived parameters (e.g., HR, SpO_2 level and PWV).

To date, most algorithms on motion artefact detection have been developed and validated using data collected from young, healthy subjects. Limited studies have been performed among older subjects, especially those with cardiovascular complications. As aforementioned, PPG morphology differs significantly with aging and in the presence of chronic diseases, therefore algorithms developed based on young subjects may not be applicable on older subjects. Recently, Couceiro et al. (R Couceiro et al., 2014) conducted time and period domain analysis on PPG signals obtained from healthy and cardiovascular disease diseased subjects to detect motion artifact patterns.

In this chapter, the robustness of the artefact detection algorithm developed in Chapter

4 was evaluated on PPG data collected from nineteen older subjects (above 65 years old), with more than half of them having hypertension and cholesterol. In order to control the effect of extrinsic factors, experiments were performed at the same location under a well-controlled environment. Each subject performed a series of movements (i.e. a subset of movements described in Chapter 4 according to the individuals' capabilities) according to the same experimental protocol so that comparison can be done without bias. The performance of the artefact detection algorithm on the older subjects was compared against those obtained from the young subjects.

5.3 Methodology

5.3.1 Subject recruitment and data acquisition

Nineteen subjects aged 65 years and older were recruited for the study. These subjects were either those who have participated in a previous research study conducted in University Malaya Medical Centre (UMMC) or recruited through phone calls and word of mouth. Prior to data acquisition, participant information statement was given to each subject and information concerning the research study was verbally explained by the researcher. Written consent was then obtained from each subject. This study was approved by the medical ethics committee of UMMC (MECID No.: 20151-918). The baseline characteristic and medical history of each subject were recorded as reference for further data processing and analysis.

Data acquisition was conducted at UMMC in a quiet room with well-controlled temperature. A portable and noninvasive physiological signal acquisition device, the Sotera Visi Mobile system (Harvnak) (Sotera Wireless Inc., San Diego, California, USA) was used to collect continuous ECG, PPG and 3D accelerometry signals from the older subjects. The experimental setup of the Sotera Visi Mobile system followed that described in Section 4.2.1 for young subjects.

Table 5.1: List of stationary poses and movements

Types of stationary poses		
Pose	Description	Duration (total)
Sit_S0	Sit stationary on a chair with both arms by sides	5 min
Sit_S1	Sit stationary with both arms crossed across the chest	30 s
Stand_S0	Stand still with both arms by the sides of the body	30 s
Lie_S0	Supine lying with both arms by the sides of the body	30 s
Lie_S1	Lie on the left side of the body with self-selected arm position	30 s
Lie_S2	Lie on the right side of the body with self-selected arm position	30 s
Hand_S0	Place the left arm (the side of the arm with device attached) on the table at sitting position	30 s
Types of movements		
Movement	Description	Duration (median)
Arm_M1	Consecutively lift both arms overhead and back down, five times	15.3
Arm_M2	Consecutively abduct both arms away from midline of the body at 90^{o} and back down, five times	10.3
Arm_M4	Consecutive bend the left thumb, five times	8.1
Arm_M5	Consecutively bend the left elbow, five times	10.3
Arm_M6	Consecutively swing the arm left and right, five times	13.5
Arm_M7	Eat food from a plastic packet	$\geq$ 60 s
Arm_M8	Flip through pages of a book	60 s
Body_M0	Consecutively sit-to-stand with both arms by sides, five times	12.1
Body_M1	Consecutively twist the body from side to side at standing position, five times	12.7
Body_M2	Sit-to-lie-to-sit with pauses in between, five times	43.3
Body_M3	Walk at normal speed (for around 50 m)	37.5
Body_M4	Walk up the stairs with ten steps	15
Body_M5	Walk down the stairs with ten steps	9.2
Body_M6	Pick up a pen from the floor with left hand	6.1

Prior to the start of the experiment, each subject rested in a sitting position for at least five minutes to stabilize their heart rate and BP readings. Subjects were instructed to perform a predefined set of poses and movements, as listed in Table 5.1. Certain poses and movements performed by the young subjects (as described in Section 4.1) were excluded as they were too challenging for older subjects and not usually encountered in daily life. During stationary poses, subjects were reminded not to move any parts of their

body as well as fingers in order to minimize the occurrence of motion artifacts. On the other hand, each movement was performed naturally instead of adhering to a predefined movement speed. Subjects were required to raise their left arm three times between successive movements poses.

5.3.2 Signals evaluation by clinical experts

Two clinical experts were individually presented with a custom-designed MATLAB graphical user interface (GUI) software tool, displaying the physiological signals (ECG, PPG and accelerometry signals) collected from the older subjects. By observing the PPG morphology with the assistance of concurrent ECG and accelerometry signals, the clinical experts classified each PPG pulse into either clean or artifact. Any disagreements on the annotation were brought into discussion to produce the final annotation result, which were subsequently used as the gold standard for validation. In the evaluation of the algorithm, only the PPG signal was used.

5.3.3 Algorithm Implementation

The algorithm developed in Chapter 4 were implemented on PPG signal collected from the older subjects. Two models with different threshold values (*Th*) and learning rates (α) were applied. Model 1 adopted the optimized threshold value (*Th*) (0.91) and learning rate (α) (0.93) for the young subjects, while new threshold value (*Th*) and learning rate (α) were selected for Model 2 by applying the same training and testing method described in Chapter 4 on data collected from the older subjects.

5.4 Results

Nineteen older subjects (6 male, 13 female) with a mean age of 73 years and a standard

deviation of 5 years were recruited between the periods of August 2018 - September 2018. More than half of these subjects had hypertension (11 subjects) and high cholesterol (14 subjects). Five subjects showed ECG segments with irregular rhythm throughout the experiment procedure, but only one of them had been diagnosed and treated for arrhythmia.

5.4.1 PPG waveform morphology

Fig. 5.1(a) and (b) shows two examples of PPG signal obtained from a young subject and an older subject, respectively. It can be observed that unlike the young subject, there is no evidence of a notch or changes in the angle descent in the downward slope of the PPG pulses acquired from the older subject. This alternative PPG morphology was one of the five types of PPG morphology recently described by Fischer et al. in their published finding (C Fischer et al., 2017).

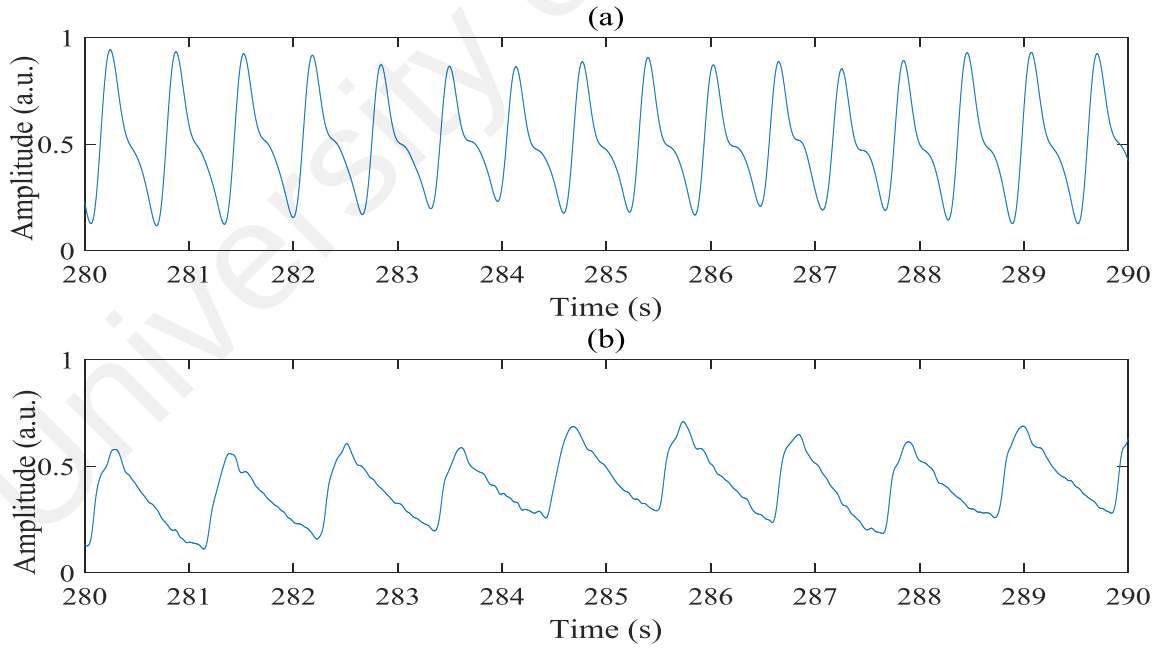

Figure 5.1: Normalized PPG waveform from (a) a young subject; and (b) an older subject.

Fig. 5.2(a) and (b) shows an example of a normal ECG waveform and a clean PPG waveform from an older subject. It can be observed from the ECG waveform that the

patient had regular heart rhythms and consistent PPG morphology across pulses.

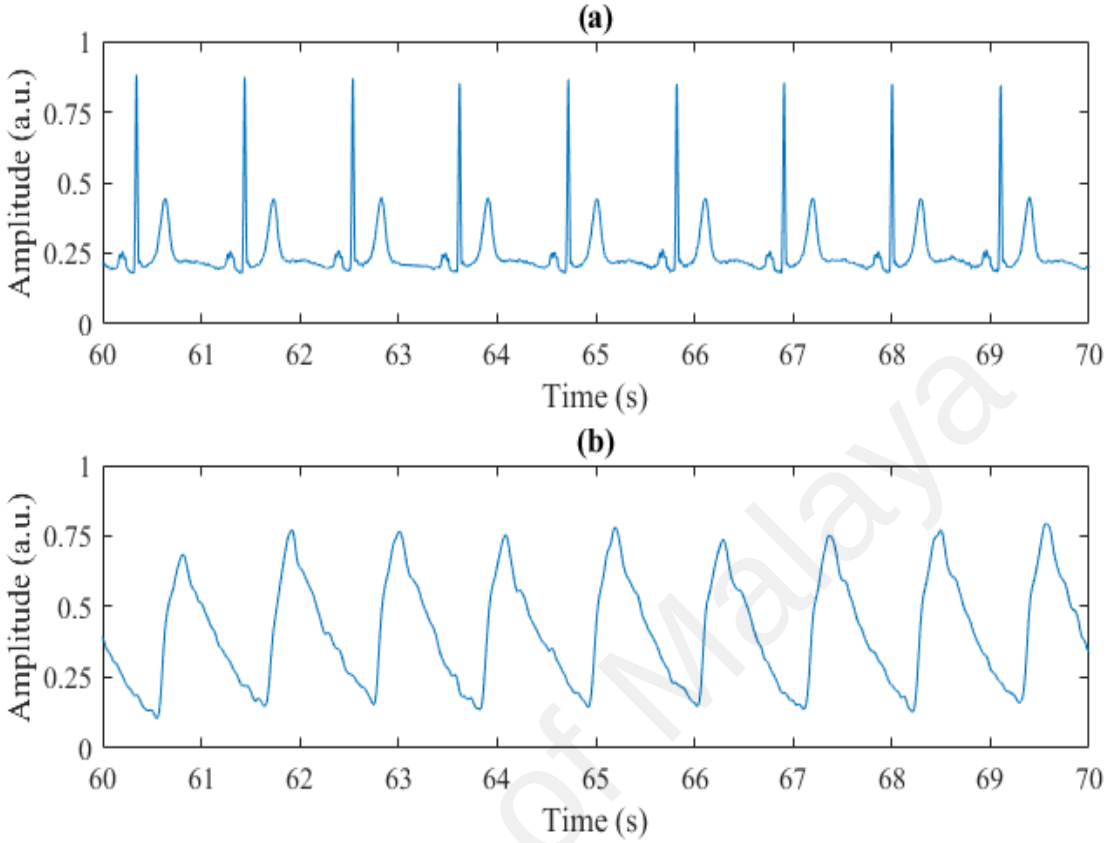

Figure 5.2: Example of (a) a normal ECG waveform and (b) a normal, clean PPG waveform from an older subject.

Fig. 5.3 (a) and (b) shows an example of an irregular ECG waveform and a PPG waveform with bad pulses (according to clinical expert annotation results) from an older subject. It can be observed from the ECG waveform that the patient had irregular heart rhythms (between 882 s and 886 s). This led to inconsistent PPG morphology during this time period, which was subsequently labelled by the clinical expert as bad pulses.

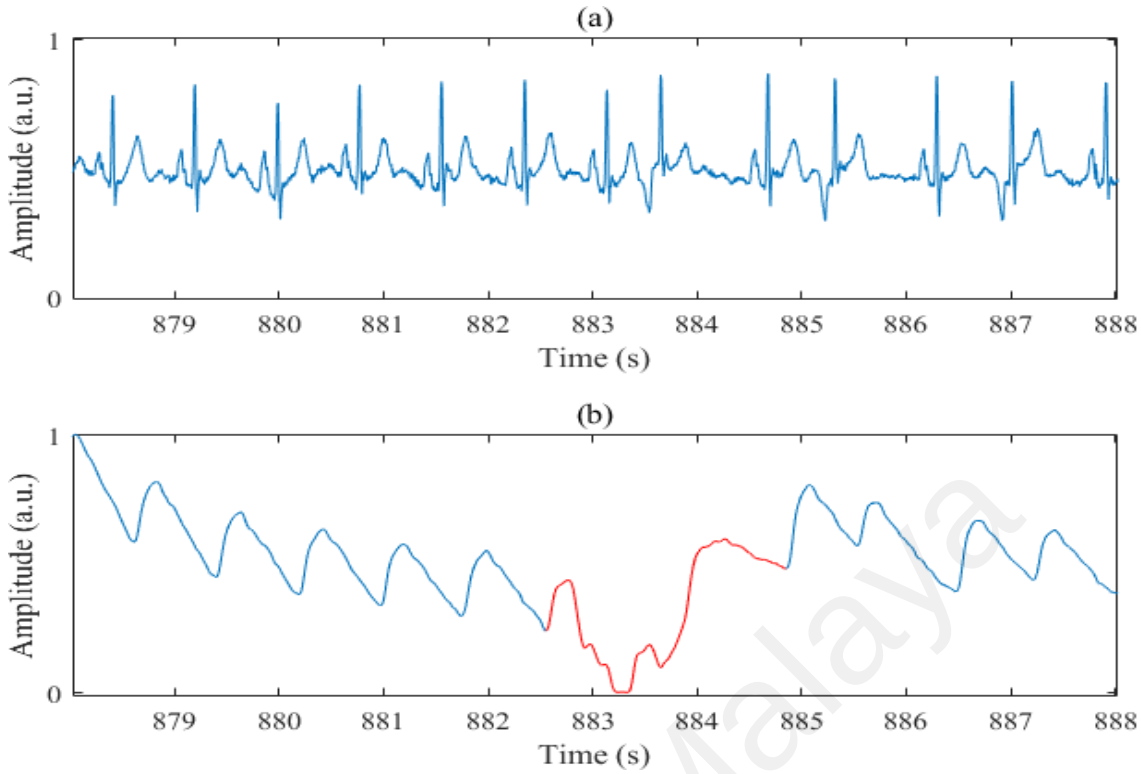

Figure 5.3: Example of (a) an irregular ECG waveform and (b) a PPG waveform with bad pulses (red segment, according to clinical expert annotation results) from an older subject.

Fig. 5.4 (a) and (b) shows an example of an irregular ECG waveform and a clean PPG waveform (according to clinical expert annotation results) with inconsistent morphology (between 220 s and 224.5 s) from an older subject. It can be observed from the ECG waveform that the patient had irregular heart rhythms (between 220 s and 224.5 s), which led to inconsistent PPG morphology during this time period. Despite inconsistent morphology, the PPG pulses were labelled as clean by the clinical experts as they not only resembled characteristic PPG morphology, each of the PPG pulse corresponded to one ECG pulse, thus can be regarded as true pulses.

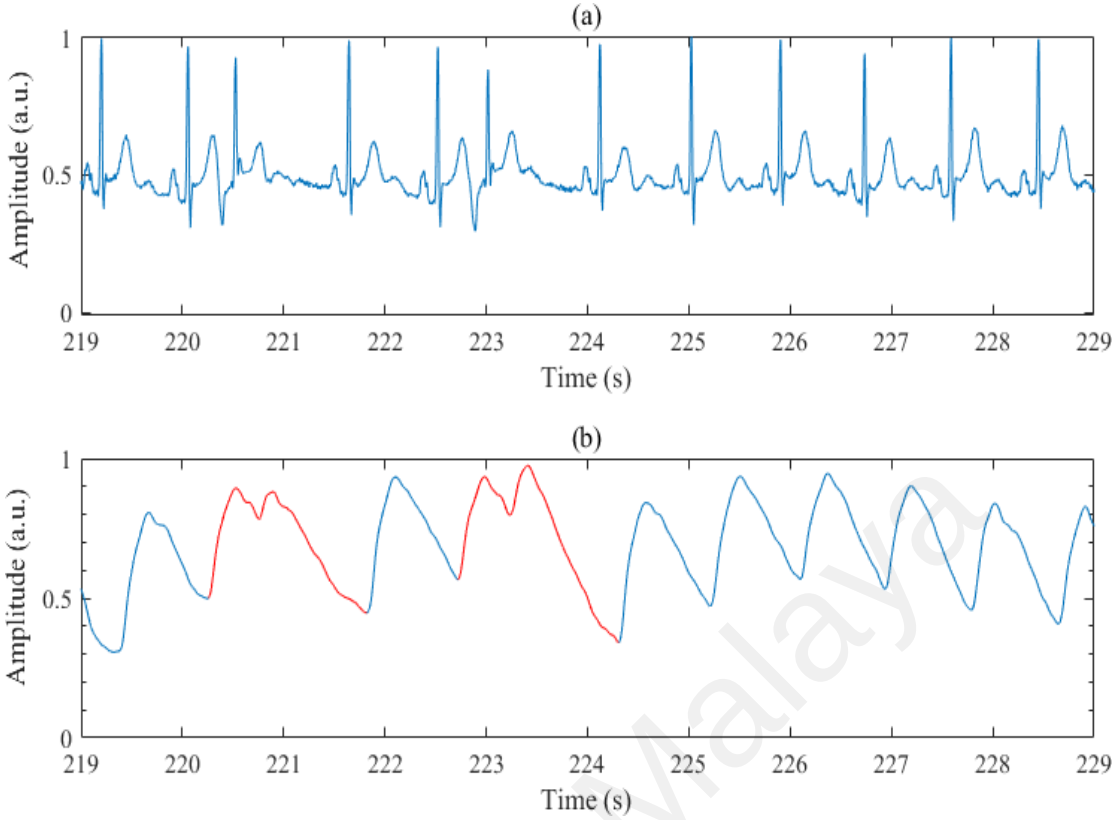

Figure 5.4: Example of (a) an irregular ECG waveform and (b) a clean PPG waveform (according to clinical expert annotation results) with inconsistent morphology (red segment) from an older subject.

5.4.2 Optimization of the learning rate (*α*) and correlation threshold values (*Th*)

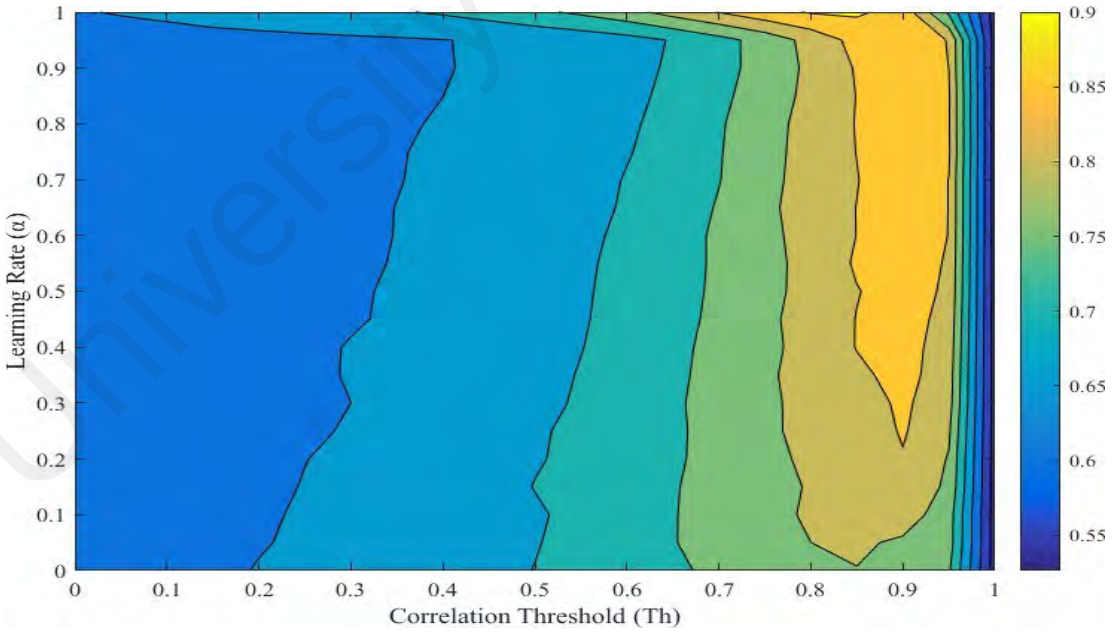

Figure 5.5: Contour plot of the classification accuracy with respect to correlation threshold (*Th*) value and learning rate (α) (search step size = 0.05). Color bar on the right indicates the accuracy scale. A learning rate of α = 1.0 with a correlation threshold value (*Th*) of 0.85 yielded the highest accuracy (90.1%) with a sensitivity of 83.4% and a specificity of 91.1%.

As shown in Figure 5.5, by varying the learning rate (α) and correlation threshold values (*Th*) from 0 to 1 with a step size of 0.05 on the training data, we found that region with a learning rate (*α*) of 1.0 and a correlation threshold value (*Th*) of 0.85 yielded the highest accuracy. The classification accuracy was further calculated with a finer size of 0.01 for both learning rate (*α*) (within the range 0.90 to 1.00) and correlation threshold value (*Th*) (within the range 0.85 to 0.95). The optimized learning rate (*α*) and correlation threshold (*Th*) value were 0.99 and 0.89. By using these optimization values, our algorithm was able to achieve an overall accuracy of 90.2±4.6% (median = 90.7%, interquartile range = 3.7%) with a sensitivity of 80.7±13.5% (median = 83.8%, interquartile range = 12.5%) and a specificity 93.3±9.3% (median = 95.4%, interquartile range = 3.5%).

5.4.3 Effect of varying the correlation threshold value (Th)

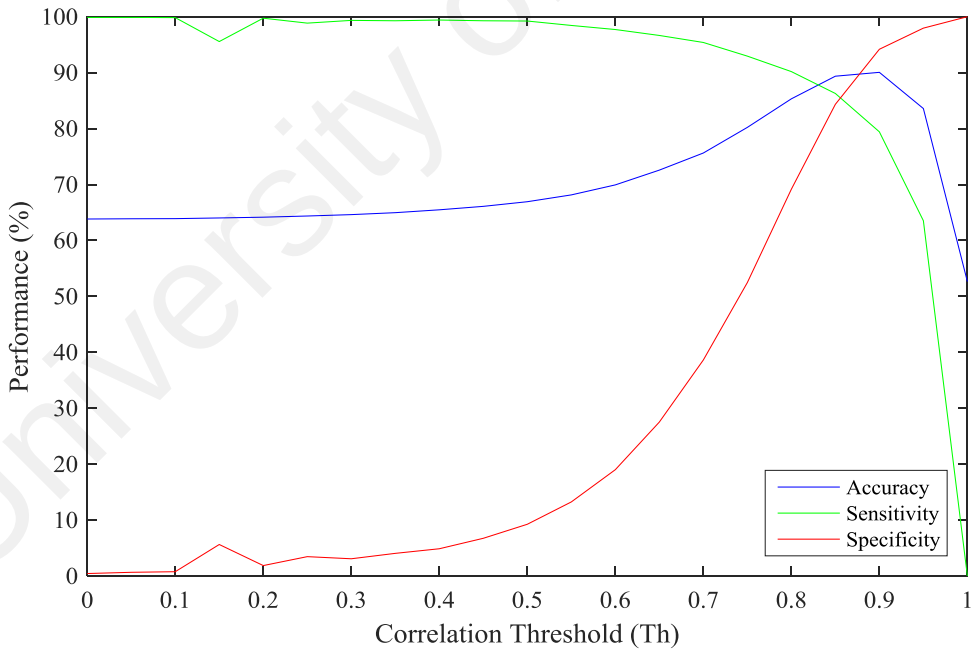

Figure 5.6: Classification results with varying correlation threshold (Th) values at a fixed learning rate (α) of 0.99.

Figure 5.6 demonstrates the effect of changing the correlation threshold (*Th*) with a step size of 0.05, on the classification accuracy, sensitivity, and specificity, at a learning rate (α) of 0.99.At low correlation threshold (*Th*) values, almost all pulses

were classified as good (accuracy: 63.8%; sensitivity: 99.9%; specificity: 0.4%, with a correlation threshold (*Th*) value of 0).With an increase in the correlation threshold (*Th*) value above 0.6, both the accuracy and specificity levels showed a steep increase, at the expense of a slight drop in the sensitivity (accuracy: 69.9; sensitivity: 97.7; specificity: 19.0with a correlation threshold (*Th*) value of 0.6). The highest accuracy was achieved when the correlation threshold (*Th*) value reached 0.90 with an accuracy of 89.9, sensitivity of 79.4 and specificity of 94.3 respectively.

5.4.4 Effect of varying the learning rate (α)

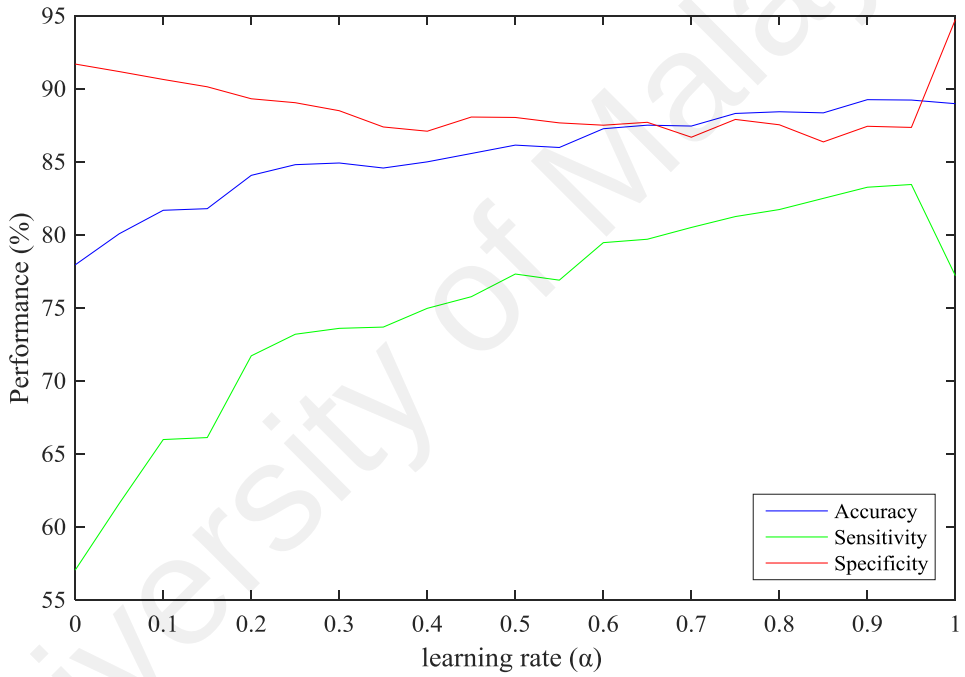

Figure 5.7: Classification results with varying learning rate (α) values at a fixed correlation threshold (Th) of 0.89.

Figure 5.7 demonstrates the effect of changing the learning rate (α) with a step size of 0.05, on the classification accuracy, sensitivity, and specificity, at a correlation threshold (*Th*) of 0.89. At low learning rate, almost all the artifact pulses were classified correctly (accuracy: 77.6%; sensitivity: 57.04%; specificity: 91.8%, with a learning rate (α) of 0).

The accuracy of the algorithm improved by increasing the learning rate (α). The highest accuracy was achieved when the learning rate (α) reached 0.95, with accuracy

of 89.0%, sensitivity of 83.3% and specificity of 87.8%, respectively.

5.4.5 Comparison between different sets of parameters optimized using young and older subjects' data

Table 5.2 shows a comparison between two models: (i) model 1 with a threshold value (*Th*) of 0.91 and a learning rate (α) of 0.93, adopted from Chapter 4 on young subjects; and (ii) model 2 with the new optimized threshold value (*Th*) and learning rate (α) for older subjects. Both models achieved similar results with regards to accuracy, sensitivity, specificity, positive predictive value and negative predictive value, with model 2 performing approximately 1% better than model 1 in all performance categories. In addition to the performance measures presented in Chapter 4, Table 5.2 also included the positive predictive value (PPV) and negative predictive value (NPV). PPV refers to the percentage of clean PPG signals identified correctly as good pulses from the total number of good pulses detected, while NPV refers to the percentage of corrupted PPG signals identified correctly as bad pulses from the total number of bad pulses detected. Both models showed high PPV, with 91.8% for model 1 and 93.2% for model 2. As compared to patients with regular ECG rhythm, it can be demonstrated that the presence of irregular ECG rhythm substantially reduced the accuracy, sensitivity and NPV (by around 3%), while specificity and PPV remained relatively unchanged or showed a minor increase.

Table 5.2: Comparison between two models: (i) model 1 with a threshold value (*Th*) of 0.91 and a learning rate (α) of 0.93, adopted from Chapter 4 on young subjects; and (ii) model 2 with the new optimized threshold value (*Th*) and learning rate (α) for older subjects on accuracy, sensitivity, specificity, positive predictive value and negative predictive value.

Performance measures	Model 1			Model 2		
	Regular ECG rhythm (N=14)	Irregular ECG rhythm (N=5)	Total (N=19)	Regular ECGrhythm (N=14)	Irregular ECG rhythm (N=5)	Total (N=19)
Accuracy (%)	90.6±4.0	85.3±4.1	89.2±4.6	91.3±3.6	87.0±5.9	90.2±4.6
Sensitivity (%)	79.5±16.4	80.1±9.0	79.6±14.5	80.5±15.0	81.4±9.6	80.7±13.5
Specificity (%)	92.2±10.7	91.6±4.1	92.0±9.3	93.0±10.8	94.1±2.6	93.3±9.3
Positive Predictive Value (%)	91.8±11.4	93.9±1.9	92.4±9.8	93.2±10.2	95.9±0.6	93.9±8.8
Negative Predictive Value (%)	79.5±14.3	75.8±11.0	78.5±13.3	80.2±13.9	77.2±12.5	79.4±13.3

5.4.6 Comparison of the algorithm performance between young and older subjects

Table 5.3: PPG pulse quality classification results for stationary poses (mean ±SD) on the young and older subjects.

Stationary Poses	Young subjects (N =19)			Older subjects (N =19)		
	Accuracy (%)	Sensitivity (%)	Specificity (%)	Accuracy (%)	Sensitivity (%)	Specificity (%)
Sit_S0	87.0 ± 8.1	88.5 ± 7.9	81.1± 15.1	90.6±7.0	87.5±9.5	91.8±16.7
Sit_S1	89.5 ± 15.2	95.9 ±2.2	86.2± 18.7	91.4±6.9	84.9±14.2	96.2±7.7
Stand_S0	86.4 ± 20.3	88.3 ± 14.3	85.9±17.9	87.6±9.3	80.2±15.4	93.4±12.3
Lie_S0	95.8 ± 4.9	96.4 ±2.5	85.4±18.6	91.1±7.8	79.2±14.9	96.0±6.3
Lie_S1	89.0 ± 3.5	93.3±2.6	85.4±20.4	86.2±9.1	77.0±17.6	90.6±19.5
Lie_S3	94.3 ± 8.1	98.4± 3.8	66.7±22.4	91.1±8.6	82.8±11.6	97.4±4.6
Hand_S0	93.8 ± 6.2	96.1± 7.5	75.9± 21.7	90.8±6.6	79.0±15.6	95.2±5.0
Average	90.8±3.8	93.8±4.0	80.9±7.3	89.8±2.1	81.5±3.7	94.4±2.5

Tables 5.3 and 5.4 show the mean classification results for stationary poses and movements on the young and older subjects. Compared to the young subjects, a reduction in the overall accuracy was observed in the older subjects for both stationary poses and movements. Meanwhile, the sensitivity also dropped drastically in the older subjects for all types of stationary poses and movements. On the contrary, the older subjects demonstrated a major increase in the specificity results for stationary poses, but with relatively unchanged performance for movements.

Table 5.4: PPG pulse quality classification results for movements (mean ±SD) on the young and older subjects.

Movements	Young subjects (N = 19)			Older subjects (N = 19)		
	Accuracy (%)	Sensitivity (%)	Specificity (%)	Accuracy (%)	Sensitivity (%)	Specificity (%)
Arm_M1	97.0 ± 4.5	78.9 ± 0.0	98.0 ± 4.5	88.4±10.1	71.3±17.4	93.5±5.0
Arm_M2	99.2 ± 2.6	80.5 ± 13.4	100 ± 0.0	87.4±10.0	83.4±12.2	92.8±16.4
Arm_M4	88.3 ± 0.0	89.4 ± 0.0	86.0 ± 18.8	93.0±7.5	91.1±10.7	94.9±12.7
Arm_M5	97.0 ± 7.0	78.9 ± 0.0	97.5 ± 7.0	93.6±5.5	86.2±10.8	95.5±7.7
Arm_M6	91.1 ± 9.1	83.3 ± 0.0	92.3 ± 12.5	94.7±7.3	91.4±11.8	99.5±2.0
Arm_M7	87.3 ± 6.5	89.8 ± 9.7	86.7 ± 7.6	94.3±6.3	80.7±27.0	97.8±5.5
Arm_M8	93.5 ± 5.3	95.8 ± 5.9	91.1 ± 5.3	92.1±7.2	80.7±19.5	93.8±8.3
Body_M0	94.4 ± 5.8	72.7 ± 14.2	95.6 ± 3.7	89.2±9.3	82.3±18.8	89.7±14.0
Body_M1	97.9 ± 3.7	79.4 ± 13.8	98.7 ± 3.5	90.3±4.4	78.8±10.4	94.1±4.4
Body_M2	88.1 ± 12.9	80.8 ± 10.9	88.4 ± 12.9	93.8±4.8	79.0±18.6	95.4±4.9
Body_M3	99.3 ± 1.2	77.6 ± 6.5	99.5 ± 8.9	90.6±7.8	76.5±22.3	93.2±6.2
Body_M4	95.9 ± 3.1	98.9 ± 1.2	93.7 ± 3.1	85.4±15.5	71.4±26.7	90.5±18.4
Body_M5	97.2 ± 6.1	78.1 ± 4.1	97.9 ± 5.5	87.0±14.0	75.4±23.5	91.2±12.1
Body_M6	92.9 ± 12.1	83.9 ± 0.0	93.1 ± 12.2	83.4±17.9	68.9±28.0	97.4±6.0
Average	94.2±4.1	83.4±7.7	94.3±4.9	90.2±3.6	79.8±6.9	94.2±3.1

Table 5.5 shows the statistical analysis results of the algorithm performance in terms of average accuracy. For stationary poses, the difference in the average accuracy between the two groups was not statistically different (p-value > 0.05), i.e. 92.1% for young subjects and 89.8% for older subjects. However, for movements, the algorithm performed better when applied on data collected from the young subjects (average accuracy of 94.6%) as compared to the older subjects (average accuracy of 90.2 %), with a p-value <0.001.

Table 5.5: Statistical analysis results comparing the algorithm performance between young and older subjects in terms of average accuracy (mean ± SD).

	Young adults (N=19)	Older adults (N=19)	p-value
Stationary poses (%)	90.8 ± 3.8	89.8 ± 2.1	0.107
Movements (%)	94.2 ± 4.1	90.2 ± 3.6	<0.001

5.4.7 Comparison of the algorithm performance between older subjects with and without irregular heart rhythms

The performance of the algorithm on five older subjects with irregular heart rhythms was compared with the rest of the older subjects (N=14) with normal sinus rhythm. As shown in Table 5.6, the algorithm performed slightly better in older subjects with normal sinus rhythm, for both stationary poses and movements. In

terms of stationary poses, a 4.4% reduction in both accuracy and specificity were obtained when tested on older subjects with irregular heart rhythm. Meanwhile, as compared to those with normal sinus rhythm, a minor increase in sensitivity (of 1.1%) was achieved in older subjects with irregular heart rhythm. Similar observations were found for movements with regards to the average accuracy (a 3% drop in older subjects with irregular heart rhythm), but opposite results were demonstrated in sensitivity/specificity. Instead of showing an increase in sensitivity and a reduction in specificity, older subjects with irregular heart rhythm had a reduction in sensitivity (2.4%) and relatively unchanged specificity when compared to those with normal sinus rhythm.

Table 5.6: Comparison of the algorithm performance between older subjects with and without irregular heart rhythms.

	Older subjects with normal sinus rhythm (N=14)			Older subjects with irregular heart rhythm (N=5)		
	Accuracy (%)	Sensitivity (%)	Specificity (%)	Accuracy (%)	Sensitivity (%)	Specificity (%)
Stationary poses	91.0±3.0	81.2±5.6	95.6±2.7	86.6±1.8	82.3±6.3	91.2±5.9
Movements	91.0±3.8	80.5±7.9	94.3±3.3	88.0±4.2	78.1±8.3	94.2±4.4

5.4 Discussion

The present study evaluates the robustness of the previously developed artefact detection algorithm on PPG signals collected from young subjects, older subjects with normal sinus rhythm as well as those with irregular heart rhythms. The morphology of the PPG signal varies from an individual to another due to various phenomena and can be classified into five different categories according to its changes during the diastolic phase: (i) two distinct notches are inscribed on the downward slope; (ii) one distinct notch is inscribed; (iii) no notch develops but the line of descent becomes horizontal. (iv) no notch is present but well-defined change in the angle of descent is observed; (v) no evidence of a notch is seen (Christoph Fischer et al., 2016). Based on PPG signals obtained in this study, it was observed that types 1-3 were commonly found in the young subjects, while types 4-5 were observed in the older subjects

(Figures 5.1& 5.2). Older subjects normally experience a reduction in the systemic vascular compliance due to ageing, which leads to the disappearance of the dicrotic notch. In addition, some of them had cardiovascular diseases that alter the morphology of the PPG signal. The variations in the PPG morphology across different cohorts present a challenge for designing a robust algorithm that could detect clean PPG signals in all cohorts.

The present algorithm was able to achieve high accuracies on both young and older subject's data (i.e., above 90%). By using the optimized parameter values trained with young subject's data (i.e., Model 1) on PPG signals collected from older subjects, comparable performance with only a minor reduction in accuracy was obtained (Table 5.2). This demonstrated the robustness of our algorithm against variations in subjects and further highlighted its simplicity, which only requires the selection of two variables. While young subjects demonstrated significantly lower specificities for stationary poses as compared to movements and vice versa for sensitivities, the types of activities (stationary poses or movements) have negligible effects on the performance measures in older subjects (Tables 5.3 – 5.5). Overall, the algorithm performed worse when applied on data collected from the older subjects as compared to the young subjects especially for movements. This could be due to the presence of a large variation in PPG morphology across older subjects, for example due to irregular heart rhythms. The presence of abnormal cardiovascular events such as arrhythmia could alter the periodic characteristics of the PPG signal, which may lead to misclassifications of clean PPG signals (R Couceiro et al., 2014). As a result, the algorithm performed slightly better in older subjects with normal sinus rhythm as compared to those with irregular heart rhythms, for both stationary poses and movements (Table 5.6).

To date, only a single study has (R Couceiro et al., 2014) developed and validated

their motion artifact detection algorithms on PPG signals obtained from both healthy subjects and patients with cardiovascular disease. Time and period domain analysis were conducted on PPG signals collected from seven older patients (mean age of 62 years). Eight most relevant features (i.e. four features from the time domain and four features from the period domain) were chosen as input to the support vector machine (SVM) model for further classification. As compared to Couceiro et al., the present study achieved a higher accuracy (90.2% vs. 88.5%) and specificity (93.3% vs. 91.5%), but at the expense of a lower sensitivity (80.7% vs 84.3 %). As PPG morphology changes with time, the present algorithm, which updated the master templates with each incoming good pulse, is more robust to variations across subjects and within an individual.

5.5 Conclusion

In this chapter, the motion artifact detection algorithm developed in the Chapter 4 was evaluated on older subjects with normal sinus rhythm and irregular heart rhythm. Despite changes in PPG signal morphology due to the presence of irregular heart rhythms, the present algorithm was able to achieve an accuracy of over 87% on these subjects as compare to healthy young subject.

CHAPTER 6: CONCLUSION AND RECOMMENDATIONS

The main idea of this thesis is to develop an automatic artifact detection algorithm to classify BP and PPG signals, especially in the occurrence of motion artifacts. The developed algorithms have been evaluated on several sources of data, including a publicly available ICU database (PhysioNet), healthy patients, older patients and arrhythmia patients. This chapter summarises the overall conclusion and major contributions of the research. Besides that, recommendations and future work are also presented.

6.1 Summary and Conclusion

This thesis has introduced a novel technique to identify artifacts and estimate BP based on motion corrupted oscillometric BP measurements. An automatic algorithm based on changes in the oscillometric pulses relative to their respective neighbour pulses was proposed to remove outlier points before the curve fitting process. Ten features extracted from the OWE corresponding to systolic (SBPR) and diastolic blood pressure ratio (DBPR) were evaluated. Our results showed that both SVR and MLR models achieved a comparable performance. However, MLR model is preferable due to its simplicity.

Other than that, an adaptive algorithm has been developed to detect artifacts in PPG signals. There are several strengths of the designed adaptive algorithm. Firstly, this algorithm does not required any prior knowledge of the PPG signal such as amplitude, pulse width and slope, thus our algorithm is suitable for a diverse range of datasets acquired from different devices. Besides that, two standard PPG master templates were generated; thus eliminating the need to generate subject-specific templates to account for inherent differences in the PPG waveform morphology across subjects, which resulted in long processing time. Moreover, our algorithms required a shorter response time (i.e. 2s); thus make it suitable for online detection purpose (within 2s). This algorithm has been tested on ambulatory long-continuous data (i.e. longer than 30mins) which contained several types of motion and short segment data (6s) in the ICU environment. Our

algorithm achieved accuracy of more than 95% for both databases.

Older and chronic disease patients have shown significant difference in PPG morphology compared to normal healthy subjects. Therefore, the developed algorithm based on young subjects in Chapter 4 was validated on these groups of patients. In general, the performance of the developed algorithm achieved accuracy of around 90%. The results of the older patients found no significant difference when compared with healthy young subjects. This has proven the robustness of our algorithm.

To conclude, the signal quality of physiological signals play an important role in clinical diagnosis. When telehealth recording was performed by the patient without supervision, the noise level can be greatly increased due to movement and poor recording technique. By using the developed signal quality algorithms as described in this thesis, the corrupted signal can be eliminated and excluded from further analysis. This can improve the reliability of the telehealth and improve the health care provision for different cohorts of patients.

6.2 Recommendation for future studies

The present study proposed a BP estimation algorithm but only considering healthy subjects. Although promising results were shown, the effectiveness of the algorithm on different cohorts of patients remains unknown. Moreover, some studies show that BP estimation was unreliable in certain populations such as patients with obesity (Umana et al., 2006), arterial stiffness (van Popele et al., 2000), and atrial fibrillation (Pagonas et al., 2013; Verberk & De Leeuw, 2012). In addition, this study only acquired data from 20 healthy subjects. The AAMI standard requires 255 measurements to be recorded in at least 85 subjects, with at most three measurements per subject for a validation study. Hence, validation of the developed algorithms on these patients would be crucial.

As explained in Chapter 4.2.3, the developed PPG artifact detection algorithms

required a pulse segmentation pre-processing step where having pulse segmentation as a pre-task for motion artifact detection is a drawback of the current algorithm. If we segment the pulse wrongly, it will also lead to wrong classification results and affect the performance. To the best of our knowledge, to date, except for Dao *et al*. (Dao et al., 2016), beat detection has been an a priori step in most artifact detection work on PPG signals (Chong et al., 2014; R Couceiro et al., 2014; Q. Li & G. D. Clifford, 2012; Orphanidou et al., 2014; Selvaraj et al., 2008; J Abdul Sukor et al., 2011; X. Sun et al., 2012). This algorithm can be further enhanced by eliminating this step. In addition, the parameter tuning process involved searching through all possible combinations of learning rate and correlation threshold to find the best parameters which yield the most optimal performance in terms of accuracy. Future study should employ a more principled method, such as the DOE (design-of-experiment) method, which is more computationally effective.

Although promising results were shown, the PPG algorithm was only tested on a small number of older subjects with arrhythmia (N=5). Furthermore, the effectiveness of the algorithm on different patient cohorts, such as atrial fibrillation, ventricular arrhythmia, ventricular fibrillation and ventricular tachycardia remain unknown.

In addition, this thesis studied PPG signals collected from a single sensor that is attached to the left thumb. However, a single sensor may have distinct disadvantages when applying to unsupervised monitoring. Any loss of contact or dysfunctionality of the sensor will lead to loss of signal monitoring. Therefore, it is suggested that the study can collect the PPG signals with multiple sensors at multiple body locations, such as the forehead and earlobe. This allows the comparison of the collected PPG signals and then provides a better accuracy of the application of PPG signals in SpO_2 estimation etc. Other than that, since the human body is a complex integration of numerous physiological

systems, it allows collection of multiple physiological signals simultaneously. Moreover, these physiological signals can be inter-correlated with one another; for example, ECG and PPG signals. Thus, future study could collect multiple different physiological signals, and then by the fusion of these signals, the study will be able to provide better health condition estimation.

REFERENCE

Abay, T. Y., & Kyriacou, P. A. (2018). Photoplethysmography for blood volumes and oxygenation changes during intermittent vascular occlusions. *Journal of clinical monitoring and computing, 32*(3), 447-455.

Abolarin, D., Forouzanfar, M., Groza, V., Rajan, S., Dajani, H., & Petriu, E. (2016). *Model-based filtering and compression of oscillometric blood pressure pulses*. Paper presented at the IEEE International Symposium on Medical Measurements and Applications (MeMeA).

Aboukhalil, A., Nielsen, L., Saeed, M., Mark, R. G., & Clifford, G. D. (2008). Reducing false alarm rates for critical arrhythmias using the arterial blood pressure waveform. *J Biomed Inform, 41*(3), 442-451.

Addison, P. S. (2017). Respiratory effort from the photoplethysmogram. *Medical engineering & physics, 41*, 9-18.

Addison, P. S., & Watson, J. N. (2004). Secondary transform decoupling of shifted nonstationary signal modulation components: application to photoplethysmography. *International Journal of Wavelets, Multiresolution and Information Processing, 2*(01), 43-57.

Ahmad, S., Chen, S., Soueidan, K., Batkin, I., Bolic, M., Dajani, H., & Groza, V. (2012). Electrocardiogram-assisted blood pressure estimation. *IEEE Transactions on Biomedical Engineering, 59*(3), 608-618.

Allen, J., & Murray, A. (1996). Assessing ECG signal quality on a coronary care unit. *Physiol Meas, 17*(4), 249.

Allen, J., & Murray, A. (1999). Modelling the relationship between peripheral blood pressure and blood volume pulses using linear and neural network system identification techniques. *Physiol Meas, 20*(3), 287.

Allen, J., & Murray, A. (2002). Age-related changes in peripheral pulse timing characteristics at the ears, fingers and toes. *Journal of human hypertension, 16*(10), 711-717.

Allen, J., & Murray, A. (2003). Age-related changes in the characteristics of the photoplethysmographic pulse shape at various body sites. *Physiol Meas, 24*(2), 297.

Allen, R. a., Schneider, J. A., Davidson, D. M., Winchester, M. A., & Taylor, C. B. (1981). The covariation of blood pressure and pulse transit time in hypertensive patients. *Psychophysiology, 18*(3), 301-306.

Antonova, M. L. (2013). Noninvasive determination of arterial elasticity and blood pressure. Part I: arterial volume pulsations and elastogram. *Blood pressure monitoring, 18*(1), 32-40.

Anzanpour, A., Azimi, I., Götzinger, M., Rahmani, A. M., TaheriNejad, N., Liljeberg, P., . . . Dutt, N. (2017). *Self-awareness in remote health monitoring systems using wearable electronics.* Paper presented at the Design, Automation & Test in Europe Conference & Exhibition.

Askarian, B., Jung, K., & Chong, J. W. (2019). Monitoring of Heart Rate from Photoplethysmographic Signals Using a Samsung Galaxy Note8 in Underwater Environments. *Sensors, 19*(13), 2846.

Ave, A., Fauzan, H., Adhitya, S. R., & Zakaria, H. (2015). *Early detection of cardiovascular disease with photoplethysmogram (PPG) sensor*. Paper presented at the International Conference on Electrical Engineering and Informatics (ICEEI).

Babbs, C. F. (2012). Oscillometric measurement of systolic and diastolic blood pressures validated in a physiologic mathematical model. *Biomedical engineering online, 11*(1), 56.

Baker, P., Westenskow, D., & Kück, K. (1997). Theoretical analysis of non-invasive oscillometric maximum amplitude algorithm for estimating mean blood pressure. *Medical and biological engineering and computing, 35*(3), 271-278.

Baker, P. D., Orr, J. A., Westenskow, D. R., & Egbert, T. P. (1994). U.S. Patent No. 5339818.

Barbé, K., Kurylyak, Y., & Lamonaca, F. (2014). Logistic ordinal regression for the calibration of oscillometric blood pressure monitors. *Biomedical Signal Processing and Control, 11*, 89-96.

Barbé, K., Van Moer, W., & Lauwers, L. (2010). *Oscillometric blood pressure measurements: A signal analysis.* Paper presented at the Journal of Physics: Conference Series.

Barbe, K., Van Moer, W., & Schoors, D. (2011). Analyzing the windkessel model as a potential candidate for correcting oscillometric blood-pressure measurements. *IEEE Transactions on Instrumentation and Measurement, 61*(2), 411-418.

Baron, R., Häbler, H.-J., Heckmann, K., & Porschke, H. (1996). Respiratory modulation of blood flow in normal and sympathectomized skin in humans. *Journal of the autonomic nervous system, 60*(3), 147-153.

Basak, D., Pal, S., & Patranabis, D. (2007). Support Vector Regression. *Neural Information Processing – Letters and Reviews, 11*.

Bashar, S. K., Han, D., Soni, A., McManus, D. D., & Chon, K. H. (2018). *Developing a novel noise artifact detection algorithm for smartphone PPG signals: Preliminary results.* Paper presented at the IEEE EMBS International Conference on Biomedical & Health Informatics (BHI).

Beevers, G., Lip, G. Y., & O'Brien, E. (2001). ABC of hypertension: Blood pressure measurement. Part II-conventional sphygmomanometry: technique of auscultatory blood pressure measurement. *Bmj, 322*(7293), 1043-1047.

Benoit, H., Costes, F., Feasson, L., Lacour, J., Roche, F., Denis, C., . . . Barthelemy, J. (1997). Accuracy of pulse oximetry during intense exercise under severe hypoxic conditions. *European journal of applied physiology and occupational physiology, 76*(3), 260-263.

Bowles, K. H., & Baugh, A. C. (2007). Applying research evidence to optimize telehomecare. *The Journal of cardiovascular nursing, 22*(1), 5.

Budidha, K., & Kyriacou, P. (2014). The human ear canal: investigation of its suitability for monitoring photoplethysmographs and arterial oxygen saturation. *Physiol Meas, 35*(2), 111.

Burke, M. (2018). *Haptic Feedback for VR Environments, Electrical and Electronic Engineering.*

Casson, A. J., Vazquez Galvez, A., & Jarchi, D. (2016). Gyroscope vs. accelerometer measurements of motion from wrist PPG during physical exercise. *ICT Express, 2*(4), 175-179.

Cattivelli, F. S., & Garudadri, H. (2009). *Noninvasive cuffless estimation of blood pressure from pulse arrival time and heart rate with adaptive calibration.* Paper presented at the Sixth international workshop on wearable and implantable body sensor networks.

Celka, P., Verjus, C., Vetter, R., Renevey, P., & Neuman, V. (2004). Motion resistant earphone located infrared based heart rate measurement device. *Biomedical Engineering*.

Celler, B. G., Argha, A., Le, P. N., & Ambikairajah, E. (2018). Novel methods of testing and calibration of oscillometric blood pressure monitors. *PloS one, 13*(8).

Chambrin, M.-C. (2001). Alarms in the intensive care unit: how can the number of false alarms be reduced? *Critical Care, 5*(4), 184.

Chan, G. S., Fazalbhoy, A., Birznieks, I., Macefield, V. G., Middleton, P. M., & Lovell, N. H. (2012). Spontaneous fluctuations in the peripheral photoplethysmographic waveform: roles of arterial pressure and muscle sympathetic nerve activity. *American Journal of Physiology-Heart and Circulatory Physiology, 302*(3), H826-H836.

Chang, C.-C., & Lin, C.-J. (2011). LIBSVM: A library for support vector machines. *ACM transactions on intelligent systems and technology (TIST), 2*(3), 1-27.

Charbonnier, S., Siche, J., & Vancura, R. (2000). *On line detection of movement artifacts to improve ambulatory blood pressure monitoring.* Paper presented at the Proceedings of the 17th IEEE Instrumentation and Measurement Technology Conference.

Chen, S., Bolic, M., Groza, V. Z., Dajani, H. R., Batkin, I., & Rajan, S. (2010). Extraction of breathing signal and suppression of its effects in oscillometric blood pressure measurement. *IEEE Transactions on Instrumentation and Measurement, 60*(5), 1741-1750.

Chen, W., Kobayashi, T., Ichikawa, S., Takeuchi, Y., & Togawa, T. (2000). Continuous estimation of systolic blood pressure using the pulse arrival time and intermittent calibration. *Medical and biological engineering and computing, 38*(5), 569-574.

Cherif, S., Pastor, D., Nguyen, Q.-T., & L'Her, E. (2016). *Detection of artifacts on photoplethysmography signals using random distortion testing.* Paper presented at the 38th Annual International Conference of the IEEE Engineering in Medicine and Biology Society (EMBC).

Choi, H. S., Park, H. D., & Lee, K. J. (2007). *Motion artifact reduction in blood pressure signals using adaptive digital filter with a capacitive sensor.* Paper presented at the 29th Annual International Conference of the IEEE Engineering in Medicine and Biology Society.

Chon, K. H., Dash, S., & Ju, K. (2009). Estimation of respiratory rate from photoplethysmogram

data using time–frequency spectral estimation. *IEEE Transactions on Biomedical Engineering, 56*(8), 2054-2063.

Chong, J. W., Dao, D. K., Salehizadeh, S., McManus, D. D., Darling, C. E., Chon, K. H., & Mendelson, Y. (2014). Photoplethysmograph signal reconstruction based on a novel hybrid motion artifact detection–reduction approach. Part I: motion and noise artifact detection. *Annals of biomedical engineering, 42*(11), 2238-2250.

Chowdhury, S. S., Hyder, R., Hafiz, M. S. B., & Haque, M. A. (2018). Real-Time Robust Heart Rate Estimation From Wrist-Type PPG Signals Using Multiple Reference Adaptive Noise Cancellation. *IEEE Journal of Biomedical and Health Informatics, 22*(2), 450-459.

Clifford, G. D., Silva, I., Moody, B., Li, Q., Kella, D., Chahin, A., . . . Mark, R. G. (2016). False alarm reduction in critical care. *Physiol Meas, 37*(8), E5.

Colak, S., & Isik, C. (2004). *Blood pressure estimation using neural networks.* Paper presented at the IEEE International Conference onComputational Intelligence for Measurement Systems and Applications.

Colak, S., & Isik, C. (2004). *Fuzzy pulse qualifier.* Paper presented at the IEEE Annual Meeting of the Fuzzy Information.

Costarino, A. T., Davis, D. A., & Keon, T. P. (1987). Falsely normal saturation reading with the pulse oximeter. *Anesthesiology (Philadelphia), 67*(5), 830-831.

Couceiro, R., Carvalho, P., Paiva, R. P., Henriques, J., & Muehlsteff, J. (2012). *Detection of motion artifacts in photoplethysmographic signals based on time and period domain analysis.* Paper presented at the 2012 Annual international conference of the IEEE engineering in medicine and biology society.

Couceiro, R., Carvalho, P., Paiva, R. P., Henriques, J., & Muehlsteff, J. (2014). Detection of motion artifact patterns in photoplethysmographic signals based on time and period domain analysis. *Physiol Meas, 35*(12), 2369.

Cropp, A. J., Woods, L. A., Raney, D., & Bredle, D. L. (1994). Name that tone: the proliferation of alarms in the intensive care unit. *Chest, 105*(4), 1217-1220.

Da He, D., Winokur, E. S., Heldt, T., & Sodini, C. G. (2010). *The ear as a location for wearable vital signs monitoring.* Paper presented at the 2010 Annual International Conference of the IEEE Engineering in Medicine and Biology.

Dao, D., Salehizadeh, S. M., Noh, Y., Chong, J. W., Cho, C. H., McManus, D., . . . Chon, K. H. (2016). A robust motion artifact detection algorithm for accurate detection of heart rates from photoplethysmographic signals using time–frequency spectral features. *IEEE Journal of Biomedical and Health Informatics, 21*(5), 1242-1253.

Demaerschalk, B. M., Raman, R., Ernstrom, K., & Meyer, B. C. (2012). Efficacy of telemedicine for stroke: pooled analysis of the Stroke Team Remote Evaluation Using a Digital Observation Camera (STRokE DOC) and STRokE DOC Arizona telestroke trials. *Telemedicine and e-Health, 18*(3), 230-237.

Donchin, Y., & Seagull, F. J. (2002). The hostile environment of the intensive care unit. *Current opinion in critical care, 8*(4), 316-320.

Dorsett, T. J. (1991). *Application of a prediction and smoothing algorithm to noninvasive blood pressure measurement.* Paper presented at the Ann. Int. Conf. IEEE Eng. Med. Biol. Soc.

Drzewiecki, G., & Bronzino, J. (2000). Noninvasive arterial blood pressure and mechanics. *The Biomedical Engineering Handbook, 1*, 1-16.

Drzewiecki, G., Hood, R., & Apple, H. (1994). Theory of the oscillometric maximum and the systolic and diastolic detection ratios. *Annals of biomedical engineering, 22*(1), 88-96.

Elgendi, M. (2016). Optimal signal quality index for photoplethysmogram signals. *Bioengineering, 3*(4), 21.

Fallet, S., & Vesin, J. M. (2017). Robust heart rate estimation using wrist-type photoplethysmographic signals during physical exercise: an approach based on adaptive filtering. *Physiol Meas, 38*(2), 155-170.

Fischer, C., Dömer, B., Wibmer, T., & Penzel, T. (2016). An algorithm for real-time pulse waveform segmentation and artifact detection in photoplethysmograms. *IEEE Journal of Biomedical and Health Informatics, 21*(2), 372-381.

Fischer, C., Glos, M., Penzel, T., & Fietze, I. (2017). Extended algorithm for real-time pulse waveform segmentation and artifact detection in photoplethysmograms. *Somnologie, 21*(2), 110-120.

Fonseca-Reyes, S., de Alba-García, J. G., Parra-Carrillo, J. Z., & Paczka-Zapata, J. A. (2003). Effect of standard cuff on blood pressure readings in patients with obese arms. How frequent are arms of a 'large circumference'? *Blood pressure monitoring, 8*(3), 101-106.

Foo, J. Y. A., & Wilson, S. J. (2006). A computational system to optimise noise rejection in photoplethysmography signals during motion or poor perfusion states. *Medical and biological engineering and computing, 44*(1-2), 140-145.

Forouzanfar, M., Dajani, H. R., Groza, V. Z., Bolic, M., & Rajan, S. (2011). Feature-based neural network approach for oscillometric blood pressure estimation. *IEEE Transactions on Instrumentation and Measurement, 60*(8), 2786-2796.

Forouzanfar, M., Dajani, H. R., Groza, V. Z., Bolic, M., Rajan, S., & Batkin, I. (2014). Ratio-independent blood pressure estimation by modeling the oscillometric waveform envelope. *IEEE Transactions on Instrumentation and Measurement, 63*(10), 2501-2503.

Forouzanfar, M., Dajani, H. R., Groza, V. Z., Bolic, M., Rajan, S., & Batkin, I. (2015). Oscillometric blood pressure estimation: past, present, and future. *IEEE reviews in biomedical engineering, 8*, 44-63.

Forster, F. K., & Turney, D. (1986). Oscillometric determination of diastolic, mean and systolic blood pressure—a numerical model.

Frese, E. M., Fick, A., & Sadowsky, H. S. (2011). Blood pressure measurement guidelines for physical therapists. *Cardiopulmonary physical therapy journal, 22*(2), 5.

Gao, M., Olivier, N. B., & Mukkamala, R. (2016). Comparison of noninvasive pulse transit time estimates as markers of blood pressure using invasive pulse transit time measurements as a reference. *Physiological reports, 4*(10), e12768.

Gao, M., Zhang, G., Olivier, N. B., & Mukkamala, R. (2013). Improved pulse wave velocity estimation using an arterial tube-load model. *IEEE Transactions on Biomedical Engineering, 61*(3), 848-858.

Geddes, L., Voelz, M., Babbs, C., Bourland, J., & Tacker, W. (1981). Pulse transit time as an indicator of arterial blood pressure. *Psychophysiology, 18*(1), 71-74.

Geddes, L. A. (1970). *The direct and indirect measurement of blood pressure*: Year Book Medical Publishers.

Geddes, L. A., Voelz, M., James, S., & Reiner, D. (1981). Pulse arrival time as a method of obtaining systolic and diastolic blood pressure indirectly. *Medical and biological engineering and computing, 19*(5), 671-672.

Georgiou, K., Larentzakis, A. V., Khamis, N. N., Alsuhaibani, G. I., Alaska, Y. A., & Giallafos, E. J. (2018). Can wearable devices accurately measure heart rate variability? A systematic review. *Folia medica, 60*(1), 7-20.

Gerin, W., Ogedegbe, G., Schwartz, J. E., Chaplin, W. F., Goyal, T., Clemow, L., . . . Kentor, R. (2006). Assessment of the white-coat effect. *Journal of hypertension, 24*(1), 67-74.

Ghamsari, A. A., Dadpour, B., & Najari, F. (2016). Frequency of electrocardiographic abnormalities in tramadol poisoned patients; a brief report. *Emergency, 4*(3), 151.

Gil, E., Vergara, J. M., & Laguna, P. (2008). Detection of decreases in the amplitude fluctuation of pulse photoplethysmography signal as indication of obstructive sleep apnea syndrome in children. *Biomedical Signal Processing and Control, 3*(3), 267-277.

Goldberger, A. L., Amaral, L. A., Glass, L., Hausdorff, J. M., Ivanov, P. C., Mark, R. G., . . . Stanley, H. E. (2000). Physiobank, physiotoolkit, and PhysioNet. *Circulation, 101*(23), 215-220.

Grad, C., & Zdrenghea, D. (2014). Heart Rate Recovery in Patients with Ischemic Heart Disease - Risk Factors. *Clujul medical (1957), 87*(4), 220-225.

Greenhut, S. E., Jenkins, J. M., & DiCarlo, L. A. (1991). Computerized interpretation of the paced ECG. *Journal of electrocardiology, 24*, 146-152.

Guo, D. G., Tay, F. E., Xu, L., Yu, L., Nyan, M. N., Chong, F., . . . Xu, B. (2008). *A long-term wearable vital signs monitoring system using BSN.* Paper presented at the 2008 11th EUROMICRO Conference on Digital System Design Architectures, Methods and Tools.

Gupta, V., & Lipsitz, L. A. (2007). Orthostatic hypotension in the elderly: diagnosis and treatment. *The American journal of medicine, 120*(10), 841-847.

Hagerman, I., Rasmanis, G., Blomkvist, V., Ulrich, R., Eriksen, C. A., & Theorell, T. (2005). Influence of intensive coronary care acoustics on the quality of care and physiological state of patients. *International journal of cardiology, 98*(2), 267-270.

Hajat, C., & Stein, E. (2018). The global burden of multiple chronic conditions: A narrative review. *Preventive medicine reports, 12*, 284-293.

Hanyu, S., & Xiaohui, C. (2017). *Motion artifact detection and reduction in PPG signals based on statistics analysis.* Paper presented at the 2017 29th Chinese control and decision conference (CCDC).

Hartley, T. R., Sung, B. H., Pincomb, G. A., Whitsett, T. L., Wilson, M. F., & Lovallo, W. R. (2000). Hypertension risk status and effect of caffeine on blood pressure. *Hypertension, 36*(1), 137-141.

Hartmut Gehring, M., ME, H. M., & Schmucker, P. (2002). The effects of motion artifact and low perfusion on the performance of a new generation of pulse oximeters in volunteers undergoing hypoxemia. *Respiratory Care, 47*(1), 48-60.

Harvey, J., Salehizadeh, S. M., Mendelson, Y., & Chon, K. H. (2018). OxiMA: A Frequency-Domain Approach to Address Motion Artifacts in Photoplethysmograms for Improved Estimation of Arterial Oxygen Saturation and Pulse Rate. *IEEE Transactions on Biomedical Engineering, 66*(2), 311-318.

Hashem, M., Shams, R., Kader, M. A., & Sayed, M. A. (2010). *Design and development of a heart rate measuring device using fingertip.* Paper presented at the International Conference on Computer and Communication Engineering (ICCCE'10).

Hasnain, A., Awan, M., & Farooq, M. (2009). *A ubiquitous real-time motion artifact rejection technique for remote NIBP monitoring of hypertensive patients.* Paper presented at the World Congress on Medical Physics and Biomedical Engineering.

Havlík, J., Martinovská, Z., Dvořák, J., & Lhotská, L. (2014). *Detection of artifacts in oscillometric pulsations signals.* Paper presented at the IEEE-EMBS International Conference on Biomedical and Health Informatics (BHI).

Hayes, M. J., & Smith, P. R. (1998). Artifact reduction in photoplethysmography. *Applied Optics, 37*(31), 7437-7446.

Hayes, M. J., & Smith, P. R. (2001). A new method for pulse oximetry possessing inherent insensitivity to artifact. *IEEE Transactions on Biomedical Engineering, 48*(4), 452-461.

Heravi, M. Y., Khalilzadeh, M., & Joharinia, S. (2014). Continuous and cuffless blood pressure monitoring based on ECG and SpO2 signals ByUsing Microsoft visual C sharp. *Journal of biomedical physics & engineering, 4*(1), 27.

Hickey, M., Phillips, J. P., & Kyriacou, P. A. (2016). Investigation of peripheral photoplethysmographic morphology changes induced during a hand-elevation study. *Journal of clinical monitoring and computing, 30*(5), 727-736.

Hilty, D. M., Nesbitt, T. S., Marks, S. L., & Callahan, E. J. (2002). Effects of telepsychiatry on the doctor-patient relationship: communication, satisfaction, and relevant issues. *Primary Psychiatry, 9*(9), 29-34.

Hjorth, B. (1970). EEG analysis based on time domain properties. *Electroencephalography and clinical neurophysiology, 29*(3), 306-310.

Hjorth, B. (1973). The physical significance of time domain descriptors in EEG analysis. *Electroencephalography and clinical neurophysiology, 34*(3), 321-325.

Hong, K. S., Park, K. T., & Ahn, J. M. (2015). Aging index using photoplethysmography for a healthcare device: comparison with brachial-ankle pulse wave velocity. *Healthcare informatics research, 21*(1), 30-34.

Hug, C. W., Clifford, G. D., & Reisner, A. T. (2011). Clinician blood pressure documentation of stable intensive care patients: an intelligent archiving agent has a higher association with future hypotension. *Critical care medicine, 39*(5), 1006.

Ihara, Z. (2006). *Design and performance of lead systems for the analysis of atrial signal components in the ECG.* EPFL.

Imhoff, M., & Kuhls, S. (2006). Alarm algorithms in critical care monitoring. *Anesthesia & Analgesia, 102*(5), 1525-1537.

Institute of Medicine Committee on Evaluating Clinical Applications of, T. (1996). The National Academies Collection: Reports funded by National Institutes of Health. In M. J. Field (Ed.), *Telemedicine: A Guide to Assessing Telecommunications in Health Care*. Washington (DC): National Academies Press (US)

National Academy of Sciences.

Jarchi, D., & Casson, A. (2016). Description of a Database Containing Wrist PPG Signals

Recorded during Physical Exercise with Both Accelerometer and Gyroscope Measures of Motion. *Data, 2*.
Jazbinsek, V., Luznik, J., Mieke, S., & Trontelj, Z. (2010). Influence of different presentations of oscillometric data on automatic determination of systolic and diastolic pressures. *Annals of biomedical engineering, 38*(3), 774-787.
Jin, J. (2018). Screening for Cardiovascular Disease Risk With ECG. *Jama, 319*(22), 2346.
Jones, A., & Pratt, O. (2009). Physical principles of intra-arterial blood pressure measurement. *World Anaesth Tutor Week, 137*(8), 44-49.
Joshi, A. K., Tomar, A., & Tomar, M. (2014). A review paper on analysis of electrocardiograph (ECG) signal for the detection of arrhythmia abnormalities. *International Journal of Advanced Research in Electrical, Electronics and Instrumentation Engineering, 3*(10), 12466-12475.
Karlen, W., Kobayashi, K., Ansermino, J. M., & Dumont, G. (2012). Photoplethysmogram signal quality estimation using repeated Gaussian filters and cross-correlation. *Physiol Meas, 33*(10), 1617.
Kasaeyan Naeini, E., Azimi, I., Rahmani, A. M., Liljeberg, P., & Dutt, N. (2019). A Real-time PPG Quality Assessment Approach for Healthcare Internet-of-Things. *Procedia Computer Science, 151*, 551-558.
Kaur, D., Kumar, S., & Sharma, S. (2011). Online Graphical Display of Blood Oxygen Saturation and Pulse Rate. *International Journal of Scientific & Engineering Research, 2*(6), 20-25.
Kim, B. S., & Yoo, S. K. (2006). Motion artifact reduction in photoplethysmography using independent component analysis. *IEEE Transactions on Biomedical Engineering, 53*(3), 566-568.
Komine, H., Asai, Y., Yokoi, T., & Yoshizawa, M. (2012). Non-invasive assessment of arterial stiffness using oscillometric blood pressure measurement. *Biomedical engineering online, 11*(1), 6.
Koo, Y., Kang, J., Shin, I. H., Jung, M. Y., Suh, G. J., & Kim, H. C. (2007). *Preliminary study of motion artifact rejection for NIBP measurement in an ambulance.* Paper presented at the 2007 29th Annual International Conference of the IEEE Engineering in Medicine and Biology Society.
Krishnan, R., Natarajan, B., & Warren, S. (2008). *Analysis and detection of motion artifact in photoplethysmographic data using higher order statistics.* Paper presented at the 2008 IEEE International Conference on Acoustics, Speech and Signal Processing.
Kyriacou, P., Moye, A., Gregg, A., Choi, D., Langford, R., & Jones, D. (1999). A system for investigating oesophageal photoplethysmographic signals in anaesthetised patients. *Medical & biological engineering & computing, 37*(5), 639-643.
Kyriacou, P. A. (2013). Direct pulse oximetry within the esophagus, on the surface of abdominal viscera, and on free flaps. *Anesthesia & Analgesia, 117*(4), 824-833.
Kyriacou, P. A., Powell, S., Langford, R. M., & Jones, D. P. (2002). Esophageal pulse oximetry utilizing reflectance photoplethysmography. *IEEE Transactions on Biomedical Engineering, 49*(11), 1360-1368.
Landgraf, J., Wishner, S. H., & Kloner, R. A. (2010). Comparison of automated oscillometric versus auscultatory blood pressure measurement. *The American journal of cardiology, 106*(3), 386-388.
Lee, B., Han, J., Baek, H. J., Shin, J. H., Park, K. S., & Yi, W. J. (2010). Improved elimination of motion artifacts from a photoplethysmographic signal using a Kalman smoother with simultaneous accelerometry. *Physiol Meas, 31*(12), 1585.
Lee, C., & Zhang, Y. T. (2003). *Reduction of motion artifacts from photoplethysmographic recordings using a wavelet denoising approach.* Paper presented at the IEEE EMBS Asian-Pacific Conference on Biomedical Engineering, 2003.
Lee, H.-W., Lee, J.-W., Jung, W.-G., & Lee, G.-K. (2007). The periodic moving average filter for removing motion artifacts from PPG signals. *International Journal of Control, Automation, and Systems, 5*(6), 701-706.
Lee, S., Bolic, M., Groza, V. Z., Dajani, H. R., & Rajan, S. (2011). Confidence interval estimation for oscillometric blood pressure measurements using bootstrap approaches. *IEEE Transactions on Instrumentation and Measurement, 60*(10), 3405-3415.
Lee, S., Chang, J.-H., Nam, S. W., Lim, C., Rajan, S., Dajani, H. R., & Groza, V. Z. (2013).

Oscillometric blood pressure estimation based on maximum amplitude algorithm employing Gaussian mixture regression. *IEEE Transactions on Instrumentation and Measurement, 62*(12), 3387-3389.

Lee, S., Jeon, G., & Lee, G. (2013). On using maximum a Posteriori probability based on a Bayesian model for oscillometric blood pressure estimation. *Sensors, 13*(10), 13609-13623.

Lee, S., Lim, C., & Chang, J.-H. (2014). A new a priori SNR estimator based on multiple linear regression technique for speech enhancement. *Digital Signal Processing, 30*, 154-164.

Lee, S., Rajan, S., Dajani, H. R., Groza, V. Z., & Bolic, M. (2011). *Determination of blood pressure using Bayesian approach.* Paper presented at the 2011 IEEE International Instrumentation and Measurement Technology Conference.

Lee, Y., Shin, H., Jo, J., & Lee, Y.-K. (2011). *Development of a wristwatch-type PPG array sensor module.* Paper presented at the 2011 IEEE International Conference on Consumer Electronics-Berlin (ICCE-Berlin).

Lei, W., Lo, B. P., & Guang-Zhong, Y. (2007). Multichannel Reflective PPG Earpiece Sensor With Passive Motion Cancellation. *IEEE Trans Biomed Circuits Syst, 1*(4), 235-241.

Li, D., Zhao, H., & Dou, S. (2015). A new signal decomposition to estimate breathing rate and heart rate from photoplethysmography signal. *Biomedical Signal Processing and Control, 19*, 89-95.

Li, Q., & Clifford, G. (2012). Dynamic time warping and machine learning for signal quality assessment of pulsatile signals. *Physiological measurement, 33*(9), 1491.

Li, Q., & Clifford, G. D. (2012). Dynamic time warping and machine learning for signal quality assessment of pulsatile signals. *Physiol Meas, 33*(9), 1491.

Lin, C.-T., Liu, S.-H., Wang, J.-J., & Wen, Z.-C. (2003). Reduction of interference in oscillometric arterial blood pressure measurement using fuzzy logic. *IEEE Transactions on Biomedical Engineering, 50*(4), 432-441.

Liu, J., Hahn, J.-O., & Mukkamala, R. (2013). Error mechanisms of the oscillometric fixed-ratio blood pressure measurement method. *Annals of biomedical engineering, 41*(3), 587-597.

Liu, S.-H., & Lin, C.-T. (2001). A model-based fuzzy logic controller with Kalman filtering for tracking mean arterial pressure. *IEEE Transactions on Systems, Man, and Cybernetics-Part A: Systems and Humans, 31*(6), 676-686.

Longmore, S. K., Lui, G. Y., Naik, G., Breen, P. P., Jalaludin, B., & Gargiulo, G. D. (2019). A Comparison of Reflective Photoplethysmography for Detection of Heart Rate, Blood Oxygen Saturation, and Respiration Rate at Various Anatomical Locations. *Sensors (Basel), 19*(8), 1874.

Madhav, K. V., Ram, M. R., Krishna, E. H., Reddy, K. N., & Reddy, K. A. (2010). *Estimation of respiratory rate from principal components of photoplethysmographic signals.* Paper presented at the 2010 IEEE EMBS Conference on Biomedical Engineering and Sciences (IECBES).

Maeda, Y., Sekine, M., & Tamura, T. (2011a). The advantages of wearable green reflected photoplethysmography. *Journal of medical systems, 35*(5), 829-834.

Maeda, Y., Sekine, M., & Tamura, T. (2011b). Relationship between measurement site and motion artifacts in wearable reflected photoplethysmography. *Journal of medical systems, 35*(5), 969-976.

Mafi, M., Rajan, S., Bolic, M., Groza, V. Z., & Dajani, H. R. (2011). *Blood pressure estimation using oscillometric pulse morphology.* Paper presented at the 2011 Annual International Conference of the IEEE Engineering in Medicine and Biology Society.

Maguire, M., & Ward, T. E. (2002). The design and clinical use of a reflective brachial photoplethysmograph.

Mancia, G., Fagard, R., Narkiewicz, K., Redon, J., Zanchetti, A., Böhm, M., . . . Dominiczak, A. (2014). 2013 ESH/ESC Practice guidelines for the management of arterial hypertension: ESH-ESC The Task Force for the management of arterial hypertension of the European Society of Hypertension (ESH) and of the European Society of Cardiology (ESC). *Blood pressure, 23*(1), 3-16.

Manolis, A. J., Rosei, E. A., Coca, A., Cifkova, R., Erdine, S. E., Kjeldsen, S., . . . Redon, J. (2012). Hypertension and atrial fibrillation: diagnostic approach, prevention and treatment. Position paper of the Working Group 'Hypertension Arrhythmias and

Thrombosis' of the European Society of Hypertension. *Journal of hypertension, 30*(2), 239-252.
Marazzi, G., Iellamo, F., Volterrani, M., Lombardo, M., Pelliccia, F., Righi, D., . . . Caminiti, G. (2012). Comparison of Microlife BP A200 Plus and Omron M6 blood pressure monitors to detect atrial fibrillation in hypertensive patients. *Advances in therapy, 29*(1), 64-70.
Matthews, D. E. (2005). *Multiple Linear Regression (Vol. 2nd ed).* : London, UK: Wiley.
McFarlane, J. (2012). Blood pressure measurement in obese patients. *Critical care nurse, 32*(6), 70-73.
Mendelson, Y., & Pujary, C. (2003). *Measurement site and photodetector size considerations in optimizing power consumption of a wearable reflectance pulse oximeter.* Paper presented at the Proceedings of the 25th Annual International Conference of the IEEE Engineering in Medicine and Biology Society (IEEE Cat. No. 03CH37439).
Meng'anyi, L. W., Omondi, L. A., & Muiva, M. N. (2017). Assessment of nurses interventions in the Management of Clinical Alarms in the critical care unit, Kenyatta National Hospital, a cross sectional study. *BMC nursing, 16*(1), 41.
Millasseau, S. C., Kelly, R., Ritter, J., & Chowienczyk, P. (2002). Determination of age-related increases in large artery stiffness by digital pulse contour analysis. *Clinical science, 103*(4), 371-377.
Moraes, J. C. T. d. B., Cerulli, M., & Ng, P. (2000). *A strategy for determination of systolic, mean and diastolic blood pressures from oscillometric pulse profiles.* Paper presented at the Computers in Cardiology 2000. Vol. 27 (Cat. 00CH37163).
Moraes, J. L., Rocha, M. X., Vasconcelos, G. G., Vasconcelos Filho, J. E., De Albuquerque, V. H. C., & Alexandria, A. R. (2018). Advances in photopletysmography signal analysis for biomedical applications. *Sensors, 18*(6), 1894.
Moyer, V. A. (2012). Screening for coronary heart disease with electrocardiography: US Preventive Services Task Force recommendation statement. *Annals of internal medicine, 157*(7), 512-518.
Nam, Y., Lee, J., & Chon, K. H. (2014). Respiratory rate estimation from the built-in cameras of smartphones and tablets. *Annals of biomedical engineering, 42*(4), 885-898.
Narus, S., Egbert, T., Lee, T.-K., Lu, J., & Westenskow, D. (1995). Noninvasive blood pressure monitoring from the supraorbital artery using an artificial neural network oscillometric algorithm. *Journal of clinical monitoring, 11*(5), 289.
Naschitz, J. E., Bezobchuk, S., Mussafia-Priselac, R., Sundick, S., Dreyfuss, D., Khorshidi, I., . . . Peck, E. R. (2004). Pulse transit time by R-wave-gated infrared photoplethysmography: review of the literature and personal experience. *Journal of clinical monitoring and computing, 18*(5-6), 333-342.
Nguyen, Q. V., Le Page, R., Goujon, J.-M., Poffo, L., & Thual, M. (2011). Comparison of two methods for demodulation of pulse signals-application in case of central sleep apnea.
Nia, A. M., Mozaffari-Kermani, M., Sur-Kolay, S., Raghunathan, A., & Jha, N. K. (2015). Energy-efficient long-term continuous personal health monitoring. *IEEE Transactions on Multi-Scale Computing Systems, 1*(2), 85-98.
Noel, H. C., Vogel, D. C., Erdos, J. J., Cornwall, D., & Levin, F. (2004). Home telehealth reduces healthcare costs. *Telemedicine Journal & e-Health, 10*(2), 170-183.
Novaes, M., Aronovich, A., Ferraz, M., & Knobel, E. (1997). Stressors in ICU: patients' evaluation. *Intensive Care Medicine, 23*(12), 1282-1285.
O'Brien, E., Petrie, J., Littler, W., de Swiet, M., Padfield, P. L., Altman, D., . . . Atkins, N. (1993). The British Hypertension Society protocol for the evaluation of blood pressure measuring devices. *J hypertens, 11*(Suppl 2), S43-S62.
Obrist, P. A., Light, K. C., McCubbin, J. A., Hutcheson, J. S., & Hoffer, J. L. (1979). Pulse transit time: Relationship to blood pressure and myocardial performance. *Psychophysiology, 16*(3), 292-301.
Ochiai, R., Takeda, J., Hosaka, H., Sugo, Y., Tanaka, R., & Soma, T. (1999). The relationship between modified pulse wave transit time and cardiovascular changes in isoflurane anesthetized dogs. *Journal of clinical monitoring and computing, 15*(7-8), 493-501.
Organization, W. H. (2011). Pulse oximetry training manual. *Geneva: World Health Organization*.
Orphanidou, C., Bonnici, T., Charlton, P., Clifton, D., Vallance, D., & Tarassenko, L. (2014).

Signal-quality indices for the electrocardiogram and photoplethysmogram: Derivation and applications to wireless monitoring. *IEEE Journal of Biomedical and Health Informatics, 19*(3), 832-838.

Pagonas, N., Schmidt, S., Eysel, J., Compton, F., Hoffmann, C., Seibert, F., . . . Westhoff, T. H. (2013). Impact of atrial fibrillation on the accuracy of oscillometric blood pressure monitoring. *Hypertension, 62*(3), 579-584.

Palen, T. E., Price, D., Shetterly, S., & Wallace, K. B. (2012). Comparing virtual consults to traditional consults using an electronic health record: an observational case–control study. *BMC medical informatics and decision making, 12*(1), 65.

Patterson, J. A., McIlwraith, D. C., & Yang, G.-Z. (2009). *A flexible, low noise reflective PPG sensor platform for ear-worn heart rate monitoring.* Paper presented at the 2009 sixth international workshop on wearable and implantable body sensor networks.

Payne, R., Symeonides, C., Webb, D., & Maxwell, S. (2006). Pulse transit time measured from the ECG: an unreliable marker of beat-to-beat blood pressure. *Journal of Applied Physiology, 100*(1), 136-141.

Peel III, H. H. (1999). U.S. Patent No. 5865756.

Pereira, T., Tran, N., Gadhoumi, K., Pelter, M. M., Do, D. H., Lee, R. J., . . . Hu, X. (2020). Photoplethysmography based atrial fibrillation detection: a review. *npj Digital Medicine, 3*(1), 1-12.

Perloff, D., Grim, C., Flack, J., Frohlich, E. D., Hill, M., McDonald, M., & Morgenstern, B. Z. (1993). Human blood pressure determination by sphygmomanometry. *circulation, 88*(5), 2460-2470.

Petterson, M. T., Begnoche, V. L., & Graybeal, J. M. (2007). The effect of motion on pulse oximetry and its clinical significance. *Anesthesia & Analgesia, 105*(6), S78-S84.

Pflugradt, M., Geissdoerfer, K., Goernig, M., & Orglmeister, R. (2017). A fast multimodal ectopic beat detection method applied for blood pressure estimation based on pulse wave velocity measurements in wearable sensors. *Sensors, 17*(1), 158.

Pickering, T. G., Hall, J. E., Appel, L. J., Falkner, B. E., Graves, J., Hill, M. N., . . . Roccella, E. J. (2005). Recommendations for blood pressure measurement in humans and experimental animals: part 1: blood pressure measurement in humans: a statement for professionals from the Subcommittee of Professional and Public Education of the American Heart Association Council on High Blood Pressure Research. *Hypertension, 45*(1), 142-161.

Pinar, R., Ataalkin, S., & Watson, R. (2010). The effect of crossing legs on blood pressure in hypertensive patients. *Journal of clinical nursing, 19*(9- 10), 1284-1288.

Poh, M.-Z., Kim, K., Goessling, A., Swenson, N., & Picard, R. (2010). Cardiovascular monitoring using earphones and a mobile device. *IEEE Pervasive Computing, 11*(4), 18-26.

Poh, M.-Z., Swenson, N. C., & Picard, R. W. (2010). Motion-tolerant magnetic earring sensor and wireless earpiece for wearable photoplethysmography. *IEEE Transactions on Information Technology in Biomedicine, 14*(3), 786-794.

Poon, C. C., Liu, Q., Gao, H., Lin, W.-H., & Zhang, Y.-T. (2011). Wearable intelligent systems for e-health. *Journal of Computing Science and Engineering, 5*(3), 246-256.

Pounds, N. (2018). *A study into Vibro-acoustic stimulation methods to reduce heart-rate measured using an electrocardiogram to support research in alieving symptoms of stress.* (Master). London South Bank University.

Prathyusha, B., Rao, T. S., & Asha, D. (2012). Extraction of respiratory rate from PPG signals using PCA and EMD. *International Journal of Research in Engineering and Technology, 1*(2), 164-184.

Pruett, J., Bourland, J., & Geddes, L. (1988). Measurement of pulse-wave velocity using a beat-sampling technique. *Annals of biomedical engineering, 16*(4), 341-347.

Raamat, R., Jagomägi, K., Talts, J., & Kivastik, J. (2013). *A model-based retrospective analysis of the fixed-ratio oscillometric blood pressure measurement.* Paper presented at the 13th IEEE International Conference on BioInformatics and BioEngineering.

Raftery, E. B. (1978). The methodology of blood pressure recording. *British journal of clinical pharmacology, 6*(3), 193-201.

Reddy, K. A., George, B., & Kumar, V. J. (2008). Use of fourier series analysis for motion artifact reduction and data compression of photoplethysmographic signals. *IEEE Transactions*

on Instrumentation and Measurement, 58(5), 1706-1711.
Redmond, S. J., Xie, Y., Chang, D., Basilakis, J., & Lovell, N. H. (2012). Electrocardiogram signal quality measures for unsupervised telehealth environments. *Physiol Meas, 33*(9), 1517.
Reiss, A., Indlekofer, I., Schmidt, P., & Van Laerhoven, K. (2019). Deep PPG: Large-Scale Heart Rate Estimation with Convolutional Neural Networks. *Sensors (Basel), 19*(14).
Rhee, S., Yang, B.-H., & Asada, H. H. (2001). Artifact-resistant power-efficient design of finger-ring plethysmographic sensors. *IEEE Transactions on Biomedical Engineering, 48*(7), 795-805.
Rundo, F., Conoci, S., Ortis, A., & Battiato, S. (2018). An advanced bio-inspired photoplethysmography (PPG) and ECG pattern recognition system for medical assessment. *Sensors, 18*(2), 405.
Section 12 : ECG Artifacts. Retrieved from http://www.mauvila.com/ECG/ecg_artifact.htm
Selvaraj, N., Jaryal, A., Santhosh, J., Deepak, K. K., & Anand, S. (2008). Assessment of heart rate variability derived from finger-tip photoplethysmography as compared to electrocardiography. *Journal of medical engineering & technology, 32*(6), 479-484.
Selvaraj, N., Mendelson, Y., Shelley, K. H., Silverman, D. G., & Chon, K. H. (2011). *Statistical approach for the detection of motion/noise artifacts in Photoplethysmogram.* Paper presented at the 2011 Annual International Conference of the IEEE Engineering in Medicine and Biology Society.
Shaffer, F., & Ginsberg, J. (2017). An overview of heart rate variability metrics and norms. *Frontiers in public health, 5*, 258.
Shin, H. S., Lee, C., & Lee, M. (2009). Adaptive threshold method for the peak detection of photoplethysmographic waveform. *Computers in biology and medicine, 39*(12), 1145-1152.
Shin, K., Kim, Y., Bae, S., Park, K., & Kim, S. (2009). *A novel headset with a transmissive PPG sensor for heart rate measurement.* Paper presented at the 13th International Conference on Biomedical Engineering.
Smola, A. J., & Schölkopf, B. (2004). A tutorial on support vector regression. *Statistics and computing, 14*(3), 199-222.
Soueidan, K., Chen, S., Dajani, H. R., Bolic, M., & Groza, V. (2012). Augmented blood pressure measurement through the noninvasive estimation of physiological arterial pressure variability. *Physiol Meas, 33*(6), 881.
Stergiou, G. S., Alpert, B. S., Mieke, S., Wang, J., & O'Brien, E. (2018). Validation protocols for blood pressure measuring devices in the 21st century. *The Journal of Clinical Hypertension, 20*(7), 1096-1099.
Sukor, J. A. (2012). *Signal quality measures for pulse oximetry and blood pressure signals acquired in unsupervised home telecare environments.* (P.h.D.). Univeristy of New South Wales.
Sukor, J. A., Redmond, S., & Lovell, N. (2011). Signal quality measures for pulse oximetry through waveform morphology analysis. *Physiol Meas, 32*(3), 369.
Sukor, J. A., Redmond, S. J., Chan, G. S., & Lovell, N. H. (2012). Signal quality measures for unsupervised blood pressure measurement. *Physiol Meas, 33*(3), 465.
Sun, X., Yang, P., & Zhang, Y.-T. (2012). *Assessment of photoplethysmogram signal quality using morphology integrated with temporal information approach.* Paper presented at the 2012 Annual International Conference of the IEEE Engineering in Medicine and Biology Society.
Sun, Z. (2015). Aging, arterial stiffness, and hypertension. *Hypertension, 65*(2), 252-256.
Talts, J., Raamat, R., Jagomägi, K., & Kivastik, J. (2011). *An influence of multiple affecting factors on characteristic ratios of oscillometric blood pressure measurement.* Paper presented at the 15th Nordic-Baltic Conference on Biomedical Engineering and Medical Physics (NBC 2011).
Tamura, T., Maeda, Y., Sekine, M., & Yoshida, M. (2014). Wearable photoplethysmographic sensors—past and present. *Electronics, 3*(2), 282-302.
Tsien, C. L., & Fackler, J. C. (1997). Poor prognosis for existing monitors in the intensive care unit. *Critical care medicine, 25*(4), 614-619.
Tur, E., Tur, M., Maibach, H. I., & Guy, R. H. (1983). Basal perfusion of the cutaneous

microcirculation: measurements as a function of anatomic position. *Journal of investigative dermatology, 81*(5), 442-446.
Uçar, M. K., Bozkurt, M. R., Bilgin, C., & Polat, K. (2017). Automatic detection of respiratory arrests in OSA patients using PPG and machine learning techniques. *Neural Computing and Applications, 28*(10), 2931-2945.
Umana, E., Ahmed, W., Fraley, M. A., & Alpert, M. A. (2006). Comparison of oscillometric and intraarterial systolic and diastolic blood pressures in lean, overweight, and obese patients. *Angiology, 57*(1), 41-45.
Ursino, M., & Cristalli, C. (1996). A mathematical study of some biomechanical factors affecting the oscillometric blood pressure measurement. *IEEE Transactions on Biomedical Engineering, 43*(8), 761-778.
van Popele, N. M., Bos, W. J. W., de Beer, N. A., van der Kuip, D. A., Hofman, A., Grobbee, D. E., & Witteman, J. C. (2000). Arterial stiffness as underlying mechanism of disagreement between an oscillometric blood pressure monitor and a sphygmomanometer. *Hypertension, 36*(4), 484-488.
Vandecasteele, K., Lázaro, J., Cleeren, E., Claes, K., Van Paesschen, W., Van Huffel, S., & Hunyadi, B. (2018). *Artifact Detection of Wrist Photoplethysmograph Signals*. Paper presented at the Biosignals.
Verberk, W. J., & De Leeuw, P. W. (2012). Accuracy of oscillometric blood pressure monitors for the detection of atrial fibrillation: a systematic review. *Expert review of medical devices, 9*(6), 635-640.
Verberk, W. J., Omboni, S., Kollias, A., & Stergiou, G. S. (2016). Screening for atrial fibrillation with automated blood pressure measurement: research evidence and practice recommendations. *International journal of cardiology, 203*, 465-473.
Verma, D., & Bhasin, M. (2014). Real time optical heart rate monitor. *International Journal of Computer Science and Information Technologies, 5*(6), 7265-7269.
Vlachopoulos, C., O'Rourke, M., & Nichols, W. W. (2011). *McDonald's blood flow in arteries: theoretical, experimental and clinical principles*: CRC press.
Vogel, S., Hülsbusch, M., Hennig, T., Blazek, V., & Leonhardt, S. (2009). In-ear vital signs monitoring using a novel microoptic reflective sensor. *IEEE Transactions on Information Technology in Biomedicine, 13*(6), 882-889.
Wang, C.-Z., & Zheng, Y.-P. (2008). *Home-telecare of the elderly living alone using an new designed ear-wearable sensor*. Paper presented at the 2008 5th International Summer School and Symposium on Medical Devices and Biosensors.
Wang, L., Lo, B. P., & Yang, G.-Z. (2007). Multichannel reflective PPG earpiece sensor with passive motion cancellation. *IEEE Trans Biomed Circuits Syst, 1*(4), 235-241.
Ward, M., & Langton, J. A. (2007). Blood pressure measurement. *Continuing education in anaesthesia, critical care & pain, 7*(4), 122-126.
Whelton, P., Carey, R., Aronow, W., Casey Jr, D., Collins, K., Himmelfarb, D. C., . . . Jones, D. (2018). y 2017 ACC/AHA/AAPA/ABC/ACPM/AGS/APhA/ASH/ASPC/NMA/PCNA Guideline for the Prevention, Detection, Evaluation, and Management of High Blood Pressure in Adults: A Report of the American College of Cardiology/American Heart Association Task Force on Clinical Practice Guidelines (vol 71, pg e127, 2018). *Journal of the American College of Cardiology, 71*(19), 2275-2279.
Xing, X., & Sun, M. (2016). Optical blood pressure estimation with photoplethysmography and FFT-based neural networks. *Biomedical optics express, 7*(8), 3007-3020.
Yan, Y.-s., Poon, C. C., & Zhang, Y.-t. (2005). Reduction of motion artifact in pulse oximetry by smoothed pseudo Wigner-Ville distribution. *Journal of NeuroEngineering and Rehabilitation, 2*(1), 3.
Yang, F., Chen, F., Zhu, M., Chen, A., & Zheng, D. (2017). Significantly reduced blood pressure measurement variability for both normotensive and hypertensive subjects: effect of polynomial curve fitting of oscillometric pulses. *BioMed research international*.
Yin, H., Akmandor, A. O., Mosenia, A., & Jha, N. K. (2018). Smart healthcare. *Foundations and Trends® in Electronic Design Automation, 12*(4), 401-466.
Young, L. B., Chan, P. S., Lu, X., Nallamothu, B. K., Sasson, C., & Cram, P. M. (2011). Impact of telemedicine intensive care unit coverage on patient outcomes: a systematic review and meta-analysis. *Archives of internal medicine, 171*(6), 498-506.

Yousefi, R., Nourani, M., Ostadabbas, S., & Panahi, I. (2013). A motion-tolerant adaptive algorithm for wearable photoplethysmographic biosensors. *IEEE Journal of Biomedical and Health Informatics, 18*(2), 670-681.

Yousefi, R., Nourani, M., Ostadabbas, S., & Panahi, I. (2014). A motion-tolerant adaptive algorithm for wearable photoplethysmographic biosensors. *IEEE J Biomed Health Inform, 18*(2), 670-681.

Yu, P.-S., Chen, S.-T., & Chang, I.-F. (2006). Support vector regression for real-time flood stage forecasting. *Journal of Hydrology, 328*(3-4), 704-716.

Yuan, H., Poeggel, S., Newe, T., Lewis, E., Viphavakit, C., & Leen, G. (2017). An experimental study of the effects of external physiological parameters on the photoplethysmography signals in the context of local blood pressure (hydrostatic pressure changes). *Sensors, 17*(3), 556.

Zhang, Y., Song, S., Vullings, R., Biswas, D., Simões-Capela, N., Van Helleputte, N., . . . Groenendaal, W. (2019). Motion artifact reduction for wrist-worn photoplethysmograph sensors based on different wavelengths. *Sensors, 19*(3), 673.

Zheng, D., Amoore, J. N., Mieke, S., & Murray, A. (2011). Estimation of mean arterial pressure from the oscillometric cuff pressure: comparison of different techniques. *Medical & biological engineering & computing, 49*(1), 33-39.

Zheng, D., & Murray, A. (2008). *Estimation of mean blood pressure from oscillometric and manual methods.* Paper presented at the 2008 Computers in Cardiology.

Zhu, B., Ding, Y., & Hao, K. (2013). A novel automatic detection system for ECG arrhythmias using maximum margin clustering with immune evolutionary algorithm. *Computational and mathematical methods in medicine*.

Zhu, Z., Ong, Y.-S., & Dash, M. (2007). Wrapper–filter feature selection algorithm using a memetic framework. *IEEE Transactions on Systems, Man, and Cybernetics, Part B (Cybernetics), 37*(1), 70-76.

LIST OF PUBLICATIONS AND PAPERS PRESENTED

Journal articles:

1. **Pooi Khoon Lim**, Siew-Cheok Ng, Wissam A. Jassim, Stephen J. Redmond, Mohammad Zilany, Alberto Avolio, Einly Lim, Maw Pin Tan and Nigel H. Lov. *Improved Measurement of Blood Pressure by Extraction of Characteristic Features from the Cuff Oscillometric Waveform.* Sensors (Basel), 2015. 15(6): p. 14142-61.

2. **Pooi Khoon Lim**, Siew-Cheok Ng, Nigel H. Lovell, Einly Lim, Yong Poh Yu, Maw Pin Tan, and Stephen J. Redmond. *Adaptive template matching of photoplethysmogram pulses to detect motion artifact.* Physiological measurement, 2018. **39**(10):105005.